Forecasting Water Waves and Currents: A Space-time Approach

Vijaya Raghav Ambati

Colophon

The research presented in this dissertation was carried out at the Numerical Analysis and Computational Mechanics (NACM) group, Department of Applied Mathematics, Faculty of Electrical Engineering, Mathematics and Computer Science of the University of Twente, The Netherlands.

The financial support from University of Twente for this research work is gratefully acknowledged.

The thesis was typeset in LaTeX by the author and printed by Wöhrmann Printing Service, Zutphen.

ISBN 978-90-365-2632-6

FORECASTING WATER WAVES AND CURRENTS: A SPACE-TIME APPROACH

DISSERTATION

to obtain
the degree of doctor at the University of Twente,
on the authority of the rector magnificus,
prof. dr. W. H. M. Zijm,
on account of the decision of the graduation committee,
to be publicly defended
on Friday 8th of February 2008 at 15.00 hrs

Vijaya Raghav Ambati

born on 31st August 1978
in Visakhapatnam, India.

This dissertation has been approved by the promoter,
prof. dr. ir. J. J. W. van der Vegt
and the assistant promoter,
dr. ir. O. Bokhove.

Contents

Chapter 1

Introduction

1.1 Motivation

Water waves and currents which are found in the mightiest oceans as well as in the smallest streams, greatly influence our environment and man-made structures. From early civilizations to the modern age, surface water waves and currents in oceans and seas have been of great practical importance to our lives due to their impact on coastal defenses and structures, offshore structures and ship dynamics. The study of surface water waves and currents is one of the oldest topics in fluid dynamics or hydrodynamics.

The near shore (or coastal) and offshore regions of seas and oceans are particularly important because they have been the traditional locations for trade and natural resources. Typical examples of man-made structures are ports, harbors, ships, wind turbines and oil platforms. Both regions are often affected by storm surges induced by tropical cyclones and sometimes by extreme flood waves due to tsunami's. These natural disasters cause extreme wave conditions which can severely damage the coastal defenses and structures, and even flood the hinterland. In July 2005, a semi-submersible oil platform named "Thunder Horse" was found listing as shown in Fig. 1.1 after hurricane Dennis has passed through that region. Recent hurricanes, such as Katrina and Rita, and the tsunami caused by an earthquake in Indian Ocean further highlight the severe damage and flooding that may occur due to such natural disasters.

Figure 1.1: A semi-submersible oil platform, Thunder Horse, was found listing after hurricane Dennis had passed through the region in 2005. Photographed by U.S. Coast Guard.
Courtesy: `http://commons.wikimedia.org/wiki.`

For the purpose of coastal and offshore structure design and for safe modes of operation in their vicinity, it is desirable to have information not only on extreme waves but also in normal wave conditions. Furthermore, for the safety of coastal inhabitants, it is essential to forecast the flood inundation caused by storm surges or tsunami's. Improving such forecasts will help to define rescue and recovery operations, and will also help to minimize the damage inflicted on coastal installations. Thus, there is a great need for accurate prediction of water waves in seas and flood inundation in coastal regions.

Wave conditions in the interested areas of seas and oceans are estimated in two ways: developing a wave climate [1] of the area and then modeling the different waves. A typical approach in establishing the wave climate at any particular location of the sea is to use long-term wave measurements from wave gauges at selected locations and then developing hindcast models to

[1] Wave climate is defined as the general condition of the sea state at a particular location, its principal elements are wave height, wave period and wave direction.

forecast a synthetic wave climate. In general, however, limited wave data are available to determine the wave climate and an extensive gauging program would thus be required. Furthermore, if the bathymetry is complex and strong currents are present then the gauge data tend to be site specific and can not be readily interpolated or extrapolated. Considering such limitations and drawbacks, modeling waves becomes an effective approach for estimating the wave conditions in seas and the flood inundation in coastal regions.

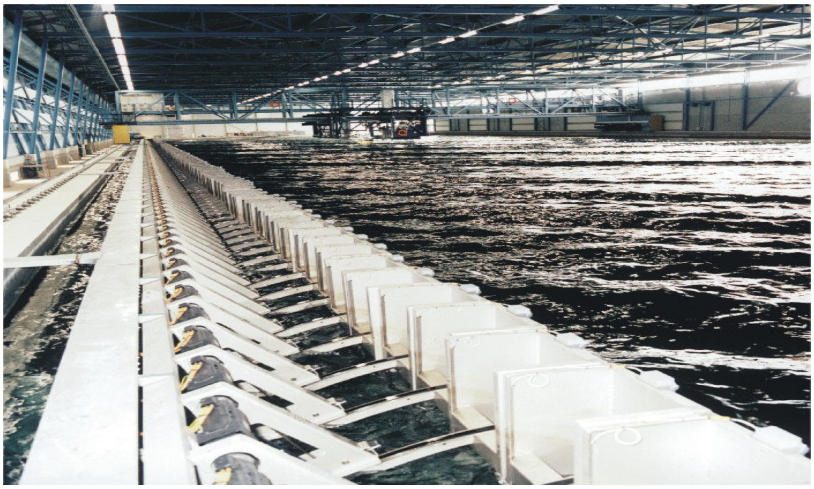

Figure 1.2: Wave basin at MARIN, Wageningen, The Netherlands. Individual controllable segments of the wave maker are clearly visible in the foreground.
Source:`http://www.marin.nl`

Modeling the effects of waves is done by a combination of physical and mathematical modeling. Physical modeling usually involves conducting experiments on a smaller scale. Experiments in a wave basin, shown in Fig. 1.2, at the Maritime Research Institute Netherlands (MARIN) are typical examples of physical modeling. Such experiments are now becoming more and more complicated and often mathematical modeling is required to design and control the experimental setup. Mathematical modeling of waves is carried out by developing a numerical method for waves and simulating

the waves for several time periods on computers. In coastal and offshore engineering, it was not feasible to conduct such numerical simulations until recently because of the large computational costs involved, the lack of high level accuracy, or both. *This has motivated us to aim at developing numerical methods for simulating waves in seas and oceans which help to estimate the wave conditions efficiently and accurately.*

1.2 Water waves and currents

Figure 1.3: Typical waves at a beach: We can clearly see the formation of white bubbly regions due to the wave breaking phenomena.

Water waves actually carry energy. It is carried along the ocean surface through the motion of water particles and mostly dissipated at the shore, which can be seen in the form of breaking waves (see Fig. 1.3). As waves approach from offshore to near shore, the water depth h gradually decreases (Fig. 1.4). In this process, the wave length λ gradually decreases towards the shore. Based on the water depth and wave length, water waves can be characterized as shallow and deep water waves when $h/\lambda < 1/20$ and

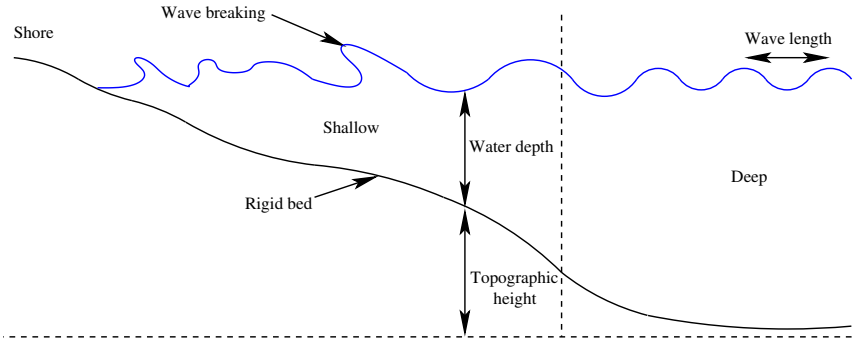

Figure 1.4: Sketch of a typical cross section of the sea.

$h/\lambda > 1/2$, respectively. Water currents are a unidirectional flow of water and some examples are long shore currents, flood currents, rip currents and oceanic currents.

In fluid dynamics, the governing equations of motion are the Navier-Stokes and Euler equations for a viscous and inviscid fluid, respectively. In wave hydrodynamics, we often assume that the water is incompressible and inviscid fluid, and thus we can obtain the Euler equations of motion for incompressible fluid. Moreover, for deep water waves, we can in addition assume the flow to be irrotational and introduce a velocity potential to simplify the Euler equations to the free surface gravity water wave equations. This set of equations consists of a potential flow equation with dynamic and kinematic boundary conditions at the free surface. On the contrary, for shallow water waves, we can neglect the vertical dependence of the fluid flow and average over the depth of the water column to obtain the depth-averaged shallow water equations. However, the shallow water equations include horizontal circulation.

The depth-averaged shallow water equations describe the near shore hydrodynamics while the free surface gravity water wave equations describe the offshore hydrodynamics. The main difficulty in solving this set of equations, analytically or numerically, is that the free boundary position is not known a priori and must be determined as part of the solution to the governing equations. To be precise, in the shallow water equations, it is the shore line boundary that the solution depends on. In the free surface grav-

ity water wave equations, it is the free surface boundary that continuously evolves in time and depends on the solution of the velocity of the water particles at the free surface. Because of the moving boundaries, it is a challenging task to develop an efficient and accurate numerical scheme for these sets of governing equations.

1.3 Research objectives

The main objective of the present research is to develop a stable, efficient and accurate numerical scheme for simulating shallow and deep water waves, which is also capable of dealing with deforming grids. Next , we review some existing methods, discuss the steps in the numerical modeling and set the important milestones to be achieved in two areas: modeling shallow and deep water waves.

1.3.1 Modeling shallow water waves

The shallow water equations from a hyperbolic system of conservation laws for mass and momentum takes into account the effects of topography and the Earth's rotation (see Pedlosky [47]). Because of their nonlinear hyperbolic nature, they can admit discontinuous solutions such as bores or jumps. These can be treated as the mathematical abstraction of three dimensional wave breaking phenomena. They can also exhibit flooding and drying as a result of the movement of the shore line boundary. Furthermore, they satisfy additional conservation laws for energy, potential vorticity and enstrophy in smooth regions of the wave field. However, in the presence of discontinuities, they dissipate energy and may generate potential vorticity. Peregrine [48] has theoretically investigated such vorticity generation due to non-uniformity of bores.

A classical numerical approach to model the shallow water equations is the finite volume method, originally developed for problems in gas dynamics (see LeVeque [36, 37] and Bouchut [13]). The finite volume method is obtained by integrating the system of conservation laws over each cell of the tessellated flow domain and solving for the cell averaged values, or "means", of the flow field across each control volume of the cell. From many years, researchers and engineers have applied the finite volume method to shallow water flows and some of the successful applications can be found in Audusse

et al. [6], Audusse and Bristeau [7] and Bouchut et al. [14]. In particular, Audusse and Bristeau [7] have applied this method to deal with flooding and drying in river flows through a hydrostatic reconstruction of the slope of the water depth to predict the shore line boundary position. Thus, the basic finite volume scheme is a computationally efficient numerical technique to model the shallow water flows but it is first order accurate. They can be extended to second order accuracy but then the computational efficiency is lost due to gradient reconstruction. Further, they can not accurately predict the shore line movement due to the cell averaged values used in the data representation.

Another class of well-known numerical methods in fluid and gas dynamics are discontinuous Galerkin finite element methods. A discontinuous Galerkin (DG) finite element method is typically obtained through a weak formulation of the system of conservation laws and by discretizing it using a polynomial approximation of the flow field. This numerical method can be classified into two main classes: space and space-time discontinuous Galerkin finite element methods. Their classification is based on the approximation of the fluid flow field using polynomials in space and space-time, respectively. A survey on discontinuous Galerkin methods can be found in Cockburn [19], and Cockburn et al. [20].

In the space discontinuous Galerkin finite element method, the weak formulation of the governing equations for fluid flow is discretized in space and an explicit numerical scheme, like Runge-Kutta time integration schemes, is considered with a CFL (Courant-Friedrichs-Lewy) condition (see Cockburn and Shu [21, 22]). The resulting space DG finite element scheme has several advantages such as,

(i) the scheme is suitable for parallel implementation because the data communication is local, in the sense that the solution in each element is dependent only on its neighboring elements via the flux through element boundaries; and

(ii) the scheme is suitable for hp adaptivity, *i.e.*, the fluid flow field approximation can arbitrarily vary per element (known as"p" adaptivity) or/and the mesh can be locally refined (called "h" adaptivity).

The space discontinuous Galerkin finite element method has already been developed for shallow water equations by Tassi et al. [57] and Bokhove

[11]. Moreover, Bokhove [11] has successfully extended this numerical scheme to the complicated phenomenon of flooding and drying. The key feature of this approach is that the flow field is approximated with linear polynomials in which the zeroth order term (mean) is used to conserve mass and momentum, while the first order term (slope) is used to track the shore line boundary in an arbitrary Eulerian Lagrangian (ALE) way. The application of the scheme was restricted to numerical examples in one dimension but an algorithm is also proposed for two dimensions in Bokhove [12]. The space DG finite element method is slightly disadvantageous to deal with deforming grids, since the time step will depend on the quality of the deforming grid due to a CFL condition and the flow field approximation needs to be constantly adapted to the deforming grids.

The space-time discontinuous Galerkin finite element method is originally developed for the incompressible Euler equations by van der Vegt and van der Ven [64]. In this method, the space-time domain is tessellated into space-time elements. The fluid flow field is approximated on the space-time elements which is used to discretize the weak formulation in space-time. The finite element discretization of the weak formulation results in a set of nonlinear algebraic equations which are solved by integrating in a pseudo time dimension until a steady state is reached. This method has all the advantages of the space DG method and several added advantages, especially for deforming grids, such as

(i) the flow field approximation need not be adapted with respect to the deforming grids because it is automatically updated in the pseudo-time dimension;

(ii) the moving boundaries can be tracked in both space and time iteratively.

(iii) the method is conservative on moving and deforming grids (see van der Vegt and van der Ven [64]).

Because of these advantages, *we aim to develop a space-time discontinuous Galerkin finite element method for the shallow water equations over varying bottom topography, including Coriolis effects, and to capture the flooding and drying phenomena.*

To achieve this goal, we propose the following intermediate milestones:

1. Develop a novel space-time discontinuous Galerkin scheme for the shallow water equations for both fixed and deforming grids. The goal is to capture the shallow water waves and currents accurately without considering the flooding and drying phenomena.

2. Extensively verify and validate the space-time discontinuous Galerkin finite element scheme for a number of demanding test cases, such as the inclusion of deforming grids due to the presence of a wave maker.

3. Extend the space-time discontinuous Galerkin finite element scheme to flooding and drying in shallow water waves and currents.

1.3.2 Modeling deep water waves

The free surface gravity water wave equations consist of a velocity potential flow equation supplemented with a dynamic and a kinematic boundary condition at the free surface. The potential flow equation is linear and elliptic in nature, where as, the dynamic and kinematic boundary conditions are nonlinear and hyperbolic in nature. This set of equations can also be derived using Luke's variational principle [39]. The beauty of a variational principle is that the complete physics of the problem can be described with a single functional and it follows the conservation of energy (see Miles [45] and Milder [46]). Another aspect of this variational principle is that the variational formulation can be considered as the basis for a finite element discretization and have the benefits of preserving energy at the discrete level.

Finite element methods based on a variational principle for free surface waves are developed in the works of Bai and Kim [8], Kim and Bai [28] and Kim et al. [29]. Classical numerical methods such as finite element methods for three dimensional nonlinear free surface waves are relatively new and can be found in the works of Cai et al. [18], Ma et al. [41, 42], Ma and Yan [43] and Westhuis [68], Wu and Taylor [70], and Wu and Hu [71].

In the discontinuous Galerkin finite element framework, the DG methods for elliptic problems proposed by Arnold et al. [5] and Brezzi [15] have enabled researchers to model free surface water waves using a space discontinuous Galerkin method. The space DG finite element method for three dimensional free surface wave problems can be found in van der Vegt and Tomar [63] and Tomar and van der Vegt [59]. Van der Vegt and Xu

[65] have subsequently proposed a space-time DG method for three dimensional nonlinear free surface waves, but its numerical scheme is tested only for two dimensional nonlinear free surface waves. The novelty of this numerical method is the coupling of the free surface boundary conditions to the space-time DG weak formulation through a flux at the free surface.

The advantages of the space-time discontinuous Galerkin method, mentioned in the previous section, have motivated us to use this method also for free surface gravity water waves. However, the development of the space-time DG method for nonlinear free surface waves has two main difficulties:

(i) It is non-trivial to develop an efficient solution technique for the nonlinear algebraic equations as the governing equations are elliptic on the flow domain and hyperbolic on the free surface.

(ii) It is a complicated matter to handle the grid deformation in the four dimensional computational space-time domain due to the nonlinearity of the free surface evolution.

Therefore, we first consider the development of a space-time DG finite element method for linear free surface waves.

In the present work, *we aim to develop an efficient and accurate numerical scheme for three dimensional linear free surface waves using a space-time DG finite element method*. We also aim to extend this numerical method based on Luke's variation principle. To achieve these goals we set the following intermediate milestones:

1. Develop a space-time discontinuous Galerkin scheme for three dimensional linear free surface waves.

2. Investigate and implement efficient and accurate numerical solvers for the linear algebraic system of equations resulting from the space-time DG discretization.

3. Extend the space-time DG method for linear free surface waves based on Luke's variational principle.

1.4 Outline

The outline of this thesis is as follows: In Chapter 2, we present a novel space-time discontinuous Galerkin method for shallow water waves. To

deal with discontinuities, we apply a dissipation operator locally around discontinuities with the help of a discontinuity detector. We conduct a discrete Fourier analysis of the numerical scheme to investigate the stability, dispersion and dissipation of the numerical scheme. We also show that our numerical scheme satisfies the rest state at the discrete level.

In Chapter 3, we verify and validate our numerical results for a number of examples arising in geophysical flows and hydrodynamics. At first, we compare the numerical results with some available exact solutions of idealized problems and verify the order of accuracy. We also test the dissipation operator combined with the discontinuity detector for the exact solutions with discontinuities. Next, we verify the dispersion and dissipation error of the numerical scheme using a discrete Fourier analysis. With the nonlinear numerical scheme, we also simulate low amplitude linear harmonic waves such as Poincare and Kelvin waves in a rectangular and circular basin, and qualitatively compare them with the exact solutions. In order to validate the bore-vortex anomaly, *i.e.,* vorticity is generated along a non-uniform bore, we simulate two idealized test cases in which a uniform bore passes over a non-uniform topography. We show that the potential vorticity is generated confirming the bore-vortex anomaly. Finally, we show an example where high amplitude waves are generated by a linear wave maker to demonstrate the capability of our numerical scheme in dealing with deforming grids.

In Chapter 4, we present a space-time discontinuous Galerkin method for linear free surface gravity water waves. First, we present the discretization of the linear free surface gravity water wave equations which leads to a linear system of algebraic equations with a compact stencil. Second, we develop a space-time DG method based on a discrete version of Luke's variational formulation for linear free surface waves. We then discuss efficient implementation techniques to build and solve the linear system of equations resulting from the discontinuous Galerkin discretizations. Finally, we verify our numerical scheme both against linear free surface harmonic waves in a periodic domain and linear free surface waves generated by a wave maker.

In Chapter 5, we present conclusions and recommendations for future research.

Chapter 2

Space-time Method for Shallow Water Waves

2.1 Introduction

For waves and currents in oceans, coastal zones and rivers with small depth and small vertical velocity scales relative to typical horizontal scales, the hydrodynamics can be studied using (rotating) shallow water equations [47]. These equations are a two dimensional hyperbolic system modeling the depth and the depth-averaged horizontal velocities for an incompressible fluid. Due to this hyperbolic nature, discontinuities can develop in the form of bores or hydraulic jumps. They exist as weak solutions [60] and are considered, in near-shore hydrodynamics, as mathematical analogs of the three dimensional wave breaking observed at beaches. The shallow water wave model is one of the simplest models to capture natural wave phenomena such as run-up and backwash of the shoreline at beaches, coastal waves and tides, and floods induced by hurricanes and tsunamis. These phenomena usually take place in a complex shaped domain with a combination of fixed and freely moving boundaries, where the moving boundaries are due to the movement of the shoreline. To cope accurately with these complexities, we present a space-time discontinuous Galerkin method for simulating shallow water waves on a dynamic spatial grid. The free boundary treatment is left to the future study but as a preliminary step we consider moving

boundaries due to a wave maker (see also [11]).

The space-time discontinuous Galerkin method (Van der Vegt and Van der Ven [64]) can accurately model inviscid compressible fluid flows in a time dependent flow domain. In this method, we tessellate the space-time domain with space-time finite elements and on such an element we define the local basis functions to approximate the flow field and test functions. As a result, the space-time weak formulation results in element volume and face integrals per space-time element. Communication between elements arises via a numerical flux. There are several choices of numerical fluxes; here we have chosen the HLLC flux because it is accurate and efficient compared with other approximate Riemann solvers (see [9], [64] and [57]). This HLLC flux results in an upwind flux in the time direction ensuring the causality of time.

The finite element discretization of the weak formulation results in a set of coupled non-linear algebraic equations per space-time element. These equations are then solved locally by adding a pseudo-time derivative and integrating in pseudo-time until a steady state is reached. We use the five-stage second-order accurate Runge-Kutta time integration scheme defined in [64]. The convergence acceleration of the pseudo-time integration scheme towards steady state can be quite slow without special attention, yet at a reasonable computation time compared to explicit space DG schemes. However, we have left the implementation of a multi-grid algorithm ([64], [44]) to accelerate the convergence of the pseudo-time integration as future work.

Numerically, spurious oscillations are expected to appear only around hydraulic jumps or bores. To limit these spurious oscillations, a dissipation operator of Jaffre et al. [26] is added to the discretization, as in Van der Vegt and Van der Ven [64] which operates everywhere but very mildly in smooth regions and strongly around discontinuities. In contrast, we apply the dissipation operator where the discontinuity detector of Krivodonova et al. [33] informs us to apply it. This more strongly preserves the higher order accuracy in smooth regions and suppresses the spurious oscillations around discontinuities.

The crucial difference between space and space-time DG methods is that in the latter case time is also treated with a finite element instead of a finite difference method. Further, space and time are treated in uni-

son with space-time basis functions, here polynomials in space and time. Preservation of non-negative or positive water depth has received a lot of attention in finite-volume modelling (e.g. [7]). It has the disadvantage that even when land must fall dry, it will always stay covered with "numerical" water. This may lead to a robust scheme but effectively leads to mass loss. Bokhove [11] therefore only ensures positive mean depths in an element, but does allow the slope of the depth to indicate where dry regions may appear in a space discontinuous Galerkin method. Problematic (e.g., in [11]) is the finite difference discretization in time, which only allows a wet region with positive depth to become a region with negative depth after one (intermediate) time step. The space-time method has the advantage of a finite element method in which the water line is known in space and time[1].

Novel is that the space-time discontinuous Galerkin method is presented for rotating shallow water waves over varying bottom topography in fixed and time dependent flow domains. To preserve the hydrostatic balance of the rest state over arbitrary topography, and uniform flow of water over a flat bottom, at the discrete level, we approximate the topography smoothly with a linear polynomial basis based on a nodal approximation per element. Discrete Fourier analysis of the present numerical method for linear rotating shallow water equations in one dimension is carried out to show that the method is unconditionally stable and has minimal dispersion error and dissipation.

In this chapter, we present the shallow water equations, their conservation laws and the generation of potential vorticity (PV) by non-uniform bores are discussed in §2.2. The space-time discontinuous Galerkin finite element method in a time dependent computational domain is presented in §2.3. A discrete Fourier analysis and the persistence of the steady rest state over smooth topography are shown in §2.4.

[1]By combining local mesh adaptation and a non-negative approach in pseudo-time, we aim to deal much more accurately with flooding and drying. Initial tests are encouraging [2].

2.2 Rotating shallow water flows

2.2.1 Mathematical model

The rotating shallow water equations in the conservative form are (see [47]):

$$\nabla \cdot \mathcal{F}_i(\mathbf{U}) = S_i \text{ in } \Omega \subset \mathbb{R}^2, \tag{2.1}$$

where $\nabla = (\partial_t, \partial_x, \partial_y)^T$ is the differential operator, $\mathbf{U} = (h, hu, hv)^T$ the state vector, $h(\mathbf{x})$ the water depth, $\mathbf{u}(\mathbf{x}) = (u(\mathbf{x}), v(\mathbf{x}))^T$ the depth-averaged velocity field,

$$\begin{pmatrix} \mathcal{F}_0(\mathbf{U}) \\ \mathcal{F}_1(\mathbf{U}) \\ \mathcal{F}_2(\mathbf{U}) \end{pmatrix} = \begin{pmatrix} h & hu & hv \\ hu & hu^2 + gh^2/2 & huv \\ hv & huv & hv^2 + gh^2/2 \end{pmatrix} \text{ the flux tensor,}$$

$$\big(S_0, S_1, S_2\big)^T = \big(0, \mathsf{f}hv - gh\partial_x h_b - C_D u|\mathbf{u}|, -\mathsf{f}hu - gh\partial_y h_b - C_D v|\mathbf{u}|\big)^T$$

the source vector, g the gravitational acceleration, f the Coriolis parameter, $h_b(\bar{\mathbf{x}})$ the bottom topography, C_D the Chezy's friction coefficient, $|\mathbf{u}| = \sqrt{u^2 + v^2}$ and $\mathbf{x} = (t, \bar{\mathbf{x}}) = (t, x, y)$ the space-time coordinates. Finally, we complete the system (2.1) with inflow, outflow or solid wall boundary conditions at the boundary $\partial\Omega \subset \mathbb{R}$ and initial conditions $\mathbf{U}(0, \bar{\mathbf{x}})$.

For numerical calculations, we non-dimensionalize the equations with typical length L, time T, depth H, and velocity V scales as

$$t' = t/T,\ \bar{\mathbf{x}}' = \bar{\mathbf{x}}/L,\ h' = h/H,\ h'_b = h_b/H,\ \mathsf{f}' = \mathsf{f}\,T \text{ and } \mathbf{u}' = \mathbf{u}/V, \tag{2.2}$$

where $V = \sqrt{gH}$ and $T = L/\sqrt{gH}$. Substituting (2.2) in (2.1) and dropping the primes, the non-dimensionalized shallow water equations effectively become (2.1) with $g = 1$, $\mathsf{f} \to \mathsf{f}T$ and $C_D \to C_D L/H$.

2.2.2 Conservation laws

The shallow water equations (2.1) govern the conservation of mass and momentum of the system. In the absence of discontinuities, the shallow water equations conserve energy, absolute vorticity and enstrophy:

$$\partial_t \begin{pmatrix} \tilde{E} \\ h\Pi \\ hQ \end{pmatrix} + \bar{\nabla} \cdot \begin{pmatrix} (\tilde{E} + gh^2/2)\mathbf{u} \\ h\mathbf{u}\Pi \\ h\mathbf{u}Q \end{pmatrix} = 0, \text{ in } \Omega \subset \mathbb{R}^2, \tag{2.3}$$

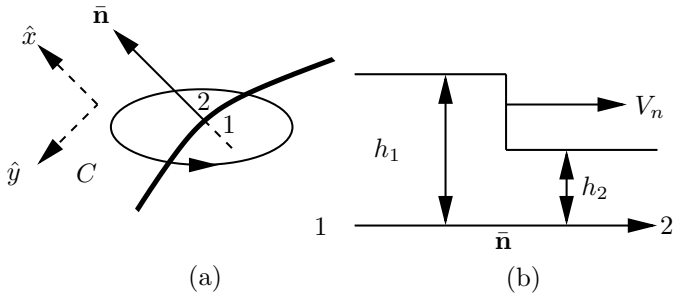

Figure 2.1: A sketch of a bore along with stream lines (left), a contour C, and traces of the upstream and downstream flow field at the bore (right).

where the energy

$$\tilde{E}(\mathbf{x}) := h|\mathbf{u}|^2/2 + gh^2/2 + ghh_b, \tag{2.4}$$

potential vorticity $\Pi(\mathbf{x}) := (\Omega_v + \mathsf{f})/h$, absolute vorticity $\Omega_v(\mathbf{x}) = \partial_x v - \partial_y u$, potential enstrophy $Q(\mathbf{x}) := \Pi^2/2$, and $\bar{\nabla} := (\partial_x, \partial_y)^T$. Furthermore, combining 2.1 and 2.3 gives that potential vorticity is materially conserved, *i.e.*,

$$\partial_t \Pi + \mathbf{u} \cdot \bar{\nabla}\Pi = 0 \text{ in } \Omega. \tag{2.5}$$

2.2.3 Bore-vortex anomaly

We concisely write (2.1) as $\partial_t \mathbf{U} + \bar{\nabla} \cdot \mathbf{F}(\mathbf{U}) = S$ with $\mathbf{U}$ the temporal and $\mathbf{F}(\mathbf{U})$ the spatial part of the flux vector $\mathcal{F}$. The shallow water equations (2.1) admit discontinuities in the form of tidal bores in coastal seas or hydraulic jumps in river channels, or may develop discontinuities in finite time from smooth initial data as bores formed due to wave breaking phenomena. These discontinuities are weak solutions of the conservation law $\partial_t \mathbf{U} + \bar{\nabla} \cdot \mathbf{F}(\mathbf{U}) = 0$. For smooth topography, they satisfy the Rankine-Hugoniot relations [36] given by

$$[\![\bar{\mathbf{n}} \cdot \mathbf{F}(\mathbf{U}) - V_n \mathbf{U}]\!] = [\![S]\!] = 0, \tag{2.6}$$

where $\bar{\mathbf{n}}$ is the unit space normal vector at point $\bar{\mathbf{x}}_c$ on the discontinuity curve pointing from 1 to 2, as in Fig. 2.1, $V_n = \mathbf{V} \cdot \bar{\mathbf{n}}$ the normal velocity

of the discontinuity, $\mathbf{V} = (V_x, V_y)^T$ the velocity of the discontinuity and $[\![\cdot]\!]$ the jump defined as $[\![q]\!] := q_1 - q_2$ with $q_1 = \lim_{\epsilon \downarrow 0} q(t, \bar{\mathbf{x}}_c - \epsilon \bar{\mathbf{n}})$ and $q_2 = \lim_{\epsilon \downarrow 0} q(t, \bar{\mathbf{x}}_c + \epsilon \bar{\mathbf{n}})$ the traces of q taken from either side of the discontinuity. Applying (2.6) for the mass and momentum conservation laws (2.1), we obtain the following jump relations across the bore ([55, 66]):

$$[\![h(\mathbf{u} \cdot \bar{\mathbf{n}} - V_n)]\!] = 0 \quad \text{and} \quad [\![h(\mathbf{u} \cdot \bar{\mathbf{n}})(\mathbf{u} \cdot \bar{\mathbf{n}} - V_n) + \frac{1}{2} g h^2]\!] = 0. \tag{2.7}$$

Introducing the normal velocity of water particles relative to the moving bore as $\hat{u} = \mathbf{u} \cdot \bar{\mathbf{n}} - V_n$ and solving the relations (2.7), we obtain

$$Q^2 := (h_1 \hat{u}_1)^2 = (h_2 \hat{u}_2)^2 = g h_1 h_2 (h_1 + h_2)/2 \tag{2.8}$$

with h_1 and h_2 the depths adjacent to the bore, and discharge Q across.

In the presence of discontinuities, the jump relations of the energy, vorticity and enstrophy conservation laws are not satisfied and hence they are not conserved. Instead, for the energy conservation law in (2.3), if we evaluate the left-hand side of the Rankine-Hugoniot relation (2.6) then we obtain the rate of energy dissipation across the bore as (see also Lamb [35] and Stoker [56])

$$Q E_D = [\![(\tilde{E} + g h^2/2)(\mathbf{u} \cdot \bar{\mathbf{n}}) - V_n \tilde{E}]\!] = g Q (h_2 - h_1)^3/(4 h_1 h_2) \tag{2.9}$$

with E_D the energy dissipation per unit discharge across the bore. To obtain the physically meaningful solution, we have to assume that the energy dissipation $Q E_D > 0$ for $h_1 \neq h_2$, since the energy flux $[\![(\tilde{E} + g h^2/2)(\mathbf{u} \cdot \bar{\mathbf{n}})]\!]$ through the bore should always be greater than $[\![V_n \tilde{E}]\!]$ the rate of change of energy at the bore. Further, for uniqueness, we have to assume that the water particles crossing the bore should always lose energy [56]. Hence, for $Q > 0$ we have $h_1 < h_2$ and for $Q < 0$ we have $h_1 > h_2$, since we must have $Q E_D > 0$. This is the energy dissipating condition analogous to the entropy condition for shocks in gas dynamics.

Peregrine [48] shows that the jump in PV $[\![\Pi]\!] = \Pi_1 - \Pi_2$ can be calculated by modification of Kelvin's circulation theorem to obtain

$$[\![\Pi]\!] = \Delta \Pi = -\frac{1}{Q} \frac{\mathrm{d} E_D}{\mathrm{d} \hat{y}} \tag{2.10}$$

with local coordinates $\hat{\mathbf{x}} = (\hat{x}, \hat{y})^T$ and $\hat{y}$ aligned along the tangent of the bore.

Hence, if there was no PV in the water undisturbed by the bore then Π_2 is the new nonzero PV when $Q > 0$ and, vice versa, Π_1 is the new nonzero PV when $Q < 0$.

Bühler [17] shows that only PV anomalies can be generated by bores, such that the total PV remains the same in the absence of sources or sinks of PV other than the bores and hydraulic jumps. In the numerical simulations, we qualitatively verify the generation of PV due to non-uniform energy dissipation along the bore.

2.3 Space-time DG finite element model

2.3.1 Space-time tessellation

The space-time flow domain $\mathcal{E}$ is defined as

$$\mathcal{E} := \{(t, \bar{\mathbf{x}}) | \bar{\mathbf{x}} \in \Omega(t), t_0 < t < T\} \subset \mathbb{R}^3 \tag{2.11}$$

with $\Omega(t) \subset \mathbb{R}^2$ the continuously changing flow domain, t_0 the initial time and T the final time. To tessellate the space-time domain, the time interval $[t_0, T]$ is divided into finite time intervals $I_n = [t_n, t_{n+1}]$ with $n = 0, \ldots, N_T$ and N_T the number of space-time slabs. Now at each time level t_n, we tessellate the flow domain $\Omega(t_n)$ using the open space elements K_{k}^n with closure $\bar{K}_{\mathsf{k}}^n$ to obtain a mesh with N_e spatial elements. The tessellation of the spatial domain is

$$\bar{\mathcal{T}}_{\mathsf{h}}^n := \{K_{\mathsf{k}}^n | \bigcup_{\mathsf{k}=1}^{N_e} \bar{K}_{\mathsf{k}}^n = \bar{\Omega}_{\mathsf{h}} \text{ and } K_{\mathsf{k}}^n \cap K_{\mathsf{k}'}^n = \emptyset \text{ if } \mathsf{k} \neq \mathsf{k}', 1 \leq \mathsf{k}, \mathsf{k}' \leq N_e\}, \tag{2.12}$$

such that the computational space domain $\Omega_{\mathsf{h}} \to \Omega$ as $\mathsf{h} \to 0$, in which h is the radius of the largest circle among the union of circles each just containing an element $K_{\mathsf{k}}^n \in \bar{\mathcal{T}}_{\mathsf{h}}^n$. The space-time tessellation consisting of space-time elements $\mathcal{K}_{\mathsf{k}}^n$ can be obtained by connecting the corresponding spatial elements K_{k}^n and K_{k}^{n-1} of the computational space domain Ω_{h} at times t_n and t_{n-1}.

To calculate the flux through the element boundaries, it is useful to introduce the union of faces $\mathcal{S}_{\mathsf{m}}$, each face either connecting two space-time elements, known as interior face, or a space-time element to the boundary of the space-time domain $\partial\mathcal{E}$, known as boundary face. The union of all faces $\mathcal{S}_{\mathsf{m}}$ is $\Gamma = \Gamma_{int} \cup \Gamma_{bou}$ with Γ_{int} and Γ_{bou} the union of interior and boundary faces, respectively.

To define function spaces and apply quadrature rules later, a mapping $F_K^n : \hat{K} \rightarrow K_{\mathsf{k}}^n$ is defined from a reference element $\hat{K}$ onto each spatial element K_{k}^n as

$$F_K^n : \hat{K} \rightarrow K_{\mathsf{k}}^n : \bar{\zeta} \rightarrow \bar{\mathbf{x}} := \sum_{\mathsf{j}} \bar{\mathbf{x}}_{\mathsf{j}}^n \; \chi_{\mathsf{j}}(\bar{\zeta}) \tag{2.13}$$

with $\bar{\zeta} = (\zeta_1, \zeta_2)$ the reference coordinates, $\bar{\mathbf{x}} = (x, y)$ the spatial coordinates, $\bar{\mathbf{x}}_{\mathsf{j}}^n$ the nodal coordinates and $\chi_{\mathsf{j}}(\bar{\zeta})$ the standard shape functions of the element K_{k}^n. Subsequently, a mapping $G_{\mathcal{K}}^n : \hat{\mathcal{K}} \rightarrow \mathcal{K}_{\mathsf{k}}^n$ is defined from a reference element $\hat{\mathcal{K}}$ onto each space-time element $\mathcal{K}_{\mathsf{k}}^n$ as

$$\begin{aligned} G_{\mathcal{K}}^n : \hat{\mathcal{K}} \rightarrow \mathcal{K}_{\mathsf{k}}^n : \zeta \rightarrow \mathbf{x} := \Big(& \frac{1}{2}\big((1+\zeta_0)t_n + (1-\zeta_0)t_{n-1}\big), \\ & \frac{1}{2}\big((1+\zeta_0)F_K^n(\bar{\zeta}) + (1-\zeta_0)F_K^{n-1}(\bar{\zeta})\big)\Big) \end{aligned} \tag{2.14}$$

with $\zeta = (\zeta_0, \bar{\zeta})$ the space-time reference coordinates and $\zeta_0 = [-1, 1]$.

2.3.2 Function spaces, traces and trace operators

To define the discontinuous Galerkin weak formulation, we introduce the broken space $\mathcal{V}_{\mathsf{h}}^d$ defined as

$$\mathcal{V}_{\mathsf{h}}^d := \{\mathbf{V}_{\mathsf{h}} \; : \; \mathbf{V}_{\mathsf{h}}|_{\mathcal{K}_{\mathsf{k}}^n} \circ G_{\mathcal{K}}^n \in (P^1(\hat{\mathcal{K}}))^d, \; \forall \mathcal{K}_{\mathsf{k}}^n\} \tag{2.15}$$

with P^1 the space of linear polynomials, $d = \dim(\mathbf{V}_{\mathsf{h}})$ and $\mathbf{V}_{\mathsf{h}}$ the polynomial approximation per space-time element defined as

$$\mathbf{V}_{\mathsf{h}} := \sum_{m=0}^{M-1} \hat{\mathbf{V}}_m \, \psi_m(\mathbf{x}), \tag{2.16}$$

where $\hat{\mathbf{V}}_m$ is the expansion coefficient, $\psi_m(\mathbf{x})$ the polynomial basis functions and M the number of basis functions. The polynomial basis functions are first defined on reference element $\hat{\mathcal{K}}$ as

$$\hat{\phi}_m : \hat{\mathcal{K}} \rightarrow \mathbb{R} := \{1,\ \zeta_0,\ \zeta_1,\ \zeta_2,\ \zeta_1\zeta_2,\ \zeta_0\zeta_1,\ \zeta_2\zeta_0,\ \zeta_0\zeta_1\zeta_2\}, m = 0, \ldots, 7, \tag{2.17}$$

and then transformed onto each space-time element $\mathcal{K}^n_{\mathsf{k}}$ as $\phi_m : \mathcal{K}^n_{\mathsf{k}} \rightarrow \mathbb{R}$ using the mapping $G^n_{\mathcal{K}}$. We either take $M = 5$ for fixed meshes or $M = 8$ for dynamic meshes. To define the numerical dissipation near discontinuities, we split the function $\mathbf{V}_{\mathsf{h}}$ into a mean $\bar{\mathbf{V}}_{\mathsf{h}} = \hat{\mathbf{V}}_0$ and a fluctuating part $\tilde{\mathbf{V}}_{\mathsf{h}} = \sum_{m=1}^{M-1} \hat{\mathbf{V}}_m \psi_m$ at $t_n^- := \lim_{\epsilon \uparrow 0}(t_n + \epsilon)$. The splitting is obtained by introducing the basis functions as

$$\psi_m(\mathbf{x}) : \mathcal{K}^n_{\mathsf{k}} \rightarrow \mathbb{R} := \begin{cases} 1 & m = 0 \\ \phi_m(\mathbf{x}) - \frac{1}{|K^n_{\mathsf{k}}|} \int_{K^n_{\mathsf{k}}} \phi_m(t_n^-, \bar{\mathbf{x}})\, \mathrm{d}K & \text{otherwise} \end{cases} \tag{2.18}$$

with $|K^n_{\mathsf{k}}| = \int_{K^n_{\mathsf{k}}} dK$ the area of the element K_{k} at time t_n. The mean of the function $\mathbf{V}_{\mathsf{h}}$ can now be defined as $\bar{\mathbf{V}}_{\mathsf{h}} := \int_{K^n_{\mathsf{k}}} \mathbf{V}_{\mathsf{h}} \mathrm{d}K / |K^n_{\mathsf{k}}|$ since the fluctuating part has the following property

$$\int_{K^n_{\mathsf{k}}} \tilde{\mathbf{V}}_{\mathsf{h}} \mathrm{d}K = 0. \tag{2.19}$$

It should be noted that the numerical dissipation usually acts on the expansion coefficients of the fluctuating part and because of property (2.19), the mean remains the same and ensures conservation.

The trace of the function $\mathbf{V}_{\mathsf{h}}$ on the element boundary $\partial\mathcal{K}^n_{\mathsf{k}}$ taken from the inside of the space-time element $\mathcal{K}^n_{\mathsf{k}}$ is defined as

$$\mathbf{V}_{\mathsf{h}}(\mathbf{x})|_{\partial\mathcal{K}^n_{\mathsf{k}}} = \mathbf{V}^- := \lim_{\epsilon \uparrow 0} \mathbf{V}_{\mathsf{h}}(\mathbf{x} + \epsilon \mathbf{n}_{\mathcal{K}}) \tag{2.20}$$

with $\mathbf{n}_{\mathcal{K}}$ the outward unit normal vector of the boundary $\partial\mathcal{K}^n_{\mathsf{k}}$. Since $\mathbf{V}_{\mathsf{h}} \in \mathcal{V}^d_{\mathsf{h}}$, *i.e.,* the functions are approximated per space-time element $\mathcal{K}^n_{\mathsf{k}}$, the traces of the function taken from the inside of any two adjacent elements are discontinuous. Hence, on each face $\mathcal{S}_{\mathsf{m}}$ connecting the element $\mathcal{K}^l$ from left and $\mathcal{K}^r$ from right, it is convenient to introduce the following weighted average $\{\!\{\cdot\}\!\}$ and jump $[\![\cdot]\!]$ trace operators:

Definition 2.3.1. *The weighted average* $\{\!\{F\}\!\}_{\alpha,\beta}$ *of a scalar function* $F \in \mathcal{V}_{\mathsf{h}}^d$ *on the face* $\mathcal{S}_{\mathsf{m}} \in \Gamma_{int}$ *is defined as:*

$$\{\!\{F\}\!\}_{\alpha,\beta} := (\alpha F^l + \beta F^r) \tag{2.21}$$

with $\alpha + \beta = 1$, *and* F^l *and* F^r *the traces of the scalar function* F *taken from the inside of elements* $\mathcal{K}^l$ *and* $\mathcal{K}^r$, *respectively. The weighted average* $\{\!\{\mathbf{G}\}\!\}_{\alpha,\beta}$ *of a vector function* $\mathbf{G} \in \mathcal{V}_{\mathsf{h}}^d$ *on* $\mathcal{S}_{\mathsf{m}} \in \Gamma_{int}$ *is defined as:*

$$\{\!\{\mathbf{G}\}\!\}_{\alpha,\beta} := \alpha \mathbf{G}^l + \beta \mathbf{G}^r \tag{2.22}$$

with $\mathbf{G}^l$ *and* $\mathbf{G}^r$ *the traces of the vector function* $\mathbf{G}$ *from the inside of elements* $\mathcal{K}^l$ *and* $\mathcal{K}^r$, *respectively.*

Definition 2.3.2. *The jump* $[\![F]\!]$ *of a scalar function* $F \in \mathcal{V}_{\mathsf{h}}^d$ *on* $\mathcal{S}_{\mathsf{m}} \in \Gamma_{int}$ *is defined as:*

$$[\![F]\!] := (F^l \mathbf{n}_{\mathcal{K}}^l + F^r \mathbf{n}_{\mathcal{K}}^r) \tag{2.23}$$

with $\mathbf{n}_{\mathcal{K}}^l$ *and* $\mathbf{n}_{\mathcal{K}}^r$ *the outward unit normal vectors of the face* $\mathcal{S}_{\mathsf{m}}$ *w.r.t. elements* $\mathcal{K}^l$ *and* $\mathcal{K}^r$, *respectively. Note that* $\mathbf{n}_{\mathcal{K}}^l = -\mathbf{n}_{\mathcal{K}}^r$. *The jump* $[\![\mathbf{G}]\!]$ *of a vector function* $\mathbf{G} \in \mathcal{V}_{\mathsf{h}}^d$ *on* $\mathcal{S}_{\mathsf{m}} \in \Gamma_{int}$ *is defined as:*

$$[\![\mathbf{G}]\!] := \mathbf{G}^l \cdot \mathbf{n}_{\mathcal{K}}^l + \mathbf{G}^r \cdot \mathbf{n}_{\mathcal{K}}^r. \tag{2.24}$$

Now the following proposition holds between jumps and averages:

Proposition 2.3.3. *For any arbitrary scalar function* $F \in \mathcal{V}_{\mathsf{h}}^d$ *and vector function* $\mathbf{G} \in \mathcal{V}_{\mathsf{h}}^d$, *the following relation holds for the traces on* $\mathcal{S}_{\mathsf{m}} \in \Gamma_{int}$*:*

$$F^l(\mathbf{G}^l \cdot \mathbf{n}_{\mathcal{K}}^l) + F^r(\mathbf{G}^r \cdot \mathbf{n}_{\mathcal{K}}^r) = \{\!\{F\}\!\}_{\alpha,\beta}[\![\mathbf{G}]\!] + [\![F]\!] \cdot \{\!\{\mathbf{G}\}\!\}_{\beta,\alpha}, \quad \mathcal{S}_{\mathsf{m}} \in \Gamma_{int}. \tag{2.25}$$

Proof. Evaluate the left-hand side of (2.25) by using the fact $\mathbf{n}_{\mathcal{K}}^l = -\mathbf{n}_{\mathcal{K}}^r$, rearranging the terms and using definitions (2.21) to (2.24), to find

$$\begin{aligned} F^l(\mathbf{G}^l \cdot \mathbf{n}^l) + F^r(\mathbf{G}^r \cdot \mathbf{n}^r) =& F^l(\mathbf{G}^l \cdot \mathbf{n}^l) - F^r(\mathbf{G}^r \cdot \mathbf{n}^l) \\ \overset{F(\mathbf{G}\cdot\mathbf{n})=\mathbf{G}\cdot(F\mathbf{n})}{=}& (\alpha F^l + \beta F^r)(\mathbf{G}^l \cdot \mathbf{n}^l - \mathbf{G}^r \cdot \mathbf{n}^l) \\ &+ (\beta \mathbf{G}^l + \alpha \mathbf{G}^r) \cdot (\mathbf{n}^l F^l - \mathbf{n}^l F^r) \\ =& \{\!\{F\}\!\}_{\alpha,\beta}[\![\mathbf{G}]\!] + [\![F]\!] \cdot \{\!\{\mathbf{G}\}\!\}_{\beta,\alpha}. \end{aligned} \tag{2.26}$$

□

2.3.3 Discontinuous Galerkin weak formulation

The discontinuous Galerkin weak formulation per space-time element $\mathcal{K}_{\mathsf{k}}^n$ is obtained by multiplying the shallow water equations (2.1) with arbitrary test functions $\mathbf{W}_{\mathsf{h}} \in \mathcal{V}_{\mathsf{h}}^d$, integrating by parts over space-time element $\mathcal{K}_{\mathsf{k}}^n$, using Gauss' theorem in space and time, and introducing the shorthand notation $\mathcal{F}_i(\mathbf{U}_{\mathsf{h}}^-) = \mathcal{F}_i^-$. We obtain then the weak formulation

$$\int_{\partial\mathcal{K}_{\mathsf{k}}^n} \mathbf{n}_{\mathcal{K}} \cdot (W_{\mathsf{h}i}^- \mathcal{F}_i^-) \mathrm{d}(\partial\mathcal{K}) - \int_{\mathcal{K}_{\mathsf{k}}^n} \nabla W_{\mathsf{h}i} \cdot \mathcal{F}_i(\mathbf{U}_{\mathsf{h}}) \,\mathrm{d}\mathcal{K} - \int_{\mathcal{K}_{\mathsf{k}}^n} W_{\mathsf{h}i}\, S_i \,\mathrm{d}\mathcal{K} = 0. \tag{2.27}$$

After summation of the weak formulation (2.27) over all space-time elements $\mathcal{K}_{\mathsf{k}}^n$ in the space-time interval I_n, we can rearrange the element boundary integrals into a summation of interior face integrals and boundary face integrals, and use relation (2.25) to get

$$\begin{aligned}\sum_{\mathcal{K}} \int_{\partial\mathcal{K}_{\mathsf{k}}^n} \mathbf{n}_{\mathcal{K}} \cdot (W_{\mathsf{h}i}^- \mathcal{F}_i^-) \,\mathrm{d}(\partial\mathcal{K}) &= \sum_{\mathcal{S}\in\Gamma_{bou}} \int_{\mathcal{S}_{\mathsf{m}}} W_{\mathsf{h}i}^l (\mathbf{n}_{\mathcal{K}}^l \cdot \mathcal{F}_i^l) \,\mathrm{d}\mathcal{S} \\ &+ \sum_{\mathcal{S}\in\Gamma_{int}} \Big\{ \int_{\mathcal{S}_{\mathsf{m}}} (\{\!\{\mathcal{F}_i\}\!\}_{\alpha,\beta} \cdot [\![W_{\mathsf{h}i}]\!] + [\![\mathcal{F}_i]\!] \{\!\{W_{\mathsf{h}i}\}\!\}_{\beta,\alpha}) \,\mathrm{d}\mathcal{S} \Big\},\end{aligned} \tag{2.28}$$

where $\mathcal{F}^K$, $\mathbf{U}_{\mathsf{h}}^K$ and $\mathbf{W}_{\mathsf{h}}^K$ are the limiting trace values on the face $\mathcal{S}_{\mathsf{m}}$ taken from the inside of the element $\mathcal{K}^K, K = l$ or r; and, $\mathbf{n}_{\mathcal{K}}^K$ is the outward unit normal vector. Now, we enforce the continuity of the flux $[\![\mathcal{F}_i]\!] = 0$ and introduce a consistent and conservative numerical flux

$$\hat{F}_i(\mathbf{U}_{\mathsf{h}}^l, \mathbf{U}_{\mathsf{h}}^r, \mathbf{n}_{\mathcal{K}}) \approx \mathbf{n}_{\mathcal{K}} \cdot \begin{cases} \{\!\{\mathcal{F}_i\}\!\}_{\alpha,\beta} & \text{for } \mathcal{S}_{\mathsf{m}} \in \Gamma_{int} \\ \mathcal{F}_i^l & \text{for } \mathcal{S}_{\mathsf{m}} \in \Gamma_{bou} \end{cases} \tag{2.29}$$

in which the boundary data $\mathbf{U}_{\mathsf{h}}^b = \mathbf{U}_{\mathsf{h}}^r$ are applied at $\mathcal{S}_{\mathsf{m}} \in \Gamma_{bou}$. After introducing the numerical flux (2.29) into (2.28), we obtain the weak formulation

$$\begin{aligned}&\sum_{\mathcal{S}} \int_{\mathcal{S}_{\mathsf{m}}} \hat{F}_i(\mathbf{U}_{\mathsf{h}}^l, \mathbf{U}_{\mathsf{h}}^r, \mathbf{n}_{\mathcal{K}}^l)(W_{\mathsf{h}i}^l - W_{\mathsf{h}i}^r) \,\mathrm{d}\mathcal{S} - \\ &\qquad \sum_{\mathcal{K}} \Big\{ \int_{\mathcal{K}_{\mathsf{k}}^n} \nabla W_{\mathsf{h}i} \cdot \mathcal{F}_i(\mathbf{U}_{\mathsf{h}}) \,\mathrm{d}\mathcal{K} + \int_{\mathcal{K}_{\mathsf{k}}^n} W_{\mathsf{h}i}\, S_i \,\mathrm{d}\mathcal{K} \Big\} = 0 \quad \forall \quad \mathbf{W}_{\mathsf{h}} \in \mathcal{V}_{\mathsf{h}}^{\mathrm{d}},\end{aligned} \tag{2.30}$$

in which we have combined the interior and boundary face integrals by keeping in mind that $W_{\mathsf{h}i}^r = 0$ when $\mathcal{S}_\mathsf{m} \in \Gamma_{bou}$. In section 2.3.5, we will define the normal numerical flux $\hat{F}_i(\mathbf{U}_\mathsf{h}^l, \mathbf{U}_\mathsf{h}^r, \mathbf{n}_\mathcal{K})$ through the faces. The weak formulation (2.30) is akin to the numerical implementation in which we loop separately over faces and elements to calculate the face and element integrals.

2.3.4 Numerical dissipation near bores and jumps

The shallow water equations (2.1) are hyperbolic and hence its weak formulation (2.30) admits discontinuous solutions in the form of bores and hydraulic jumps. In numerical discretizations of the weak formulation (2.30), spurious oscillations generally appear near discontinuities. To suppress these spurious oscillations, we extend and apply the dissipation operator of Van der Vegt and Van der Ven [64] into the weak formulation per space-time element $\mathcal{K}_\mathsf{k}^n$ as

$$\mathcal{D}_\mathsf{k}^n(\mathbf{W}_\mathsf{h}, \mathbf{U}_\mathsf{h}; \mathbf{U}_\mathsf{h}^*) := \int_{\mathcal{K}_\mathsf{k}^n} (\nabla U_{\mathsf{h}i})^T \, \mathfrak{D}_\mathsf{k}^n(\mathbf{U}_\mathsf{h}, \mathbf{U}_\mathsf{h}^*) \, (\nabla W_{\mathsf{h}i}) \, \mathrm{d}\mathcal{K}, \tag{2.31}$$

where $\mathfrak{D}_\mathsf{k}^n(\mathbf{U}_\mathsf{h}, \mathbf{U}_\mathsf{h}^*)$ is the diagonal dissipation matrix, $\mathbf{U}_\mathsf{h}$ the solution in $\mathcal{K}_\mathsf{k}^n$ and $\mathbf{U}_\mathsf{h}^*$ the solution in the immediate neighboring elements of $\mathcal{K}_\mathsf{k}^n$. The dissipation operator (2.31) acts in every space-time element $\mathcal{K}_\mathsf{k}^n$ but is only required around discontinuities and sharp gradients.

The evaluation of the numerical dissipation operator $\mathcal{D}_\mathsf{k}^n(\mathbf{W}_\mathsf{h}, \mathbf{U}_\mathsf{h}, \mathbf{U}_\mathsf{h}^*)$ is more straightforward in the reference coordinate directions than in the physical space coordinates, so we transform (2.31) onto the reference element as

$$\mathcal{D}_\mathsf{k}^n(\mathbf{W}_\mathsf{h}, \mathbf{U}_\mathsf{h}; \mathbf{U}_\mathsf{h}^*) := \int_{\hat{\mathcal{K}}} (\hat{\nabla} U_{\mathsf{h}i})^T \Big(J^{-1} \, \mathfrak{D}_\mathsf{k}^n(\mathbf{U}_\mathsf{h}, \mathbf{U}_\mathsf{h}^*) \, (J^T)^{-1} \Big) (\hat{\nabla} W_{\mathsf{h}i}) \, |J| \mathrm{d}\hat{\mathcal{K}} \tag{2.32}$$

with J the Jacobian matrix defined as $J_{kl} := \partial x_k / \partial \zeta_l$, $|J|$ the determinant of the Jacobian matrix, $\hat{\nabla} = (\partial_{\zeta_0}, \partial_{\zeta_1}, \partial_{\zeta_2})^T$ the differential operator with the relation $\hat{\nabla} = J^T \nabla$. Now, we introduce the dissipation matrix $\tilde{\mathfrak{D}}_\mathsf{k}^n(\mathbf{U}_\mathsf{h}, \mathbf{U}_\mathsf{h}^*)$ on the reference element as

$$\tilde{\mathfrak{D}}_\mathsf{k}^n(\mathbf{U}_\mathsf{h}, \mathbf{U}_\mathsf{h}^*) := J^{-1} \mathfrak{D}_\mathsf{k}^n(\mathbf{U}_\mathsf{h}, \mathbf{U}_\mathsf{h}^*) (J^T)^{-1}. \tag{2.33}$$

To evaluate (2.32), instead of computing $\tilde{\mathfrak{D}}^n_{\mathsf{k}}(\mathbf{U}_{\mathsf{h}}, \mathbf{U}^*_{\mathsf{h}})$ at each Gauss' point we compute it only at the midpoint of the reference element $\zeta = (0,0,0)$. Also, the Jacobian matrix is diagonalized as $J = \text{diag}\{\mathsf{c}_0, \mathsf{c}_1, \mathsf{c}_2\}/2$ with $\mathsf{c}_k = 2\sum_{l=0}^{3} \partial x_k/\partial\zeta_l$ at $\zeta = (0,0,0)$ to reduce the computational effort. The factor 2 introduced in the diagonalization of the Jacobian J makes the parameter c_k into the size of the element $\mathcal{K}^n_{\mathsf{k}}$ in the physical coordinate direction x_k. Since $\mathfrak{D}^n_{\mathsf{k}}(\mathbf{U}_{\mathsf{h}}, \mathbf{U}^*_{\mathsf{h}})$ is a diagonal matrix, the dissipation matrix (2.33) is simplified to

$$\tilde{\mathfrak{D}}^n_{\mathsf{k};kl}(\mathbf{U}_{\mathsf{h}}, \mathbf{U}^*_{\mathsf{h}})|_{\zeta=(0,0,0)} := \frac{4}{\mathsf{c}_k^2}\mathfrak{D}^n_{\mathsf{k},kk}(\mathbf{U}_{\mathsf{h}}, \mathbf{U}^*_{\mathsf{h}}) \text{ for } k = l, \text{ and } 0 \text{ for } k \neq l. \tag{2.34}$$

Jaffre et al. [26] proposed a diagonal dissipation matrix $\mathfrak{D}^n_{\mathsf{k}}(\mathbf{U}_{\mathsf{h}}, \mathbf{U}^*_{\mathsf{h}})$ for hyperbolic conservation laws, which is defined as

$$\mathfrak{D}^n_{\mathsf{k};kk}|_{(\zeta=0,0,0)} := \begin{cases} \max\left(C_2\mathsf{c}_{\mathcal{K}}^{2-\gamma}\mathcal{R}^n_{\mathsf{k}}(\mathbf{U}_{\mathsf{h}}, \mathbf{U}^*_{\mathsf{h}}), C_1\mathsf{c}_{\mathcal{K}}^{1.5}\right), & \text{if } k = 1,2 \\ 0, & \text{if } k = 0 \end{cases} \tag{2.35}$$

for the shallow water equations with

$$\begin{aligned} \mathcal{R}^n_{\mathsf{k}}(\mathbf{U}_{\mathsf{h}}, \mathbf{U}^*_{\mathsf{h}}) := \max_i \Big(\max_{\mathbf{x}\in\mathcal{K}^n_{\mathsf{k}}} \|\nabla\cdot\mathcal{F}_i(\mathbf{U}_{\mathsf{h}})\| \Big) \\ + \sum_{\mathcal{S}_{\mathsf{m}}\subset\partial\mathcal{K}^n_{\mathsf{k}}} C_0 \max_i \Big(\max_{\mathbf{x}\in\mathcal{S}_{\mathsf{m}}} \|\mathbf{n}^l_{\mathcal{K}}\cdot(\mathcal{F}^l_i - \mathcal{F}^r_i)\|/\mathsf{c}_{\mathcal{K}} \Big), \end{aligned} \tag{2.36}$$

$\mathsf{c}_{\mathcal{K}} = \min(\mathsf{c}_1, \mathsf{c}_2)$ a scaling factor, $\max_{\mathbf{x}\in\mathcal{K}^n_{\mathsf{k}}}\|\cdot\|$ is based on the midpoint of the reference element, $\max_{\mathbf{x}\in\mathcal{S}_{\mathsf{m}}}\|\cdot\|$ is based on the midpoint of the face of the reference element, and C_i for $i = 0,1,2$ and γ are positive constants. The positive constants are taken from [64] as $C_0 = 1.2$ if the normal of the face $\mathcal{S}_{\mathsf{m}}$ is parallel to the time direction or else $C_0 = 1.0$, $C_1 = 0.1$, $C_2 = 1.0$ and $\gamma = 0.1$. (In general, the constant C_2 is chosen between 0.1 and 10.) According to [26], the positive constant C_2 can be tuned depending upon the desired quality of solution.

Krivodonova et al. [33] proposed a discontinuity detector scheme, to apply numerical dissipation (2.31) only near discontinuities. We adopt the

Krivodonova discontinuity detector for the shallow water equations as follows

$$\mathcal{I}_{\mathsf{k}}^{n}(h_{\mathsf{h}}, h_{\mathsf{h}}^{*}) := \frac{\sum\limits_{\mathcal{S}_m \in \partial\mathcal{K}_{\mathsf{k}}^{n}} \int_{\mathcal{S}_m} |h_{\mathsf{h}}^{+} - h_{\mathsf{h}}^{-}| \mathrm{d}\mathcal{S}}{\mathsf{h}_{\mathcal{K}}^{(p+1)/2} \, |\partial\mathcal{K}_{\mathsf{k}}^{n}| \, \max\|h_{\mathsf{h}}\|}, \tag{2.37}$$

where h_{h} is the approximated water depth, $\mathsf{h}_{\mathcal{K}}$ the cell measure defined as the radius of the largest circumscribed circle in the element $\mathcal{K}_{\mathsf{k}}^{n}$, $|\partial\mathcal{K}_{\mathsf{k}}^{n}|$ the surface area of the element, and $\max\|\cdot\|$ the maximum norm based on local Gauss' integration points in the element $\mathcal{K}_{\mathsf{k}}^{n}$. Now the space-time elements in non-smooth and smooth regions are detected by $\mathcal{I}_{\mathsf{k}}^{n} > 1$ and $\mathcal{I}_{\mathsf{k}}^{n} < 1$, respectively.

The weak formulation (2.30) is combined with the dissipation operator (2.31) based on the discontinuity detector (2.37) as follows:
Find a $\mathbf{U}_{\mathsf{h}} \in \mathcal{V}_{\mathsf{h}}^{d}$ *such that for all* $\mathbf{W}_{\mathsf{h}} \in \mathcal{V}_{\mathsf{h}}^{d}$

$$\sum_{\mathcal{S}} \Big\{ \int_{\mathcal{S}_{\mathsf{m}}} \hat{F}_i(\mathbf{U}_{\mathsf{h}}^{l}, \mathbf{U}_{\mathsf{h}}^{r}, \mathbf{n}_{\mathcal{K}})(W_{\mathsf{h}i}^{l} - W_{\mathsf{h}i}^{r}) \, \mathrm{d}\mathcal{S} - \sum_{\mathcal{K}} \Big\{ \int_{\mathcal{K}_{\mathsf{k}}^{n}} \nabla W_{\mathsf{h}i} \cdot \mathcal{F}_i(\mathbf{U}_{\mathsf{h}}) \, \mathrm{d}\mathcal{K} + \int_{\mathcal{K}_{\mathsf{k}}^{n}} W_{\mathsf{h}i} \, S_i \, \mathrm{d}\mathcal{K} - \Theta(\mathcal{I}_{\mathsf{k}}^{\mathrm{n}} - 1)\mathcal{D}_{\mathsf{k}}^{\mathrm{n}}(\mathbf{U}_{\mathsf{h}}, \mathbf{U}_{\mathsf{h}}^{*}) \Big\} = 0 \tag{2.38}$$

is satisfied with $\Theta(\mathcal{I}_{\mathsf{k}}^{n} - 1)$ *the Heaviside function.*

2.3.5 Numerical HLLC flux

In the weak formulation (2.30), we introduced the approximate numerical flux $\hat{\mathcal{F}}(\mathbf{U}_{\mathsf{h}}^{l}, \mathbf{U}_{\mathsf{h}}^{r}, \mathbf{n}_{\mathcal{K}})$ because the solution vector $\mathbf{U}_{\mathsf{h}}$ is discontinuous at the element face, as in Fig. 2.2. The numerical flux is usually given by the solution of the Riemann problem identified with the trace values $\mathbf{U}_{\mathsf{h}}^{l,r}$ directly on either side of the face. Since the solution of Riemann problem is computationally expensive, approximate Riemann solvers are used in practice. The HLLC solver in [61] is such an efficient and approximate Riemann solver. In [9], the HLLC solver was improved with appropriate choices of acoustic and contact wave velocities for the Euler equations. Further in [64], this solver was extended to dynamic grids. We show here that the HLLC flux can be derived in space-time without making any explicit difference

between space and time such that the resulting flux is applicable at all the faces of the space-time element. The approach applies the HLLC-technique in pseudo-time τ and the direction χ of the outward normal in a space-time element.

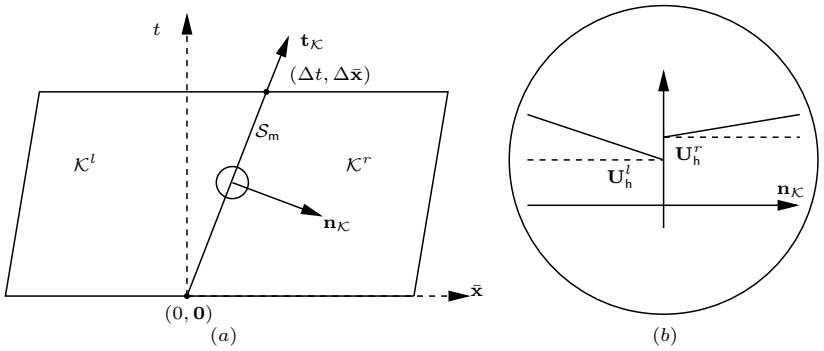

Figure 2.2: (a) Geometry at a face $\mathcal{S}_{\mathsf{m}}$ connecting the space-time elements $\mathcal{K}^l$ and $\mathcal{K}^r$. (b) Local Riemann problem at a face.

To analyze the HLLC flux through the face $\mathcal{S}_{\mathsf{m}}$, we first have to understand the geometry at the face $\mathcal{S}_{\mathsf{m}}$ connecting the space-time elements $\mathcal{K}^l$ and $\mathcal{K}^r$. For convenience, let us take the coordinate axis with the origin located at the bottom corner of the face $\mathcal{S}_{\mathsf{m}}$ as in Fig. 2(a). Now, the top corner of the face $\mathcal{S}_{\mathsf{m}}$ can be taken $(\Delta t, \Delta\bar{\mathbf{x}})$ with $\Delta\bar{\mathbf{x}} = (\Delta x, \Delta y)$ the displacement of the top corner from the bottom corner in the x and y directions, respectively. The tangential vector $\mathbf{t}_{\mathcal{K}}$ along the face can be taken as $(\Delta t, \Delta\bar{\mathbf{x}})^T$. Since the tangential and normal vectors are orthogonal, we have

$$n_t = -\bar{\mathbf{n}}_{\mathcal{K}} \cdot \Delta\bar{\mathbf{x}}/\Delta t = -\bar{\mathbf{n}}_{\mathcal{K}} \cdot \mathbf{v}_g = -v_g/\sqrt{1+v_g^2} \tag{2.39}$$

with $\mathbf{n}_{\mathcal{K}} = (n_t, \bar{\mathbf{n}}_{\mathcal{K}})$ the unit space-time normal vector of the face $\mathcal{S}_{\mathsf{m}}$, $\bar{\mathbf{n}}_{\mathcal{K}} = (n_x, n_y) = (\tilde{n}_x, \tilde{n}_y)/\sqrt{1+v_g^2}$, $\tilde{\mathbf{n}}_{\mathcal{K}} = (\tilde{n}_x, \tilde{n}_y)$ the spatial normal vector, $\mathbf{v}_g = \Delta\bar{\mathbf{x}}/\Delta t$ the grid velocity, and $v_g = \tilde{\mathbf{n}}_{\mathcal{K}} \cdot \mathbf{v}_g$ the normal grid velocity. To unify the derivation of a space-time numerical flux, we consider the one-dimensional shallow water equations in the direction $\mathbf{n}_{\mathcal{K}}$ normal to a space-time face of an element. By ignoring dependencies in the other directions,

we obtain

$$\partial_\tau \mathbf{U} + \partial_\chi \hat{\mathbf{F}} = 0 \tag{2.40}$$

with $\mathbf{U} = (h, hu, hv)^T$, $\hat{\mathbf{F}} = (hq, huq + n_x P, hvq + n_y P)^T$, effective pressure $P = gh^2/2$, space-time velocity

$$q = n_t + \bar{n}_{\mathcal{K}} \cdot \mathbf{u}, \tag{2.41}$$

χ the coordinate in the direction of $\mathbf{n}_{\mathcal{K}}$, and pseudo-time τ. The spatial HLLC approach of [9] is now applied to (2.40) but in the τ, χ–space. The HLLC wave patterns are sketched in Fig. 2.3(a) in the physical $t, \bar{\mathbf{x}}$–space and in Fig. 2.3(b) in the τ, χ–space. In physical space, the left and right waves are taken as

$$S_l = \min(\tilde{q}_l - a_l, \tilde{q}_r - a_r) \quad \text{and} \quad S_r = \max(\tilde{q}_l + a_l, \tilde{q}_r + a_r) \tag{2.42}$$

with $\tilde{q} = \tilde{\mathbf{n}}_{\mathcal{K}} \cdot \mathbf{u}$ the speed in the spatial normal direction, as in [9], and $a^2 = \partial P / \partial h$. We infer from (2.41) that

$$s_r = (S_r - v_g)/\sqrt{1 + v_g^2} \quad \text{and} \quad s_r = (S_l - v_g)/\sqrt{1 + v_g^2}. \tag{2.43}$$

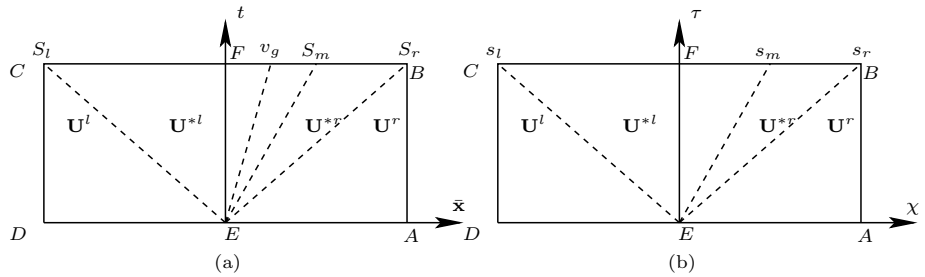

Figure 2.3: (a) HLLC wave pattern in physical space with $v_g = \bar{\mathbf{n}}_{\mathcal{K}} \cdot \mathbf{v}_g$. (b) The HLLC pattern in τ, χ–space.

As usual, four possible cases occur (i) $s_l < 0,\ s_r > 0,\ s_m > 0$; (ii) $s_l < 0,\ s_r > 0,\ s_m < 0$; (iii) $s_l < 0,\ s_r < 0,\ s_m < 0$ and (iv) $s_l > 0,\ s_r >$

0, $s_m > 0$. Combining the HLLC flux for the four cases (as in [9]), but in the τ, χ-space, we obtain

$$\hat{\mathbf{F}}_{\mathrm{HLLC}}(\mathbf{U}^l, \mathbf{U}^r, \mathbf{n}_{\mathcal{K}}) = \frac{1}{2}\Big\{\hat{\mathbf{F}}^l + \hat{\mathbf{F}}^r - (|s_l| - |s_m|)\mathbf{U}^{*l} + (|s_r| - |s_m|)\mathbf{U}^{*r} + |s_l|\mathbf{U}^{\mathbf{l}} - |s_r|\mathbf{U}^r\Big\}, \tag{2.44}$$

where $\hat{\mathbf{F}}^{l,r} = \hat{\mathbf{F}}(\mathbf{U}^{l,r})$. The usual HLLC-expressions for the wave speed s_m and the average intermediate states $\mathbf{U}^{*l}$ and $\mathbf{U}^{*r}$ are given next.

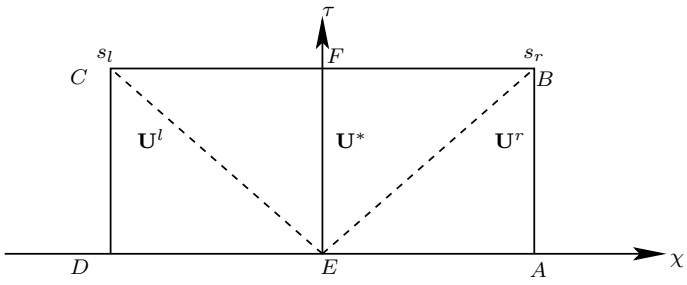

Figure 2.4: Riemann fan for shallow water equations (HLL approach).

As in [9] we assume $s_m = q_l^* = q_r^* = q^*$ where q^* is the average directed velocity between the left and right waves. The q^* can be obtained from the average intermediate state $\mathbf{U}^*$ calculated using HLL approach (see Fig. 2.4). The average intermediate state $\mathbf{U}^*$ is given by

$$\mathbf{U}^* = \Big(s_r\mathbf{U}^r - s_l\mathbf{U}^l - (\hat{\mathbf{F}}^r - \hat{\mathbf{F}}^l)\Big)/(s_r - s_l). \tag{2.45}$$

The wave speed s_m follows from (2.45) as

$$s_m = q^* = \frac{\mathbf{n}_{\mathcal{K}} \cdot \mathbf{U}^*}{h^*} = \frac{h_r q_r(s_r - q_r) - h_l q_l(s_l - q_l) - (n_x^2 + n_y^2)(P_r - P_l)}{h_r(s_r - q_r) - h_l(s_l - q_l)} \tag{2.46}$$

with h^* the average intermediate depth, following from (2.45). By substituting the expressions (2.41) and (2.43) into (2.46), it follows that $s_m =$

$(S_m - v_g)/\sqrt{1+v_g^2}$, as expected heuristically. Here S_m is the expression in [9]; essentially it follows by replacing the space-time variables in (2.46) by their space counterparts as in: $s_m \to S_m, s_r \to S_r, S_l \to s_l, q_l \to \tilde{q}_l$ and $q_r \to \tilde{q}_r$.

The intermediate states U^{*l} and U^{*r} are determined by using the Rankine-Hugoniot relations across left wave and right wave as

$$(s_{l,r} - s_m)\,\mathbf{U}^{*l,*r} = (s_{l,r} - q_{l,r})\,\mathbf{U}^{l,r} + (\hat{\mathbf{P}}^{*l,*r} - \hat{\mathbf{P}}^{l,r}), \tag{2.47}$$

where $\hat{\mathbf{P}}^{*l,*r} = (0, n_x P^*_{l,r}, n_y P^*_{l,r})$ is the average intermediate normal pressure, $P^*_{l,r}$ is the average intermediate pressure obtained by multiplying (2.47) with $\mathbf{n}_\mathcal{K}$ and is given by

$$P^* = P^*_{l,r} = P_{l,r} + (h_{l,r}\,(s_{l,r} - q_{l,r})\,(s_m - q_{l,r}))/(n_x^2 + n_y^2). \tag{2.48}$$

When $s_l > 0$ the flux simplifies to $\hat{\mathbf{F}}_l$ and when $s_r < 0$ to $\hat{\mathbf{F}}_r$, *i.e.* the classic upwind cases.

The expressions (2.43)–(2.48) for our HLLC flux, using

$$\mathbf{n}_\mathcal{K} = (n_t, n_x, n_y) = (-v_g, \tilde{n}_x, \tilde{n}_y)/\sqrt{1+v_g^2}, \tag{2.49}$$

reduce to the expressions in [64]: in comparison our flux is multiplied by a factor $1/\sqrt{1+v_g^2}$ because we included the space-time normal.

In the limit $v_g \to \infty$, we obtain

$$\hat{\mathbf{F}}_{HLLC} = \lim_{v_g \to \infty} \hat{\mathbf{F}}_r = -(h_r, u_r, u_r, h_r v_r)^T. \tag{2.50}$$

This is consistent since we are at the bottom face $t = t_n$ of a space-time element with space-time normal $\mathbf{n}_\mathcal{K} = (-1, 0, 0)^T$, and (2.40) becomes $\partial_\tau \mathbf{U} - \partial_\chi \mathbf{U} = 0$. Causality in time thus reduces to an upwind flux in our unified approach, as expected.

Likewise, we find at the top $t = t_{n+1}$ of the space-time element that $v_g \to -\infty$

$$\hat{\mathbf{F}}_{HLLC} = \lim_{v_g \to -\infty} \hat{\mathbf{F}}_l = (h_l, u_l, u_l, h_l v_l)^T, \tag{2.51}$$

and (2.40) becomes $\partial_\tau \mathbf{U} + \partial_\chi \mathbf{U} = 0$.

2.3.6 Discretized weak formulation: non-linear equations

The weak formulation (2.38) is discretized by substituting the polynomial approximation of the state vector $\mathbf{U}_{\mathsf{h}}$ (2.16) and using the arbitrariness of the test function $\mathbf{W}_{\mathsf{h}}$ as $(\psi_j, 0, 0)$, $(0, \psi_j, 0)$ and $(0, 0, \psi_j)$, $j = 0 \ldots M-1$ with $M = 5$ or $M = 8$. The discretized equations can now be obtained as

$$\sum_{\mathcal{S}_{\mathsf{m}} \subset \partial\mathcal{K}_{\mathsf{k}}^n} \Big\{ \int_{\mathcal{S}_{\mathsf{m}}} \Big(\hat{F}_i(\mathbf{U}_{\mathsf{h}}^l, \mathbf{U}_{\mathsf{h}}^r, \mathbf{n}_{\mathcal{K}}^{\mathsf{k}}) \psi_j \, \mathrm{d}\mathcal{S} \Big\} - \int_{\mathcal{K}_{\mathsf{k}}^n} \nabla\psi_j \cdot \mathcal{F}_i(\mathbf{U}_{\mathsf{h}}) \, \mathrm{d}\mathcal{K} + \Theta(\mathcal{I}_{\mathsf{k}}^n - 1) \times \sum_{m=0}^{4} \hat{U}_{im}^n \int_{\mathcal{K}_{\mathsf{k}}^n} (\nabla\psi_m) \, \mathfrak{D}_{\mathsf{k}}^n(\mathbf{U}_{\mathsf{h}}, \mathbf{U}_{\mathsf{h}}^*) \, (\nabla\psi_j)^T \, \mathrm{d}\mathcal{K} - \int_{\mathcal{K}_{\mathsf{k}}^n} S_i \, \psi_j \, \mathrm{d}\mathcal{K} = 0, \tag{2.52}$$

where $i = 0, 1, 2$ is the index for the shallow water equations, m the index for the expansion coefficients, m the index for the faces and k the index for the elements. The various terms in the non-linear equations (2.52) are represented as follows:

$$\begin{aligned}
E_{\mathsf{k};ij}^{n;\mathcal{K}}(\hat{\mathbf{U}}^n) &= \int_{\mathcal{K}_{\mathsf{k}}^n} \nabla\psi_j \cdot \mathcal{F}_i(\mathbf{U}_{\mathsf{h}}) \, \mathrm{d}\mathcal{K}, \\
F_{\mathsf{m};ij}^{\mathsf{k};\mathcal{S}}(\hat{\mathbf{U}}^n, \hat{\mathbf{U}}^{n-1}) &= \int_{\mathcal{S}_{\mathsf{m}} \subset \partial\mathcal{K}_{\mathsf{k}}^n} \hat{\mathcal{F}}(\mathbf{U}_{\mathsf{h}}^l, \mathbf{U}_{\mathsf{h}}^r, \mathbf{n}_{\mathcal{K}}) \psi_j \, \mathrm{d}\mathcal{S}, \mathsf{k} = l \text{ or } r, \\
D_{\mathsf{k};ij}^{n;\mathcal{K}}(\hat{\mathbf{U}}^n, \hat{\mathbf{U}}^{n-1}) &= \sum_{m=0}^{M-1} \hat{U}_{im}^n \bar{D}_{\mathsf{k};jm}^{n;\mathcal{K}}(\hat{\mathbf{U}}^n, \hat{\mathbf{U}}^{n-1}) \quad \text{with} \\
\bar{D}_{\mathsf{k};jm}^{n;\mathcal{K}}(\hat{\mathbf{U}}^n, \hat{\mathbf{U}}^{n-1}) &= \int_{\mathcal{K}_{\mathsf{k}}^n} (\nabla\psi_m)^T \, \mathfrak{D}_{\mathsf{k}}^n(\mathbf{U}_{\mathsf{h}}, \mathbf{U}_{\mathsf{h}}^*) \, (\nabla\psi_j) \, \mathrm{d}\mathcal{K}, \quad \text{and} \\
G_{\mathsf{k};ij}^{n;\mathcal{K}}(\hat{\mathbf{U}}^n) &= \int_{\mathcal{K}_{\mathsf{k}}^n} \psi_j \, S_i \, \mathrm{d}\mathcal{K}.
\end{aligned} \tag{2.53}$$

The non-linear set of equations (2.52) for each space-time element thus become

$$L^{n;\mathcal{K}}_{\mathsf{k};ij}(\hat{\mathbf{U}}^n;\hat{\mathbf{U}}^{n-1}) = \sum_{\mathcal{S}_\mathsf{m}\subset\partial\mathcal{K}^n_\mathsf{k}} F^{\mathsf{k};\mathcal{S}}_{\mathsf{m};ij} - E^{n;\mathcal{K}}_{\mathsf{k};ij} + \Theta(\mathcal{I}^n_\mathsf{k}-1)D^{n;\mathcal{K}}_{\mathsf{k};ij} - G^{n;\mathcal{K}}_{\mathsf{k};ij} = 0, \tag{2.54}$$

where n represents the space-time level and k represents the index of the space-time element $\mathcal{K}^n_\mathsf{k}$. Given the coefficients $\hat{\mathbf{U}}^{n-1}$ at the previous time level t_{n-1}, we have to find the coefficients $\hat{\mathbf{U}}^n$ satisfying (2.54) at the present time level t_n.

2.3.7 Pseudo-time integration: non-linear solver

To solve the system of non-linear equations (2.54) obtained from the space-time discontinuous Galerkin discretization, we augment these equations with a pseudo-time derivative as

$$|K^n_\mathsf{k}|\frac{\partial\hat{U}_{ij}}{\partial\tau} = -\frac{1}{\Delta t}L^{n;\mathcal{K}}_{\mathsf{k};ij}(\hat{\mathbf{U}};\hat{\mathbf{U}}^{n-1}) \tag{2.55}$$

with $\Delta t = (t_n - t_{n-1})$ the time step and $|K^n_\mathsf{k}| = |\mathcal{K}^n_\mathsf{k}|/\Delta t$. Now we integrate (2.55) until the solution reaches steady state in pseudo-time, *i.e.,*

$$L^{n;\mathcal{K}}_{\mathsf{k};ij}(\hat{\mathbf{U}}^n;\hat{\mathbf{U}}^{n-1}) \approx 0. \tag{2.56}$$

The pseudo-time integration scheme is obtained from a second order accurate five-stage Runge-Kutta scheme by treating $\hat{\mathbf{V}}$ in $L^{n;\mathcal{K}}_\mathsf{k}(\hat{\mathbf{V}};\hat{\mathbf{U}}^{n-1})$ semi-implicitly as

$$\left(I + \frac{\alpha_s\lambda}{|K^n_\mathsf{k}|}\Big(|K^n_\mathsf{k}|I + \Theta(\mathcal{I}^n_\mathsf{k}-1)\bar{D}^{n;\mathcal{K}}_\mathsf{k}(\hat{\mathbf{V}}^{s-1},\hat{\mathbf{U}}^{n-1})\Big)\right)\hat{\mathbf{V}}^s = \hat{\mathbf{V}}^0 + \frac{\alpha_s\lambda}{|K^n_\mathsf{k}|}\times$$
$$\left(\Big(|K^n_\mathsf{k}|I + \Theta(\mathcal{I}^n_\mathsf{k}-1)\bar{D}^{n;\mathcal{K}}_\mathsf{k}(\hat{\mathbf{V}}^{s-1},\hat{\mathbf{U}}^{n-1})\Big)\hat{\mathbf{V}}^{s-1} - L^{n;\mathcal{K}}_\mathsf{k}(\hat{\mathbf{V}}^{s-1};\ \hat{\mathbf{U}}^{n-1})\right), \tag{2.57}$$

where $s = 1, \ldots, 5$ are the Runge-Kutta stages, $\alpha_s = (0.0791451, 0.163551, 0.283663, 0.5, 1.0)$ the Runge-Kutta coefficients, $\lambda = \Delta\tau/\Delta t$ and $\Delta\tau$ the pseudo-time step. The pseudo-time step $\Delta\tau$ is determined locally per space-time element by a CFL condition given as

$$\Delta\tau|_{\mathcal{K}_{\mathsf{k}}^n} = CFL_{\Delta\tau}|K_{\mathsf{k}}^n|/S_{\mathsf{k};\max}^n \tag{2.58}$$

with $S_{\mathsf{k};\max}^n$ the maximum wave speed in the space-time element $\mathcal{K}_{\mathsf{k}}^n$ and $CFL_{\Delta\tau} = 0.8$ the CFL number for the pseudo-time step.

In our numerical computations, we observed that in the presence of discontinuities the residue may oscillate between smooth and non-smooth states resulting in a non-convergent scheme. The main cause of these oscillations is that the pseudo-time integration scheme (2.57) integrates the nonlinear system $L_{\mathsf{k}}^{n;\mathcal{K}} \approx (\bar{A}_{\mathsf{k}}^n + \bar{D}_{\mathsf{k}}^n)\hat{\mathbf{V}} = 0$ when $\mathcal{I}_{\mathsf{k}}^n > 1$, and $L_{\mathsf{k}}^{n;\mathcal{K}} \approx \bar{A}_{\mathsf{k}}^n\hat{\mathbf{V}} = 0$ otherwise, in each space-time element $\mathcal{K}_{\mathsf{k}}^n$. To avoid this, we use a switch $\mathcal{I}'^n_{\mathsf{k}}$ in every space-time element such that $\mathcal{I}'^n_{\mathsf{k}} = -1$ when $\mathcal{I}_{\mathsf{k}}^n < 1$, and $\mathcal{I}'^n_{\mathsf{k}} = 1$ when $\mathcal{I}_{\mathsf{k}}^n > 1$ for pseudo-time steps, whereafter we only switch to $\mathcal{I}'^n_{\mathsf{k}} = 1$ wherever $\mathcal{I}_{\mathsf{k}}^n > 1$ until the solution reaches steady state in pseudo-time. Finally, in the numerical scheme we replace $\Theta(\mathcal{I}_{\mathsf{k}}^n - 1)$ with $\Theta(\mathcal{I}'^n_{\mathsf{k}})$ to achieve convergence.

2.4 Properties and analysis of the numerical discretization

2.4.1 Persistence of the discretized rest state

The shallow water equations at rest satisfy $\mathbf{u} = 0$ for a fixed depth $h(\mathbf{x}) = D(\bar{\mathbf{x}})$ such that $\bar{\nabla}(gh^2/2) = -gh\bar{\nabla}h_b$. For smooth topography $h_b(\bar{\mathbf{x}}) + h(\mathbf{x}) = H$ is constant.

Proposition 2.4.1. *Consider the shallow water equations with a consistent and conservative numerical flux $\hat{F}_i(\mathbf{U}_{\mathsf{h}}^-, \mathbf{U}_{\mathsf{h}}^+, \mathbf{n}_{\mathcal{K}})$ and the weak formulation (2.30). The weak formulation (2.30) exactly satisfies the steady rest state $\mathbf{u} = 0, H = h(\mathbf{x}) + h_b(\bar{\mathbf{x}})$ if:*

1. *The bottom topography $h_b(\bar{\mathbf{x}})$ is approximated smoothly as follows:*

$$\tilde{h}_b(\bar{\mathbf{x}}) = \sum_{0}^{M-1} \hat{h}_{b;m}\psi_m \text{ such that} \tag{2.59}$$

$$h_b(x_k, y_k) = \tilde{h}_b(x_k, y_k) \text{ for } k = 0, 1, 2 \text{ and } 3 \tag{2.60}$$

with $\tilde{h}_b(\bar{\mathbf{x}})$ the approximated topography, ψ_m the basis functions defined in (2.18), $\hat{h}_{b;m}$ the expansion coefficients of the topographic approximation and (x_k, y_k) the nodal coordinates of the spatial element K_{k}. The expansion coefficient corresponding to the time coordinate $\hat{h}_{b;1}$ is taken zero when $M = 5$.

2. *The rest water depth $h(\mathbf{x})$ is approximated as*

$$\tilde{h}(\bar{\mathbf{x}}) = H - \tilde{h}_b(\bar{\mathbf{x}}) = \sum_{m=0}^{M-1} \hat{h}_m\psi_m \tag{2.61}$$

with $\tilde{h}(\bar{\mathbf{x}})$ the approximated water depth and $\hat{h}_m$ the expansion coefficient of the water depth obtained using a (dis)continuous Galerkin projection with $\hat{h}_1 = 0$ for $M = 5$.

3. *The spatial element K^n_{k} is not deforming in time.*

Proof. We give the proof for the case with $M = 5$. The approximated topography $\tilde{h}_b(\bar{\mathbf{x}})$ as given in (2.59) satisfying (2.60) ensures that $\tilde{h}_b(\bar{\mathbf{x}})$ is piecewise continuous and linear along the faces. Hence, $\tilde{h}$ in (2.61) is also piecewise continuous and linear along the faces. Since the velocities are zero, we can now conclude that $\mathbf{U}_{\mathsf{h}} = (\tilde{h}, \tilde{h}u, \tilde{h}v)$ is piecewise continuous and linear along the faces. Also the traces on each element boundary from the inside and outside the element are equal, *i.e.,* $\mathbf{U}_{\mathsf{h}}|_{\partial\mathcal{K}^n_{\mathsf{k}}} = \mathbf{U}^-_{\mathsf{h}} = \mathbf{U}^+_{\mathsf{h}}$. Using the consistency property of numerical flux, we get

$$\tilde{\mathcal{F}}(\mathbf{U}^-_{\mathsf{h}}, \mathbf{U}^+_{\mathsf{h}}, \mathbf{n}_{\mathcal{K}}) = \mathcal{F}(\mathbf{U}_{\mathsf{h}}). \tag{2.62}$$

Substituting (2.62) in (2.30) for every element, we obtain an alternative form of the weak formulation as follows:

$$\int_{\partial\mathcal{K}^n_{\mathsf{k}}} W^-_j \Big(\mathbf{n}_{\mathcal{K}} \cdot \mathcal{F}_i(\mathbf{U}_{\mathsf{h}})\Big) \mathrm{d}(\partial\mathcal{K}) - \int_{\mathcal{K}^n_{\mathsf{k}}} \nabla W_{\mathsf{h}j} \cdot \mathcal{F}_i(\mathbf{U}_{\mathsf{h}}) \mathrm{d}\mathcal{K} - \int_{\mathcal{K}^n_{\mathsf{k}}} W_{\mathsf{h}j}\, S_i \mathrm{d}\mathcal{K} = 0. \tag{2.63}$$

After integrating by parts and applying Gauss' theorem in space and time, we get

$$\int_{\mathcal{K}_{\mathsf{k}}^n} W_{\mathsf{h}i}\Big(\nabla\cdot\mathcal{F}_i(\mathbf{U}_{\mathsf{h}})\Big)\mathrm{d}\mathcal{K} - \int_{\mathcal{K}_{\mathsf{k}}^n} W_{\mathsf{h}i}\, S_i\,\mathrm{d}\mathcal{K} = 0. \tag{2.64}$$

Since $\mathbf{W}_{\mathsf{h}}$ is arbitrary, the approximation $\mathbf{U}_{\mathsf{h}}$ needs to satisfy

$$\nabla\cdot\mathcal{F}_i(\mathbf{U}_{\mathsf{h}}) = S_i. \tag{2.65}$$

Substituting the approximations $\mathbf{U}_{\mathsf{h}}$ in $\nabla\cdot\mathcal{F}_i(\mathbf{U}_{\mathsf{h}})$, we get

$$\partial_t\tilde{h} = \partial_t(H-\tilde{h}_b) = 0, \quad \text{and} \quad \bar{\nabla}(g\tilde{h}^2/2) = g\tilde{h}\bar{\nabla}(H-\tilde{h}_b) = -g\tilde{h}\bar{\nabla}\tilde{h}_b. \tag{2.66}$$

Hence, the steady rest state is satisfied in the discretized equations. □

This strategy to preserve the rest state coincides with the one in [11] and [57], and contrasts with the ones in [7] and [34], because we consider smooth topography. Preservation of the rest state with discontinuous bottom topography and a Galerkin finite element method is found in Rhebergen et al. [50].

2.4.2 Discrete Fourier analysis

For the discrete Fourier analysis of the space-time DG discretization, we consider the one dimensional linearized rotating shallow water equations

$$\partial_t\eta + \partial_x(Hu) = 0, \quad \partial_t u - \mathsf{f}v = -g\partial_x\eta \quad \text{and} \quad \partial_t v + \mathsf{f}u = 0 \tag{2.67}$$

with $\eta(t,x)$ the free surface perturbation around a mean surface depth H, $(u(t,x),v(t,x))$ the velocity field, g the gravitational acceleration and f the Coriolis parameter. These equations can be solved using the following ansatz:

$$\eta(t,x) = Ae^{\imath(kx+\omega t)} \quad \text{and} \quad (u(t,x),v(t,x)) = \frac{-gAk}{(\omega^2-\mathsf{f}^2)}(\omega,\mathsf{f}\imath)e^{\imath(kx+\omega t)} \tag{2.68}$$

yielding the dispersion relation $\omega^2 = a^2k^2+\mathsf{f}^2$ with amplitude A, frequency ω, wave number k, and gravity wave speed $a=\sqrt{gH}$.

To discretize (2.67), we consider one dimensional space-time elements $\mathcal{K}_{\mathsf{k}}^n$ with neighboring elements $\mathcal{K}_{\mathsf{k}-1}^n$ and $\mathcal{K}_{\mathsf{k}+1}^n$ in the x–direction, and $\mathcal{K}_{\mathsf{k}}^{n-1}$ and $\mathcal{K}_{\mathsf{k}}^{n+1}$ in the t–direction. The faces of the space-time element $\mathcal{K}_{\mathsf{k}}^n$ can now be given by $\mathcal{S}_l = \bar{\mathcal{K}}_{\mathsf{k}-1}^n \cap \bar{\mathcal{K}}_{\mathsf{k}}^n$, $\mathcal{S}_r = \bar{\mathcal{K}}_{\mathsf{k}}^n \cap \bar{\mathcal{K}}_{\mathsf{k}+1}^n$, $\mathcal{S}_b = \bar{\mathcal{K}}_{\mathsf{k}}^{n-1} \cap \bar{\mathcal{K}}_{\mathsf{k}}^n$ and $\mathcal{S}_t = \bar{\mathcal{K}}_{\mathsf{k}}^n \cap \bar{\mathcal{K}}_{\mathsf{k}}^{n+1}$ with element boundary $\partial\mathcal{K}_{\mathsf{k}}^n = \mathcal{S}_l \cup \mathcal{S}_r \cup \mathcal{S}_b \cup \mathcal{S}_t$. In each space-time element, we approximate the wave field (η, u, v) as

$$(\eta_{\mathsf{k}}^n, u_{\mathsf{k}}^n, v_{\mathsf{k}}^n) = \sum_{j=0}^{2} (\hat{\eta}_{\mathsf{k},j}^n, \hat{u}_{\mathsf{k},j}^n, \hat{v}_{\mathsf{k},j}^n)\psi_j \tag{2.69}$$

with $(\hat{\eta}_{\mathsf{k},j}^n, \hat{u}_{\mathsf{k},j}^n, \hat{v}_{\mathsf{k},j}^n)$ the expansion coefficients and ψ_j the basis functions. The basis functions ψ_j in the reference elements $\hat{\mathcal{K}}$ are defined as $\hat{\psi} = (1, \zeta_0 - 1, \zeta)$.

To simplify the weak formulation (2.30) per space-time element, we substitute $(\tilde{\eta}, \tilde{u}, \tilde{v}) := (\eta^+, u^-, v^-)$ in the numerical flux evaluation at the elements faces $\mathcal{S}_l$ and $\mathcal{S}_r$, and the upwind flux in the time direction. The weak formulation (2.53) then becomes

$$\begin{aligned}
&-\int_{\mathcal{S}_b} \eta_{\mathsf{k}}^{n-1} w_1^- \,\mathrm{d}\mathcal{S} + \int_{\mathcal{S}_t} \eta_{\mathsf{k}}^n w_1^- \,\mathrm{d}\mathcal{S} - \int_{\mathcal{S}_l} H u_{\mathsf{k}-1}^n w_1^- \,\mathrm{d}\mathcal{S} + \int_{\mathcal{S}_r} H u_{\mathsf{k}}^n w_1^- \,\mathrm{d}\mathcal{S} \\
&\qquad - \int_{\mathcal{K}_{\mathsf{k}}^n} (\partial_t w_1) \eta_{\mathsf{k}}^n \,\mathrm{d}\mathcal{K} - \int_{\mathcal{K}_{\mathsf{k}}^n} (\partial_x w_1) H u_{\mathsf{k}}^n \,\mathrm{d}\mathcal{K} = 0, \\
&-\int_{\mathcal{S}_b} u_{\mathsf{k}}^{n-1} w_2^- \,\mathrm{d}\mathcal{S} + \int_{\mathcal{S}_t} u_{\mathsf{k}}^n w_2^- \,\mathrm{d}\mathcal{S} - \int_{\mathcal{S}_l} g\eta_{\mathsf{k}}^n w_2^- \,\mathrm{d}\mathcal{S} + \int_{\mathcal{S}_r} g\eta_{\mathsf{k}+1}^n w_2^- \,\mathrm{d}\mathcal{S} \\
&\qquad - \int_{\mathcal{K}_{\mathsf{k}}^n} (\partial_t w_2) u_{\mathsf{k}}^n \,\mathrm{d}\mathcal{K} - \int_{\mathcal{K}_{\mathsf{k}}^n} (\partial_x w_2) g\eta_{\mathsf{k}}^n \,\mathrm{d}\mathcal{K} - \int_{\mathcal{K}_{\mathsf{k}}^n} w_2 \mathsf{f} v_{\mathsf{k}}^n \,\mathrm{d}\mathcal{K} = 0, \\
&-\int_{\mathcal{S}_b} v_{\mathsf{k}}^{n-1} w_3^- \,\mathrm{d}\mathcal{S} + \int_{\mathcal{S}_t} v_{\mathsf{k}}^n w_3^- \,\mathrm{d}\mathcal{S} - \int_{\mathcal{K}_{\mathsf{k}}^n} (\partial_t w_3) v_{\mathsf{k}}^n \,\mathrm{d}\mathcal{K} + \int_{\mathcal{K}_{\mathsf{k}}^n} w_3 \mathsf{f} u_{\mathsf{k}}^n \,\mathrm{d}\mathcal{K} = 0
\end{aligned} \tag{2.70}$$

with (w_1, w_2, w_3) the test functions. Substituting the polynomial approxi-

mation (2.69) in (2.70), the numerical discretization is obtained as

$$\begin{aligned} -A_{\mathsf{k}}^n\hat{\eta}_{\mathsf{k}}^{n-1} + B_{\mathsf{k}}^n\hat{\eta}_{\mathsf{k}}^n - HC_{\mathsf{k}}^{n,1}\hat{u}_{\mathsf{k}-1}^n + HD_{\mathsf{k}}^{n,1}\hat{u}_{\mathsf{k}}^n - E_{\mathsf{k}}^n\hat{\eta}_{\mathsf{k}}^n - HF_{\mathsf{k}}^n\hat{u}_{\mathsf{k}}^n &= 0,\\ -A_{\mathsf{k}}^n\hat{u}_{\mathsf{k}}^{n-1} + B_{\mathsf{k}}^n\hat{u}_{\mathsf{k}}^n - gC_{\mathsf{k}}^{n,2}\hat{\eta}_{\mathsf{k}}^n + gD_{\mathsf{k}}^{n,2}\hat{\eta}_{\mathsf{k}+1}^n - E_{\mathsf{k}}^n\hat{u}_{\mathsf{k}}^n - gF_{\mathsf{k}}^n\hat{\eta}_{\mathsf{k}}^n - \mathsf{f}G_{\mathsf{k}}^n\hat{v}_{\mathsf{k}}^n &= 0,\\ -A_{\mathsf{k}}^n\hat{v}_{\mathsf{k}}^{n-1} + B_{\mathsf{k}}^n\hat{v}_{\mathsf{k}}^n - E_{\mathsf{k}}^n\hat{v}_{\mathsf{k}}^n + \mathsf{f}G_{\mathsf{k}}^n\hat{u}_{\mathsf{k}}^n &= 0, \end{aligned} \tag{2.71}$$

where the 3×3 matrices are defined as follows:

$$\begin{aligned} A_{\mathsf{k};ij}^n &:= \int_{\mathcal{S}_b} \psi_j^+\psi_i^-\mathrm{d}\mathcal{S}, \quad B_{\mathsf{k};ij}^n := \int_{\mathcal{S}_t} \psi_j^-\psi_i^-\mathrm{d}\mathcal{S}, \quad C_{\mathsf{k};ij}^{n,1} := \int_{\mathcal{S}_l} \psi_j^+\psi_i^-\mathrm{d}\mathcal{S},\\ C_{\mathsf{k};ij}^{n,2} &:= \int_{\mathcal{S}_l} \psi_j^-\psi_i^-\mathrm{d}\mathcal{S}, \quad D_{\mathsf{k};ij}^{n,1} := \int_{\mathcal{S}_r} \psi_j^-\psi_i^-\mathrm{d}\mathcal{S}, \quad D_{\mathsf{k};ij}^{n,2} := \int_{\mathcal{S}_r} \psi_j^+\psi_i^-\mathrm{d}\mathcal{S},\\ E_{\mathsf{k};ij}^n &:= \int_{\mathcal{K}_{\mathsf{k}}^n} \psi_j(\partial_t\psi_i)\mathrm{d}\mathcal{K}, \quad F_{\mathsf{k};ij}^n := \int_{\mathcal{K}_{\mathsf{k}}^n} \psi_j(\partial_x\psi_i)\mathrm{d}\mathcal{K}, \quad \text{and}\\ G_{\mathsf{k};ij}^n i &:= \int_{\mathcal{K}_{\mathsf{k}}^n} \psi_j\psi_i\mathrm{d}\mathcal{K}. \end{aligned} \tag{2.72}$$

To investigate the stability, dispersion and dissipation error of the numerical scheme, we use a discrete Fourier ansatz for the coefficients of the wave field as

$$(\hat{\eta}_{\mathsf{k}}^n, \hat{u}_{\mathsf{k}}^n, \hat{v}_{\mathsf{k}}^n) := \lambda^n \exp(\imath k\mathsf{k}\Delta x)(\hat{\eta}_F, \hat{u}_F, \hat{v}_F), \tag{2.73}$$

where $(\hat{\eta}_F, \hat{u}_F, \hat{v}_F)$ are the Fourier coefficients. Substituting (2.73) into the discretized equations (2.71), we obtain

$$\begin{aligned} M_{\mathsf{k}}^n\hat{\eta}_F + \lambda H\big(-\exp(-\imath k\Delta x)C_{\mathsf{k}}^{n,1} + D_{\mathsf{k}}^{n,1} - F_{\mathsf{k}}^n\big)\hat{u}_F &= 0,\\ M_{\mathsf{k}}^n\hat{u}_F + \lambda g\big(-C_{\mathsf{k}}^{n,2} + \exp(\imath k\Delta x)D_{\mathsf{k}}^{n,2} - F_{\mathsf{k}}^n\big)\hat{\eta}_F - \lambda\mathsf{f}G_{\mathsf{k}}^n\hat{v}_F &= 0,\\ M_{\mathsf{k}}^n\hat{v}_F + \lambda\mathsf{f}G_{\mathsf{k}}^n\hat{u}_F &= 0 \end{aligned} \tag{2.74}$$

with $M_{\mathsf{k}}^n = -A_{\mathsf{k}}^n + \lambda B_{\mathsf{k}}^n - \lambda E_{\mathsf{k}}^n$. Combining the equations (2.74), we get the following eigen-value problem

$$\Big[M_{\mathsf{k}}^n + \mathsf{f}^2G_{\mathsf{k}}^n(M_{\mathsf{k}}^n)^{-1}G_{\mathsf{k}}^n - (\lambda a)^2H_{\mathsf{k}}^{n,1}(M_{\mathsf{k}}^n)^{-1}H_{\mathsf{k}}^{n,2}\Big]\hat{u}_F = 0 \tag{2.75}$$

with $H_{\mathsf{k}}^{n,1} = -\exp(-\imath k\Delta x)C_{\mathsf{k}}^{n,1} + D_{\mathsf{k}}^{n,1} - F_{\mathsf{k}}^n$ and $H_{\mathsf{k}}^{n,2} = -C_{\mathsf{k}}^{n,2} + \exp(\imath k\Delta x)$ $D_{\mathsf{k}}^{n,2} - F_{\mathsf{k}}^n$. If we take uniform elements of size Δx and Δt then we find

using MAPLE that $(M_{\mathsf{k}}^n)^{-1}$ is of the form $M_1/(\lambda-1)+M_2/(\lambda)$. After some algebraic manipulations, a simplified quadratic eigenvalue problem can be obtained of the following form:

$$\lambda^2 P + \lambda Q + R = 0. \tag{2.76}$$

Using MATLAB, we solve for the eigenvalues λ with $k\Delta x = [0, 2\pi]$, the CFL number $CFL_{\Delta t} = a\Delta t/\Delta x$ and Coriolis parameter f. For a wide range of CFL numbers and Coriolis parameters, we always obtained $\max|\lambda| < 1$, which shows that the scheme is unconditionally stable.

The eigenvalue λ is analogous to the frequency of the harmonic wave as

$$\lambda = \exp(\imath\tilde{\omega}\Delta t) \tag{2.77}$$

with $\tilde{\omega} = \tilde{\omega}_1 + \imath\tilde{\omega}_2$ in which $\tilde{\omega}_1$ is the numerical frequency and $\tilde{\omega}_2$ is the dissipation of the numerical scheme. The dispersion error $|\tilde{\omega}_1 - \omega|$ and dissipation error $\tilde{\omega}_2$ of the numerical scheme can now be given as

$$|\tilde{\omega}_1 - \omega| = |\arg(\lambda) - \omega| \text{ and } \tilde{\omega}_2 = -\frac{\ln(|\lambda|)}{\Delta t}, \tag{2.78}$$

respectively. Some of the eigenvalues of (2.76) will be close to the actual frequencies of the harmonic wave, which we use to compute the dispersion error and dissipation of the numerical scheme. In Figs. 2.5 to 2.7, we have plotted the contours of dispersion and dissipation errors for mesh resolution $k\,\Delta x = [0, 0.25]$, wave frequency resolution $\Omega\Delta t = [0, 0.25]$, Coriolis parameter $\mathsf{f} = 0, 2, 3$ and wave number $k = 1$. We can observe from the plots that the dispersion error and dissipation error decrease with the increase of the mesh resolution and the wave frequency resolution. The exact and numerical dispersion relations in Fig. 2.8 reveal the dispersion error in another way.

2.5 Concluding remarks

A space-time discontinuous Galerkin method for the (rotating) shallow water equations has been presented for shallow flows over varying topography and in time dependent domains. This application of the space-time discontinuous Galerkin method is new. It is especially interesting as a mile stone

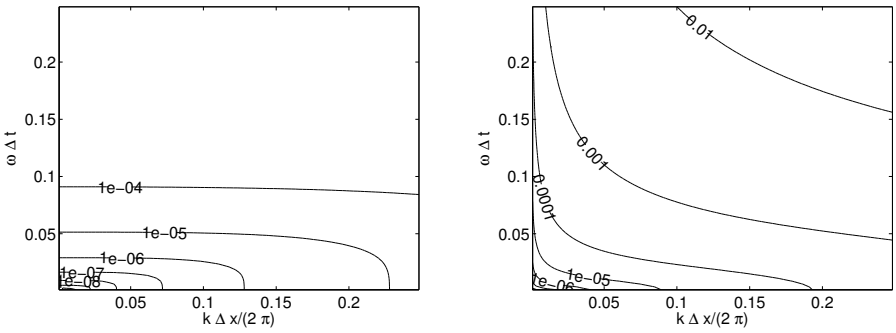

(a) Dispersion error. (b) Dissipation error.

Figure 2.5: $\mathsf{f} = 0$, $ak = 1$ and $\mathsf{f}^2 < a^2k^2$.

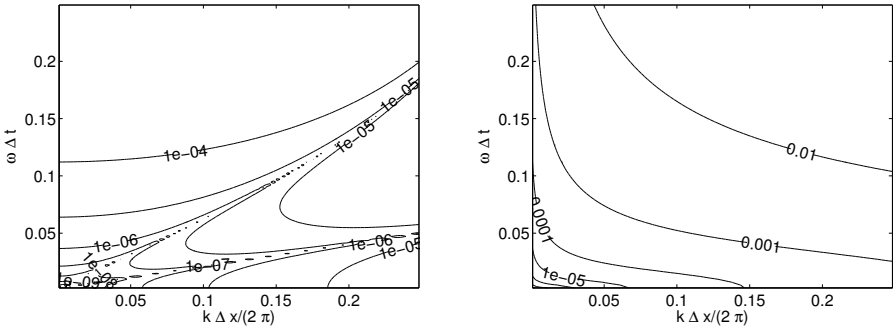

(a) Dispersion error. (b) Dissipation.

Figure 2.6: $\mathsf{f} = 2$, $ak = 1$ and $\mathsf{f}^2 > a^2k^2$.

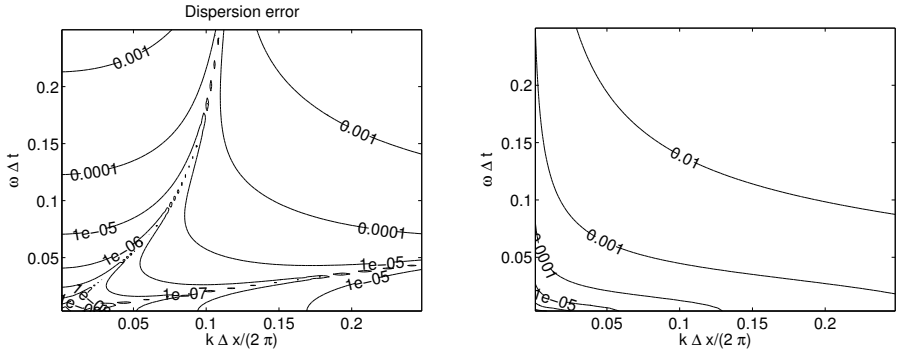

(a) Dispersion error. (b) Dissipation.

Figure 2.7: $\mathsf{f} = 3$, $ak = 1$ and $\mathsf{f}^2 > a^2k^2$.

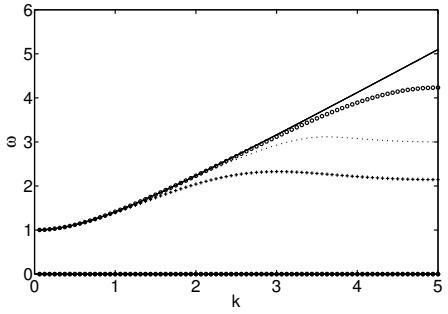

Figure 2.8: Plot of numerical and actual frequencies for different wave numbers k with mesh size $\Delta x = 2\pi/10$ and $\mathsf{f} = 1$. Solid lines correspond to the actual frequency ω and the marks "+", "." and "$\circ$" correspond to the numerical frequencies $\tilde{\omega}_1$ for $\Delta t = 1.0, 0.5$ and 0.05, respectively.

towards accurate numerical modeling of the time evolution of the water line in flooding and drying events. These events are important in the prediction of river floods and near-shore hydrodynamics.

Due to the presence of bores in the shallow water equations spurious oscillations will arise in higher order shock-capturing numerical schemes such as our space-time method. We have limited these spurious oscillations around discontinuities and sharp gradients by applying dissipation but only near discontinuities once these are detected by Krivodonova's discontinuity detector [33]. Furthermore, we showed that our numerical discretization preserves the state of rest for non-uniform topography, by use of a smooth approximation for the topography. A discrete Fourier analysis of the numerical discretization for one-dimensional linearized rotating shallow water equations showed that the scheme was unconditionally stable with small dispersion and dissipation error.

Chapter 3

Applications to Geophysical Flows

3.1 Introduction

The space-time discontinuous Galerkin scheme for shallow water waves presented in chapter 2 is thoroughly verified and validated by considering a number of demanding test cases. The numerical scheme is first verified by comparing the numerical results against some exact solutions. Next, we simulate the harmonic modes of linearized (rotating) shallow water equations, which includes Kelvin and Poincaré modes under low amplitude for a number of time periods to show qualitatively that the scheme has minimal dispersion error and dissipation. To validate the scheme, we consider shallow water flows where the energy is dissipated in the presence of bores or jumps and generate PV anomaly in the case of non-uniform bores (see Peregrine [48] and Pratt [49]). Such bore-vortex interactions are considered as necessary, advanced and demanding test cases in which non-uniform bores are formed and subsequently PV is generated (see, Hu [25]). To show the versatility of the present scheme in dynamic domains, We conside of nearly linear and highly nonlinear waves in a wave basin by prescribing the motion of a flexible domain wall as a wave maker. Finally, we also validate the method qualitatively with an interesting laboratory experiment.

3.2 Boundary conditions

For many numerical examples considered here, the implementation of the boundary condition was very crucial in the numerical scheme. To explain the implementation, let $\mathbf{U}^l = (h^l, h^l u^l, h^l v^l)^T$ be the trace taken from inside the element $\mathcal{K}^l$ connected to the boundary face $\mathcal{S}_\mathsf{m} \in \Gamma_{bou}$, $\mathbf{U}^b = (h^b, h^b u^b, h^b v^b)^T$ the boundary data applied at the boundary face $\mathcal{S}_\mathsf{m}$ and $\mathbf{n}^l_\mathcal{K} = (n_t, \tilde{\mathbf{n}}_\mathcal{K})^T$ the outward unit normal vector of the face $\mathcal{S}_\mathsf{m}$ w.r.t. element $\mathcal{K}^l$. We have implemented the different boundary conditions given $\mathbf{U}^l$ as follows:

Open flow boundary: At an open flow boundary, we simply take $\mathbf{U}^b = \mathbf{U}^l$.

Solid wall: Consider the momentum equations in primitive variables $\mathbf{u}$ as

$$\partial_t \mathbf{u} + (\mathbf{u} \cdot \nabla)\mathbf{u} = -\mathsf{f}\mathbf{u}^\perp - g\nabla(h + h_b) \tag{3.1}$$

with $\mathbf{u}^\perp = (-v, u)^T$. Taking the dot product of (3.1) with the normal vector $\bar{\mathbf{n}} = (n_x, n_y)^T$ and using the zero normal velocity $\mathbf{u} \cdot \bar{\mathbf{n}} = 0$ at the wall, we find the following geostrophic balance condition on the resultant tangential velocity component on a linear piece of the boundary:

$$\mathsf{f}\, \mathbf{u} \cdot \bar{\mathbf{t}} = g\bar{\mathbf{n}} \cdot \nabla(h + h_b). \tag{3.2}$$

When $\mathsf{f} = 0$ we find $\bar{\mathbf{n}} \cdot \nabla(h + h_b) = 0$. The velocity is decomposed as follows

$$\mathbf{u} = (\mathbf{u} \cdot \bar{\mathbf{n}})\, \bar{\mathbf{n}} + (\mathbf{u} \cdot \bar{\mathbf{t}})\, \bar{\mathbf{t}} \tag{3.3}$$

with $\bar{\mathbf{t}} = (-n_y, n_x)$ the tangential vector. For the numerical implementation, we use the ghost value $\mathbf{U}^b$. Rather than using $\mathbf{u} \cdot \bar{\mathbf{n}} = 0$ and $\bar{\mathbf{n}} \cdot \nabla(h + h_b) = 0$ when $\mathsf{f} = 0$, we enforce $\mathbf{u}^b \cdot \bar{\mathbf{n}} = -\mathbf{u}^l \cdot \bar{\mathbf{n}}$ and $\mathbf{u}^b \cdot \bar{\mathbf{t}} = \mathbf{u}^l \cdot \bar{\mathbf{t}}$ to obtain

$$h^b = h^l;\ u^b = (n_y^2 - n_x^2)u^l - 2n_x n_y v^l \text{ and } v^b = (n_x^2 - n_y^2)v^l - 2n_x n_y u^l. \tag{3.4}$$

For $\mathsf{f} \neq 0$, the situation appears ambiguous. We took

$$h^b = h^l;\ (u^b, v^b) = -(u^l, v^l) + (-n_y, n_x)(2g/\mathsf{f})\big(\bar{\mathbf{n}} \cdot \bar{\nabla}(h + h_b)\big). \quad (3.5)$$

such that $\mathbf{u}^b \cdot \bar{\mathbf{n}} = -\mathbf{u}^l \cdot \bar{\mathbf{n}}$ and $\mathbf{u}^b \cdot \bar{\mathbf{t}} = -\mathbf{u}^l \cdot \bar{\mathbf{t}} + 2\,(g/\mathsf{f})\,\bar{\mathbf{n}} \cdot \bar{\nabla}(h + h_b)$.

Moving wall: At a moving wall boundary we impose in space-time

$$\mathbf{U}^b \cdot \mathbf{n} = -\mathbf{U}^l \cdot \mathbf{n}, \quad \mathbf{U}^b \cdot \mathbf{t}_1 = \mathbf{U}^l \cdot \mathbf{t}_1 \quad \text{and} \quad \mathbf{U}^b \cdot \mathbf{t}_2 = \mathbf{U}^l \cdot \mathbf{t}_2, \quad (3.6)$$

where $\mathbf{t}_1$ and $\mathbf{t}_2$ are unit tangential vectors orthogonal to each other and to the normal vector $\mathbf{n}$ such that $\mathbf{t}_1 \times \mathbf{t}_2 = \mathbf{n}$. Solving (3.6) simultaneously and substituting the relation $\mathbf{t}_1 \times \mathbf{t}_2 = \mathbf{n}$, we obtain

$$\begin{aligned} h^b &= (-n_t^2 + n_x^2 + n_y^2)h^l - (2n_t n_x)h^l u^l - (2n_t n_y)h^l v^l, \\ h^b u^b &= (-n_x^2 + n_t^2 + n_y^2)h^l u^l - (2n_t n_x)h^l - (2n_x n_y)h^l v^l, \\ h^b v^b &= (-n_y^2 + n_t^2 + n_x^2)h^l v^l - (2n_t n_y)h^l - (2n_x n_y)h^l u^l. \end{aligned} \quad (3.7)$$

3.3 Verification

In all the numerical experiments, we work with non-dimensionalized shallow water equations as stated in section 2.2. Errors of the numerical results include the $L^2(\Omega_\mathsf{h})$ and $L^\infty(\Omega_\mathsf{h})$ norms

$$\|\mathsf{Error}\|_{L^2(\Omega_\mathsf{h})} := \Big(\sum_K \int_{K_\mathsf{k}^n} (\mathbf{U}_\mathsf{exact} - \mathbf{U}_\mathsf{h})^2 \mathrm{d}K\Big)^{1/2}, \quad (3.8)$$

$$\|\mathsf{Error}\|_{L^\infty(\Omega_\mathsf{h})} := \max_K \Big(\max_{\mathbf{x} \in K_\mathsf{k}^n} \|\mathbf{U}_\mathsf{exact} - \mathbf{U}_\mathsf{h}\|\Big), \quad (3.9)$$

where the maximum $\max\|\cdot\|$ is based on local Gauss integration points within the element K_k^n, and $\mathbf{U}_\mathsf{exact}$ and $\mathbf{U}_\mathsf{h}$ are exact and numerical solutions, respectively. The order of accuracy "order" of the method is obtained as

$$\mathsf{order} = \Big(\ln(\|\mathsf{Error}\|^{(1)}) - \ln(\|\mathsf{Error}\|^{(2)})\Big) / \Big(\ln(\mathsf{h}_\mathcal{K}^{(1)}) - \ln(\mathsf{h}_\mathcal{K}^{(2)})\Big), \quad (3.10)$$

where $\|\mathsf{Error}\|^{(1)}$ and $\|\mathsf{Error}\|^{(2)}$ are the errors computed on the meshes with cell measures $\mathsf{h}_\mathcal{K}^{(1)}$ and $\mathsf{h}_\mathcal{K}^{(2)}$, respectively. While computing the order of accuracy, we have refined the space-time mesh uniformly in both space and time.

3.3.1 Burgers' solution

The one dimensional shallow water equations with $h_b = 0$ take the form of Burgers' equation $\partial_t q + q\partial_x q = 0$, when one of its Riemann invariants is taken constant as $u + 2\sqrt{gh} = c$ with $q(t,x) = c - 3\sqrt{gh}$. A solution can be constructed as $h(t,x) = (q(t,x) - c)^2/(9g)$ and $u(t,x) = (c + 2q(t,x))/3$ from the implicit solution $q(t,x) = q_0(x')$, $x = x' + q_0(x')t$, where $q(0,x) = q_0(x)$ is the initial condition. For an initial condition $q_0(x)$ with $dq_0/dx < 0$ somewhere, wave breaking occurs at time $t_b = -1/\min(dq_0/dx)$.

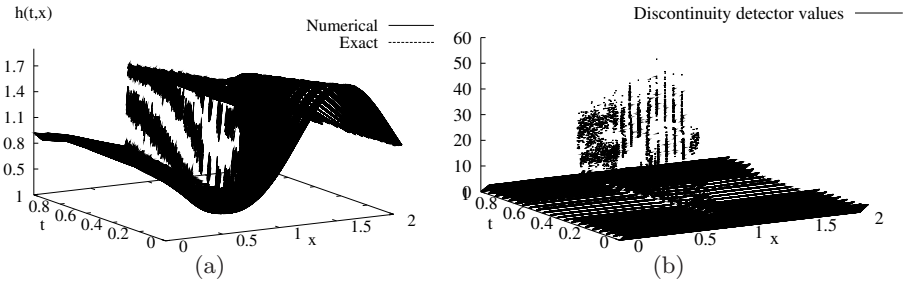

Figure 3.1: (a) Comparison of exact and numerical solutions of water depth $h(t,x)$. (b) Plot of the discontinuity detector. Computations are performed on an irregular grid of 160×160 elements from $t = 0$ to the time of breaking $t_b \approx 0.3$ and $t_b < t < 1$. Irregular grids are made by a slight, random perturbation of the interior grid points of a rectangular mesh.

We chose $c = 3$, $q_0(x) = sin(\pi x)$ with $x \in [0, 2]$ and used periodic boundary conditions in x. The space-time profile of water depth for the exact and numerical solutions are shown in Fig. 3.1(a). The smooth initial condition develops into a discontinuity in a finite time $t < t_b = 1/\pi$ at $x = 1$. We can thus test Krivodonova's discontinuity detector, which shows no sign of discontinuity in the beginning and gradually detects the regions with sharp gradients to finally detect discontinuities as shown in Fig. 3.1(b). Before breaking, we compute several errors for mass, h, and momentum, hu, on various meshes and plot them on a log-log scale in Figs. 3.2(a,b). They indicate that the method is second order accurate in space and time.

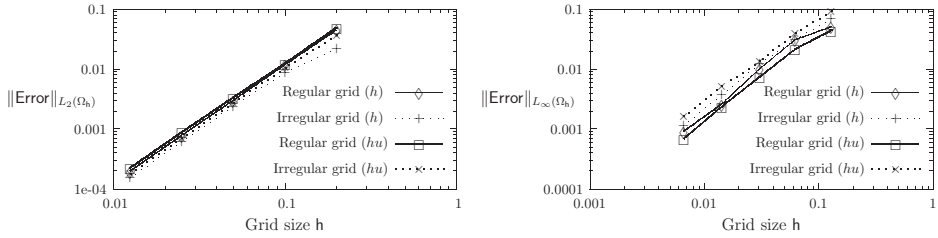

(a) (b)

Figure 3.2: (a) Log-log plot of the $\|\mathsf{Error}\|_{L^2(\Omega_h)}$ versus grid size h at $t = 0.2$. The average slope of the curves is 1.955, 1.7875, 1.83 and 1.795 for h and hu on regular and irregular grids, respectively. (b) Log-log plot of the $\|\mathsf{Error}\|_{L^\infty(\Omega_h)}$ versus grid size h at $t = 0.2$. The average slope of the curves is 1.32, 1.39, 1.16 and 1.39 for h and hu on regular and irregular grids, respectively. Regular grids are tessellated with 10, 20, 40, 80 and 160 elements and irregular grids with 10×10, 20×20, 40×40, 80×80 and 160×160 elements. Computations are performed with time steps $\Delta t = 0.05, 0.025, 0.0125, 0.0625$ and 0.003125 from coarse to fine grids.

3.3.2 Dispersion and dissipation error

To quantitatively verify the Fourier analysis, we consider the following harmonic wave type solution based on (2.67) in a domain $[0, L_x]$ with $h(t, x) = H + A\sin(kx + \omega t)$ and velocity corresponding to the real part of (2.68). In section (4.2), we have presented the discrete Fourier analysis of equations (2.67) to determine the numerical frequency ω_1 and the numerical dissipation ω_2 of a given harmonic wave from (2.77). Here, we initialize with the harmonic wave solution based on (2.67) in the nonlinear numerical code, for small amplitude, and compare our numerical simulations both with the exact solutions and discrete Fourier solutions. The discrete Fourier solutions can be simply given by replacing frequency ω by ω_1 and amplitude A by $A\exp(-\omega_2 t)$. Figs. 3.3(a,b) show the exact and numerical solution at $t = 3.0$ for $\mathsf{f} = 2\pi$, respectively. Observe the phase decay of amplitude of the waves in Fig. 3.3. We conclude that our numerical scheme confirms the Fourier analysis.

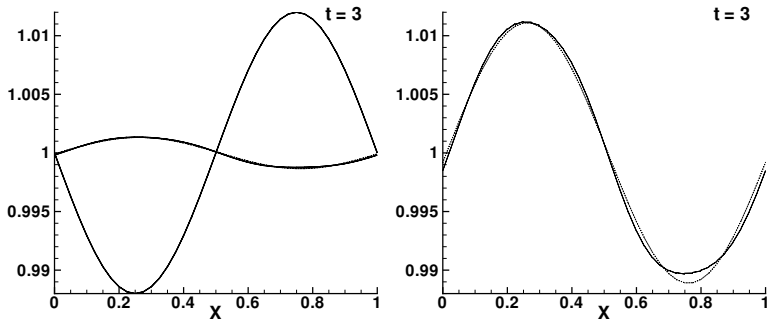

(a) (b)

Figure 3.3: Free surface plots showing a) the dissipation in a comparison of the exact versus exact discrete and numerical solution and b) the dispersion of the exact discrete and numerical solution for $\mathsf{f} = 2\pi$, $k = 2\pi$, $g = 1$ and $H = 1$ with $\omega_1 = 8.3535$ and $\omega_2 = 0.73235$ for $\Delta x = 0.025$ and $\Delta t = 0.25$. We purposely chose a case with strong dissipation for illustrative purposes.

3.3.3 Poincaré and Kelvin waves

Poincaré and Kelvin wave solutions arise when we solve the linearized rotating shallow water equations in rectangular channel and circular basins. We simulate the non-linear counterparts of these harmonic waves at low amplitude for a number of time periods to show the dispersion and dissipation error.

Rectangular channel

Both Poincaré and Kelvin waves [47] are simulated for ten time periods in a rectangular channel periodic in x. Dispersion errors and dissipation errors are observed in the numerical solutions displayed in Figs. 3.4 and 3.5.

Circular basin

We numerically simulate Poincaré and Kelvin waves [35], the former from $t = 0, ..., 10T$ with $T = 2\pi/\omega = 0.7217287851$ in a circular basin. Figs. 3.6 show contour plots of the free surface for Poincaré waves and the difference between the exact linear and numerical nonlinear solutions. Differences are

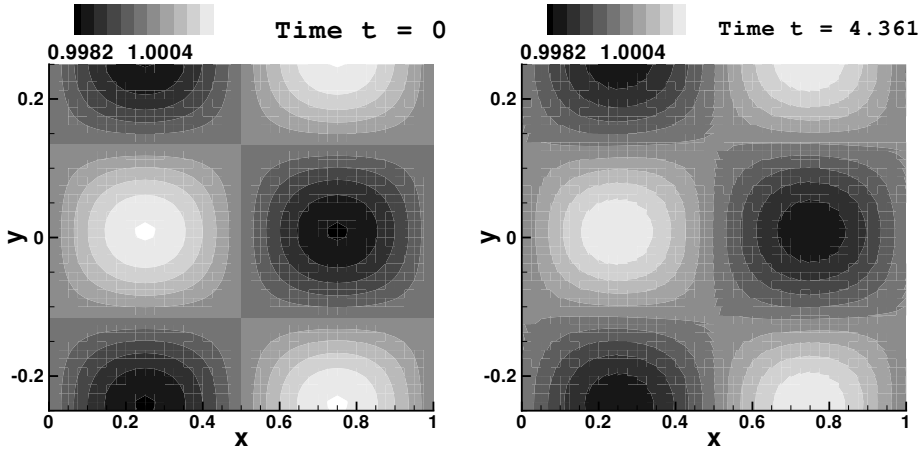

(a) Initial profile.

(b) Final profile.

Figure 3.4: Contour plots of the free surface for Poincaré waves a) at $t = 0.0$ and b) at $t = 10T$. The linear wave amplitude is $A(\omega l \cos(ly) + \mathsf{f}k \sin(ly)) \sin(kx + \omega t)$ with wave numbers k, l, and frequency $\omega = \sqrt{\mathsf{f}^2 + a^2 (k^2 + l^2)}$. The wave amplitude is 10^{-5}, zonal and meridional wave numbers are $m = n = 1$, $g = H = 1$, and $\mathsf{f} = 3.193379349$. Simulated on a mesh of size 80×40 elements with $CFL_{\Delta t} = 1.0$.

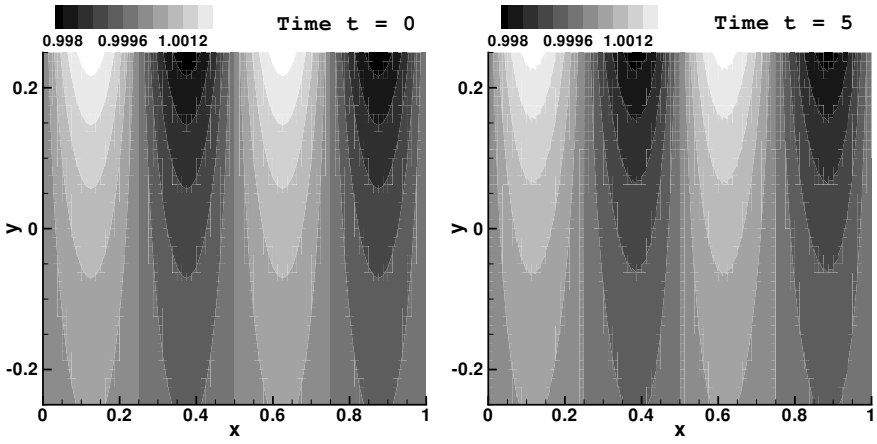

(a) Initial profile. (b) Final profile.

Figure 3.5: Contour plots of the free surface for Kelvin waves a) at $t = 0.0$ and b) at $t = 10T$. Linear wave amplitude is $A(\cosh(ly)+\sinh(ly))\sin(kx+\omega t)$ with wave amplitude $A = 0.001$, $l = \mathsf{f}/a$, $\omega = a\,k$, zonal wave number $m = 2$, $g = H = 1$, and $\mathsf{f} = 3.193379349$. Simulated on a mesh of size 80×40 elements with $CFL_{\Delta t} = 1.0$.

small as expected for small-amplitude waves.

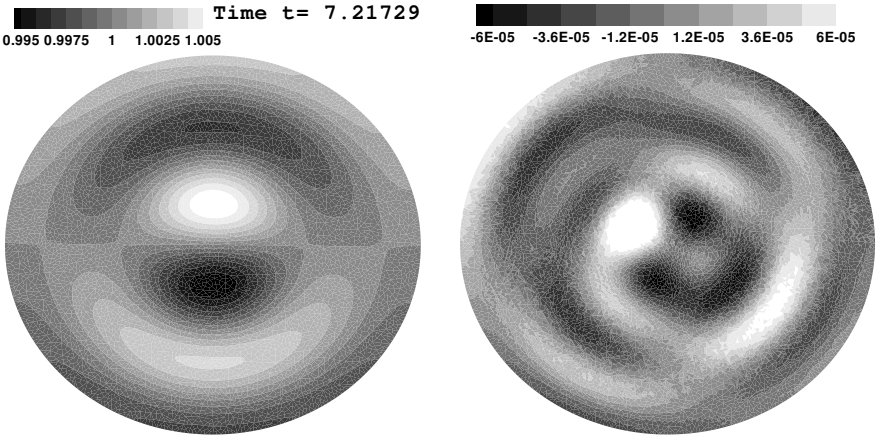

(a) Final profile. (b) Difference.

Figure 3.6: Contour plots of a) free surface of the Poincaré waves, and b) the difference between linear exact and nonlinear numerical solutions after ten time periods. Linear wave amplitude is $AJ_m(kr)\sin(m\theta+\omega t)$ with Bessel function $J_m(kr)$, radius r, azimuth θ, domain radius $R=1$, azimuthal wave number $m=1$, $\mathsf{f}=1.596689674$, $A=0.01$, $H=1$, $R=1$, $g=1$, radial wave number $k=8.558068886$ obtained from the boundary condition, and $\omega=8.705742988$.

The Kelvin wave mode has a time period $T=2\pi/\omega=7.356451577$ and we numerically simulate these waves from $t=0,...,5T$ (see Figs. 3.7).

3.3.4 Moving grid simulations

Harmonic wave maker

Consider the linearized shallow water equations $\partial_t\eta + H\,\bar{\nabla}\cdot\mathbf{u}=0$ and $\partial_t\mathbf{u}+g\bar{\nabla}\eta=0$ in a rectangular basin of size $[(0,L_x)\times(0,L_y)]$ with a solid wave maker at the boundary $x_E(t,y)=L_x+x_m(t,y)$, fixed solid walls on the remaining boundaries, free surface perturbation $\eta(\mathbf{x})$ around a mean surface H, and velocity field $(u(\mathbf{x}),v(\mathbf{x}))$. After applying the kinematic boundary condition at the wave maker and linearizing the resulting expression, we

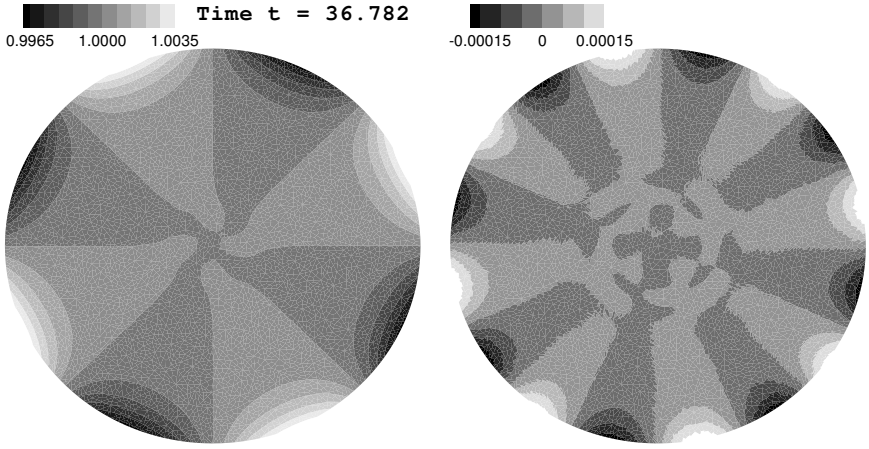

(a) Final profile. (b) Difference.

Figure 3.7: Contour plots of a) free surface of the Kelvin waves, and b) difference between linear exact and nonlinear numerical solutions at $t = 5\,T$. Linear wave amplitude is $AI_m(kr)\sin(m\theta + \omega t)$ with modified Bessel function $I_m(kr)$, $m = 4$, $\mathsf{f} = 1.596689674$, $A = 10^{-5}$, $R = 5$, $g = H = 1$, $k = 1.349044778$ and $\omega = -0.8541054396$.

obtain $\partial_t x_m = u(t, x = L_x, y)$. A linear gravity-wave type solution follows as

$$\begin{aligned}(\eta(\mathbf{x}), x_m(t,y)) &= \eta_0 \left(\cos(kx), -g\,k\sin(kL_x)/\omega^2\right)\cos(ly)\sin(\omega t),\\ (u(\mathbf{x}), v(\mathbf{x})) &= -g\,k\eta_0(k,l)\sin(kx)\cos(ly)\cos(\omega t)/\omega,\end{aligned} \tag{3.11}$$

where η_0 is the amplitude of the harmonic free surface waves, ω the frequency determined from the dispersion relation $\omega^2 = g\,H\,(k^2 + l^2)$ once $l = n\pi/L_y$ the wave numbers along y and $k = m\pi/L_x$ along x are known, with n an integer and m a real number.

We initialize the nonlinear equations using the gravity wave solution (3.11) at $t = 0$, and prescribe the movement of the wave maker at $x = L_x$ to simulate the waves induced. To maintain elements of regular size, we move the nodes of the grid by linearly interpolating between the wave maker and the solid wall at $x = 0$. Thus, given the coordinates of a node at time t_{n-1}, it is straightforward to determine these at time t_n. We simulate the nonlinear waves generated by the harmonic wave maker for low and high amplitudes. At low amplitude, we see that harmonic waves in the wave maker agrees qualitatively with the solution (3.11), see Figs. 3.8 and at high amplitudes, these harmonic waves start to break due to non-linearity and moving bores are formed, see Figs. 3.9. For low amplitude the energy stays essentially constant, while for high amplitude the energy fluctuates but initially decreases on average due to wave breaking, see Figs. 3.10.

3.4 Validation

In this section, we validate numerical simulations of bore-vortex interactions against the qualitative analytical predictions of PV anomaly from the expression (2.10). In each of the three cases presented, there is initially no PV, but PV is generated through the passage of a non-uniform bore. We verified the simulations against Tassi *et al.*'s [57] who used a space DG method.

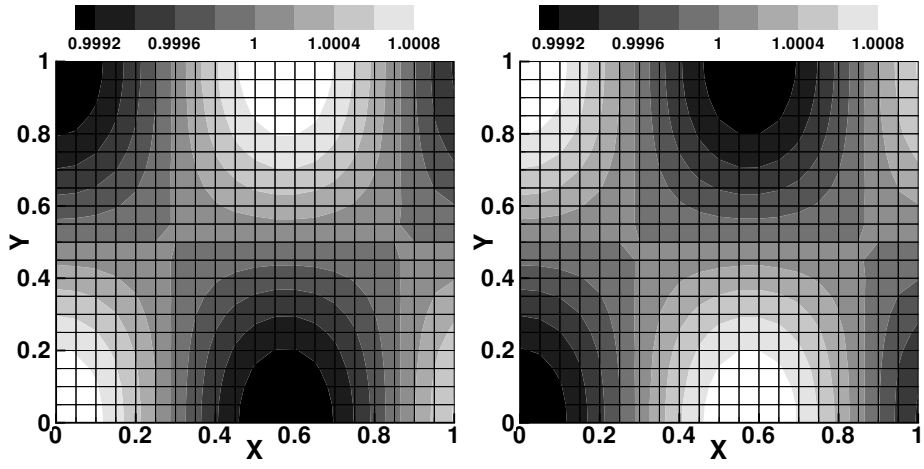

(a) At t = T/4. (b) At t = 3T/4.

Figure 3.8: Contour plots of water depth h for a time period $T = 2\pi/\omega = 1.0$. Parameters $g = 1$, $H = 1$, $\eta_0 = 0.001$, $n = 1$ and $m = \sqrt{3}$ such that $\omega = 2\pi$. At $t = T/2$ and T, the free surface is nearly flat.

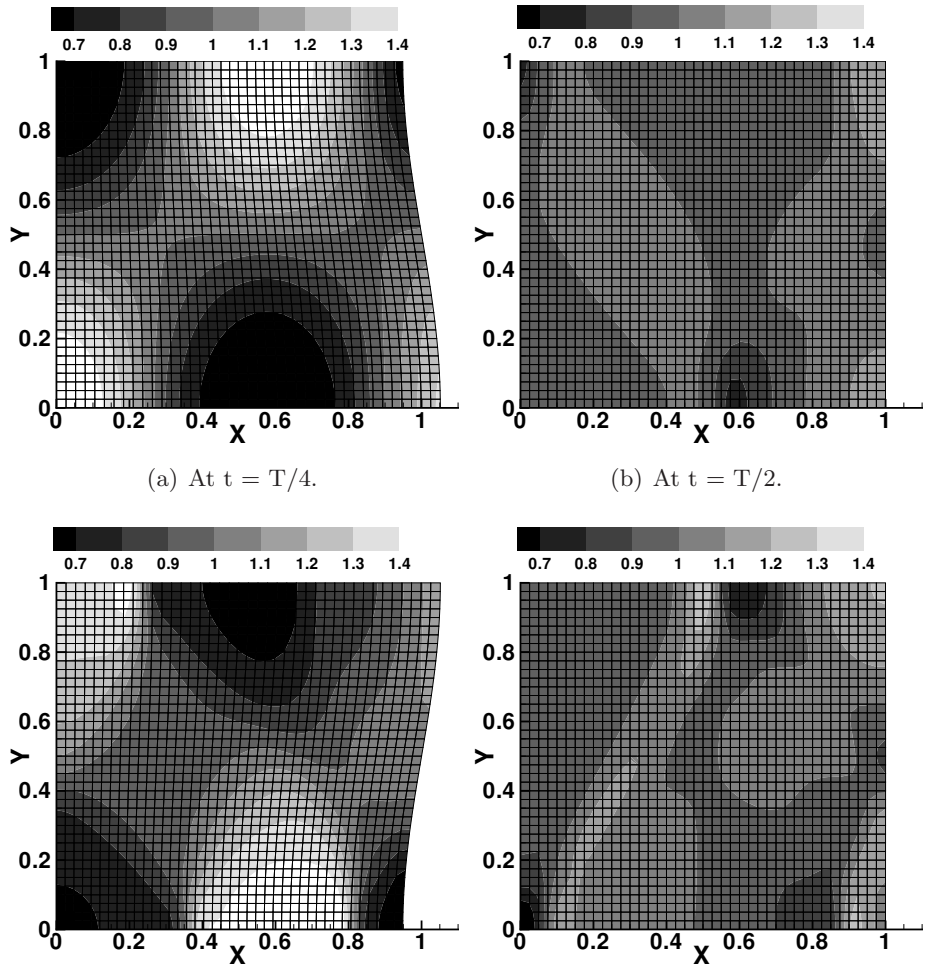

(a) At t = T/4.

(b) At t = T/2.

(c) At t = 3T/4.

(d) At t = T.

Figure 3.9: Contour plots of water depth h for a time period $T = 2\pi/\omega = 1.0$. Parameters $g = 1$, $H = 1$, $\eta_0 = 0.5$, $n = 1$ and $m = \sqrt{3}$ such that $\omega = 2\pi$.

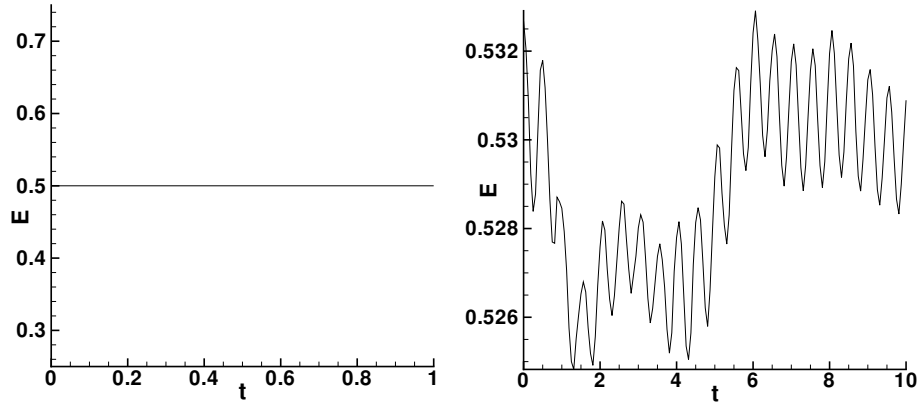

(a) Low amplitude (b) High amplitude

Figure 3.10: Plots of the energy as a function of time in the wave maker test.

3.4.1 Non-linear breaking shallow water waves

We consider the linear gravity wave solution

$$\begin{aligned} \eta(\mathbf{x}) &= A\sin(ly)\sin(kx+\omega t), \\ (u(\mathbf{x}),v(\mathbf{x}))^T &= Ag\left(-k\sin(ly)\sin(kx+\omega t), l\cos(ly)\cos(kx+\omega t)\right)^T/\omega \end{aligned} \tag{3.12}$$

in a rectangular domain of size $[L_x, L_y]$ periodic in x with solid walls along y, $k = 2\pi m/L_x$, $l = (2n+1)\pi/L_y$, and $\omega^2 = gH(k^2+l^2)$. The nonlinear numerical discretization is initialized with this linear solution (3.12) at $t = 0.0$ with $A = 0.01$, $g = H = 1$, $m = 2$ and $n = 0$.

Due to non-linearity, these higher amplitude gravity waves start to break around $t \approx 0.5$, which can be confirmed from the energy-time graph shown in Fig. 3.12(a). The breaking of the waves is first seen at the peak of crests and troughs of the free surface near to the walls, see Fig. 3.11(a) and (b). As seen in Fig. 3.13(a), the breaking extends to the interior and moving bores are formed which are aligned in the y–direction with some curvature. Since the non-uniform depth profile of the bore appears to be preserved in

time, we estimate its upstream and downstream depths from (3.12) as

$$h_1(\hat{y}) = H - \eta_D(\hat{y}) \quad \text{and} \quad h_2(\hat{y}) = H + \eta_D(\hat{y}), \tag{3.13}$$

respectively, with $\eta_D(\hat{y}) = |\hat{A}|\sin(\pi\hat{y})$, $\hat{A}$ the amplitude and $\hat{y}$ the axis aligned along the bore neglecting the curvature of the bore. These bores are traveling in the negative x–direction with their axis $\hat{y}$ roughly parallel to the direction of y–axis. Substituting the depths (3.13) in (2.10), we get the PV generation behind the bore as

$$\Delta\Pi = \Pi_1 - \Pi_2 = \frac{2g\eta_D^2(3H^2 - \eta_D^2)}{(H^2 - \eta_D^2)^2}\Big(\frac{-1}{Q}\frac{d\eta_D}{d\hat{y}}\Big). \tag{3.14}$$

For $-0.5 < y < 0$, we have $d\eta_D/d\hat{y} > 0$, $h_1 > h_2$, $Q < 0$ and $\Delta\Pi > 0$; and for $0 > y > 0.5$, we have $d\eta_D/d\hat{y} > 0$, $h_1 < h_2$, $Q > 0$ and $\Delta\Pi < 0$. Hence, the PV generated in Fig. 3.13(b) has a positive sign on the positive y axis and vice versa. Also see the zonal average of PV along the grid lines parallel to x–axis in Fig. 3.12(b). This qualitatively validates the bore-vortex anomaly discussed in section 2.2.

The bores formed are simulated till $t = 25$ when they have dissipated their energy as seen in Fig. 3.12(a). As a result, we see a PV jet formation near to the walls, shown in Fig. 3.13(d) to 3.13(f). Due to energy dissipation, the strength of the bores gradually decreases as in Fig. 3.13(a) to 3.14(a), and finally the bores disappear in Fig. 3.14(c) to 3.14(e). Although the bores disappear, the jet remains since PV is materially conserved (see Figs. 3.14(d) to 3.14(f)).

3.4.2 Bore propagation over a mound

Conical shaped mound

Matsutomi and Mochizula [40] conducted experiments to study the behavior of a bore propagating over a conical shoal and Hu [25] conducted numerical simulations of these experiments. We show similarly that the correct PV anomaly is generated in our numerical simulation due to non-uniform energy dissipation along the bore.

Consider the dam-break initial condition $h(0,\bar{\mathbf{x}})+h_b(\bar{\mathbf{x}}) = h_L$ for $x < x_c$, $h(0,\bar{\mathbf{x}})+h_b(\bar{\mathbf{x}}) = h_R$ for $x > x_c$ and water at rest $\mathbf{u}(0,\bar{\mathbf{x}}) = 0$, where $x = x_c$

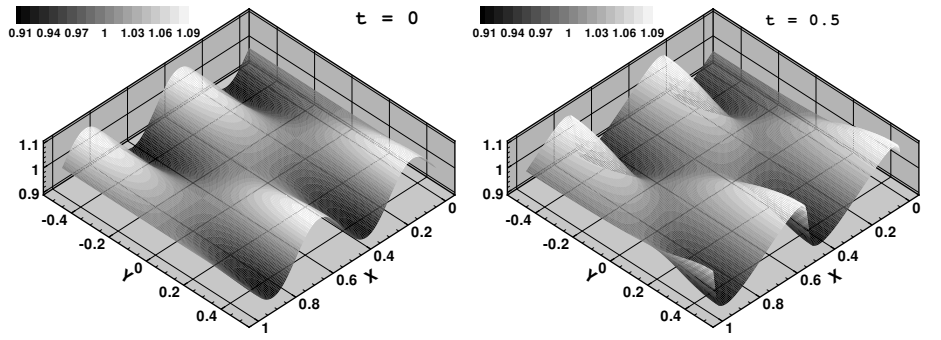

(a) (b)

Figure 3.11: Free surface height of the water at a) t = 0.0 and b) t= 0.5.

is the discontinuity in a rectangular channel of size $[0, L_x] \times [0, L_y]$. Let an isolated conical shaped mound be situated with its center at $\bar{\mathbf{x}}_m = (x_m, L_y/2)$, radius R_m, height H_m. The bottom topography in the channel is

$$h_b(\mathbf{x}) = \begin{cases} H_m - \dfrac{H_m}{R_m}|\bar{\mathbf{x}} - \bar{\mathbf{x}}_m|, & \text{if } |\bar{\mathbf{x}} - \bar{\mathbf{x}}_m| \le R_m \text{ and} \\ 0.0, & \text{if } |\bar{\mathbf{x}} - \bar{\mathbf{x}}_m| > R_m. \end{cases} \tag{3.15}$$

The boundaries of the domain consist of solid walls except for an open boundary at $x = L_x$.

When the dam collapses, a bore with uniform jump is generated which propagates towards and over the conical hump, see Fig. 3.15, and dissipates energy uniformly along its length. When the bore reaches the conical hump energy dissipation becomes non-uniform and the approximate PV generation (2.10) across the bore is

$$\Pi_1 - \Pi_2 \approx \frac{E_D}{Q}\left(\frac{1}{h_1} + \frac{1}{h_2}\right)(-\partial_y h_b), \tag{3.16}$$

with $h_1 \approx h_L - h_b$ and $h_2 \approx h_R - h_b$, since we always observe a nearly uniform jump in the free surface along the bore in our numerical simulations and $\hat{y}$ is aligned with y. For $y > L_y/2$, we have $-\partial_y h_b > 0$ and vice versa for $y < L_y/2$. Hence, a positive PV anomaly arises for $y > L_y/2$ and a

negative one for $y < L_y/2$ after the bore has passed. This is confirmed in the contour plots of PV shown in Fig. 3.16: a positive vortex and PV are found for $y > L/2$ and vice versa for $y < L/2$ after the bore's passage. Thereafter, these PV anomalies are advected along, cf. (2.5).

Gaussian shaped mound

In this test case, we also consider an initial dam break as $h(0, \bar{\mathbf{x}}) + h_b(\bar{\mathbf{x}}) = h_L$ for $x < x_c$, $h(0, \bar{\mathbf{x}}) + h_b(\bar{\mathbf{x}}) = h_R$ for $x > x_c$ and water at rest $\mathbf{u}(0, \bar{\mathbf{x}}) = 0$. The discontinuity in the free surface lies thus at $x = x_c$ in a rectangular channel of size $[0, L_x] \times [0, L_y]$. It has solid wall boundaries except for an open flow boundary at $x = L_x$. The bottom topography consists of an isolated Gaussian shaped mound with a peak at $\bar{\mathbf{x}}_m = (L_x/2, L_y/2)$:

$$h_b(\mathbf{x}) = H_m \exp(-c_m |\bar{\mathbf{x}} - \bar{\mathbf{x}}_m|^2), \tag{3.17}$$

where H_m is the height of the Gaussian mound and c_m a constant.

When the initial dam collapses, a bore with a uniform jump is generated which propagates towards the Gaussian mound, see Fig. 3.17. As the bore reaches the Gaussian mound, we deduce from (3.16) that the potential vorticity generated behind the bore must have positive sign for $y > L_y/2$ as $\partial_y h_b < 0$ and negative sign for $y < L_y/2$ as $\partial_y h_b > 0$. Hence, the PV generated and seen in Fig. (b) and (c) agrees with the observed one. Once the bore crosses the peak of the hump, a hydraulic jump facing backwards is formed which can be seen as a depression in Fig. 3.17. Thus, it can likewise be deduced that PV anomalies are generated at the hydraulic jump with opposite signs to the initial PV generated at the bore, which is confirmed in Fig. 3.18(d).

3.5 Experimental validation

3.5.1 Flow through a contraction

Shallow water flows through a contraction can under certain flow rates and Froude numbers develop steady oblique hydraulic jumps. Akers [1] conducted laboratory experiments under different flow rates and Froude numbers, and compared them with steady state solutions. His experimental setup consisted of a narrow flume of length $L = 110$ cm. The width of the

flume starts decreasing linearly at $L_0 \approx 79.5$ cm from $b_0 = 20$ cm at the beginning of the contraction or inlet to $b_c = 12$ or 14 cm at the end of the flume or outlet. The steady state state shown in Fig. 3.5.1(a) is reached experimentally with a constant inflow of water with depth h_0 and velocity u_0 such that the Froude number $F_0 = u_0/\sqrt{gh_0} = 3.65$ at the inlet and $b_c = 14$ cm. From the shock relations [55] for the shallow water system (2.1), neglecting friction, the jump ratio and angle of the hydraulic jump can be calculated as steady state solutions following [55]. We find (Al-Tarazi et al. [66]) that

$$\frac{h_1}{h_{0*}} = \frac{\tan\theta_s}{\tan(\theta_s - \theta_c)} \quad \text{and} \quad \sin\theta_s = \sqrt{\frac{1}{2F_{0*}^2}\frac{h_1}{h_{0*}}\Big(1 + \frac{h_1}{h_{0*}}\Big)}, \tag{3.18}$$

where F_{0*} is the uniform upstream Froude number, h_{0*} and h_1 are the upstream and downstream depths of the oblique jump, and θ_c and θ_s are the angle of the contraction and the jump measured relative to the horizontal wall of the flume. The two relations in (3.18) can be combined such that given the uniform upstream conditions u_{0*}, h_{0*}, F_{0*} and the angle θ_c of the contraction, we can entirely determine the conditions u_1, v_1, h_1, θ_s downstream of the oblique jumps. In experiments, due to friction, the Froude number will decrease in the downstream direction, so we use the Froude number and water depth just before the jump as F_{0*} and h_{0*} in (3.18) to obtain an approximate solution. For increasing Froude numbers, the shocks cross within the contraction, the shallow water analogy of a Mach stem appears, and for even higher Froude numbers an upstream moving bore forms.

For theoretical and numerical calculations, the shallow water equations are non-dimensionalized as follows:

$$h' = \frac{h}{b_0},\ (u', v') = \frac{(u, v)}{u_0},\ (x', y') = \frac{(x, y)}{b_0},\ t' = \frac{t}{T}, \quad \text{and } C_D' = \frac{C_D b_0}{h_0} \tag{3.19}$$

with $T = b_0/u_0$. After using (3.19) and dropping the primes, the shallow water equations effectively become (2.1) with $g = 1/F_0^2$. We used a zero velocity and constant depth H as the initial conditions and inflow, outflow and solid wall boundary conditions. The simulation was run to steady state. To mimic the experimental initial condition $H = 0$, we take $H \ll h_0$ due

to which negative depths can occur numerically. The negative depths are corrected by setting the slopes of the approximated depth to zero. After some time, the effect of this correction vanishes and we achieve the steady oblique hydraulic jumps in our simulations as shown in the Fig. 3.5.1(b) with the jump angle similar to the experimental results. Since for the experiment in Fig. 3.5.1(a) the jump ratio is not given, we use the experimental result in which the jump ratio $h_1/h_0 = 1.76$ and the jump angle $\theta_s = 25.2°$ are measured by Akers [1] with the width of the contraction $b_c = 12$ cm and the Froude number at the inlet $F_0 = 3.65$. For this experimental case, we obtain $h_1/h_0 = 1.623 \pm 0.003$ and $\theta_s = 25.50 \pm 0.40°$, numerically with an optimized choice of $C_D = 0.0012$; and $h_1/h_0 = 1.624 \pm 0.004$ and $\theta_s = 25.41° \pm 0.13°$ using the analytical solution (3.18) with the Froude numbers in the contraction.

3.6 Concluding remarks

We have thoroughly verified the present method by testing the order of accuracy and the application of the discontinuity detector in combination with the dissipation operator. The method was second-order accurate in space in both L^2 and L^∞ norms for a linear polynomial approximation of flow fields. We simulated small-amplitude gravity, Kelvin and Poincaré wave solutions for a number of time periods to observe only small dispersion and dissipation errors. Of special importance was the validation of the numerical discretization by simulating bore-vortex interactions, which could be compared with analytical results on the generation of PV anomaly by non-uniform bores. The relevance of these bore-vortex interactions in testing numerical schemes has been promoted in work by Hu [25] (report) and Peregrine [48]. Three demanding cases were considered in section 3.4: PV and shear formation by breaking waves in a periodic channel, and the generation of PV and vortices by an initially uniform bore over non-uniform topography. We also successfully validated the numerical shallow water code against laboratory data (Akers [1]) of oblique hydraulic jumps or "shocks" for hydraulic shallow flow through a contraction. Finally, the versatility of the present method in dynamic domains has been demonstrated numerically in section 3.3.4. We considered the generation of nearly linear and highly nonlinear waves by prescribing the motion of a flexible domain wall

as a wave maker. It showed that the space-time DG method seems well suited for improved simulation of run-up and backwash on beaches ([11]) and in flood prediction.

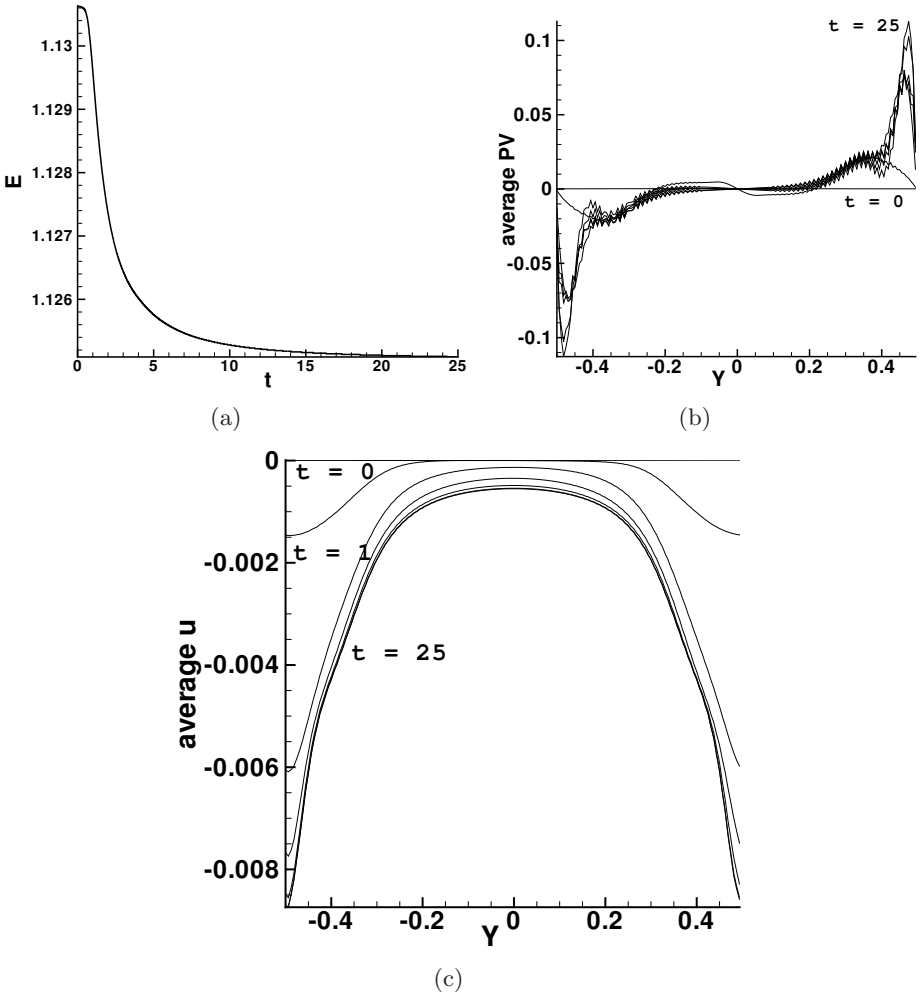

(a) (b)

(c)

Figure 3.12: Shown are a) the energy $E = E(t) = \int_\Omega \tilde{E}(\mathbf{x}, t)\,\mathrm{d}x\,\mathrm{d}y$ (cf. 2.4) as function of time, b) profiles of PV averaged along the channel as a function of y, c) profiles of u averaged as a function of y at various times.

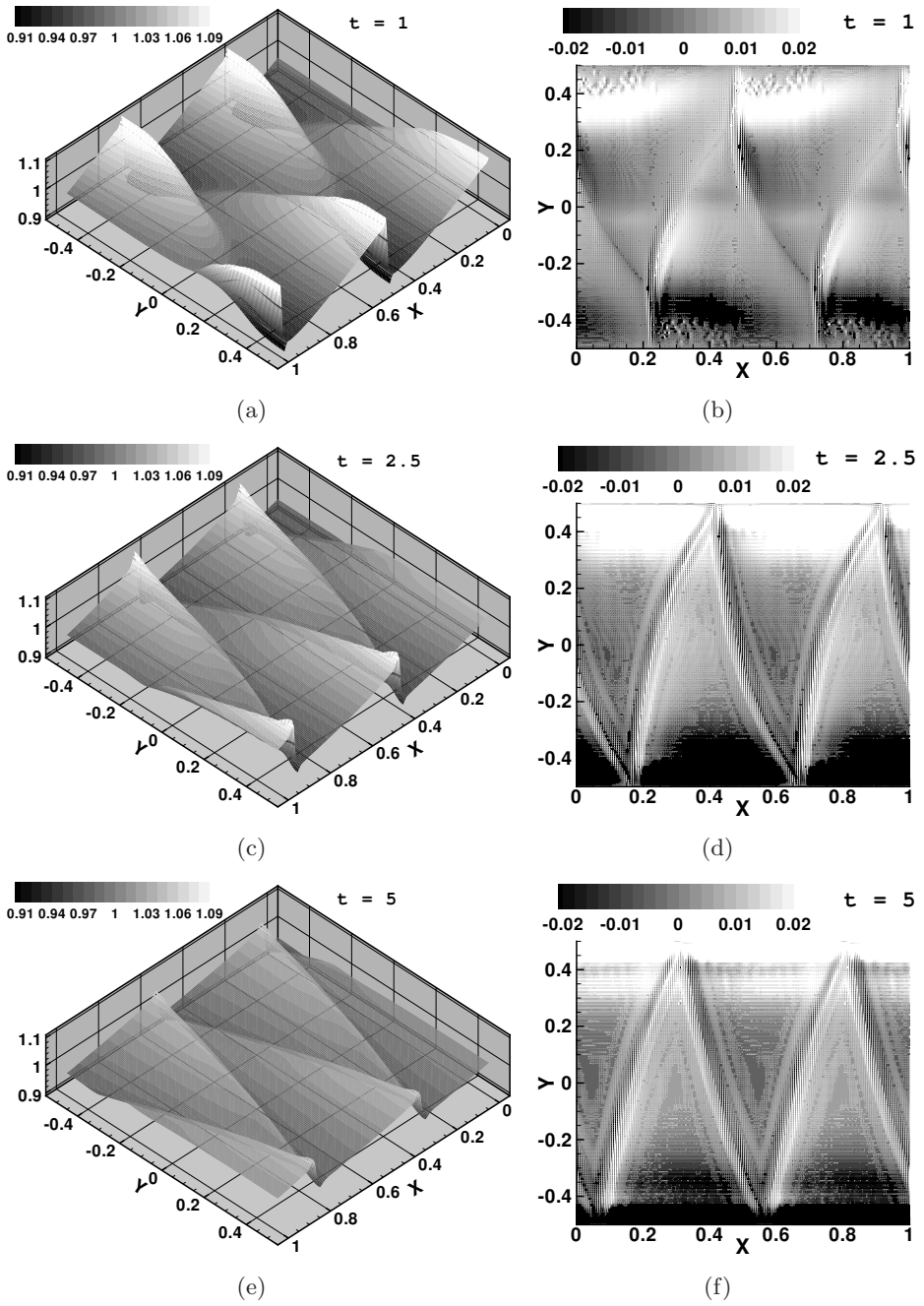

Figure 3.13: a) Free surface height of the water and b) shadow graph of the PV generated at t = 1.0. Observe the PV generation has opposite signs. c,d) Same at $t = 2.5$. e,f) Same at $t = 5.0$.

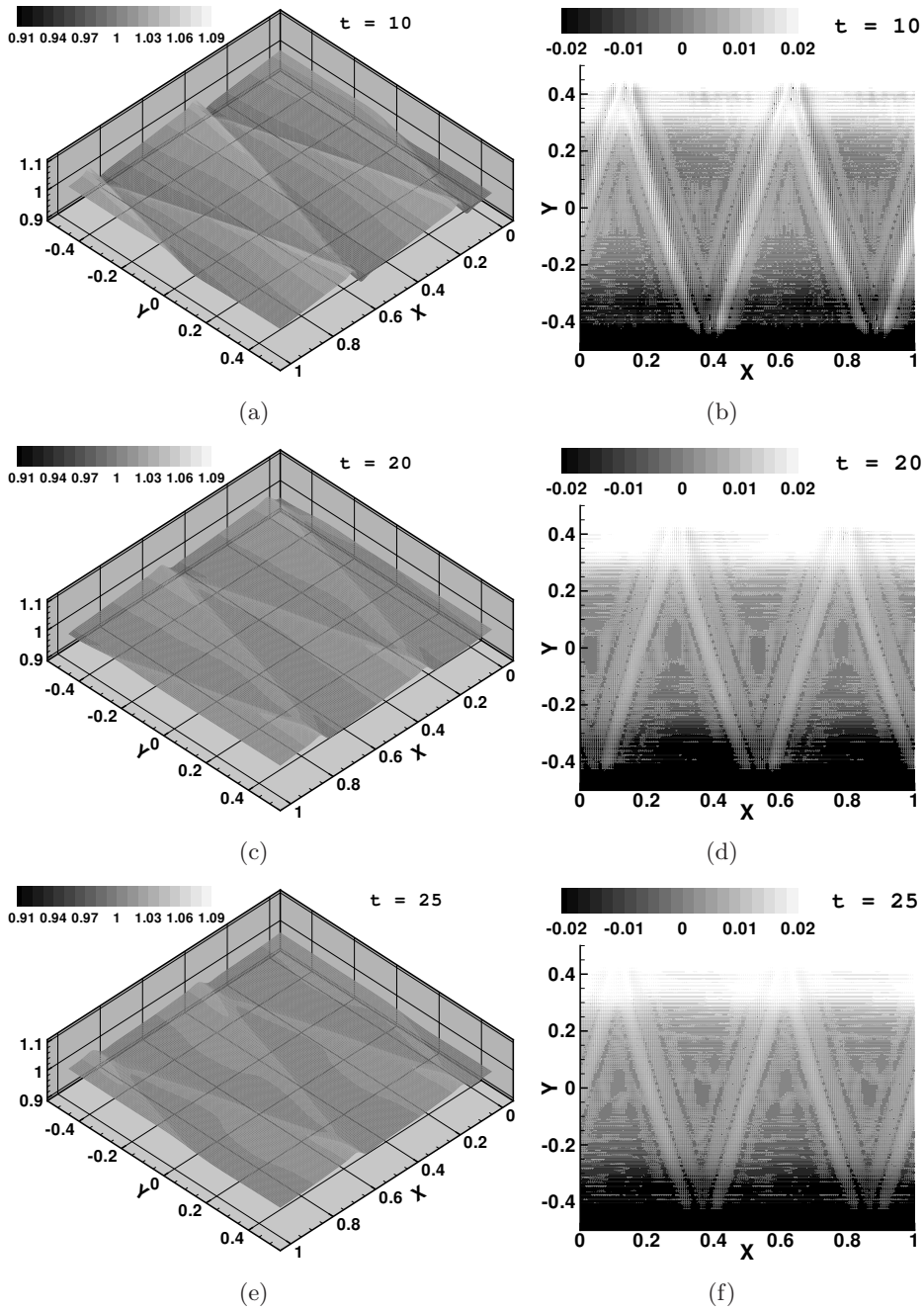

Figure 3.14: a) Free surface height of the water and b) shadow graph of the PV generated at t = 10. c,d) Same at $t = 20$. e,f) Same at $t = 25$.

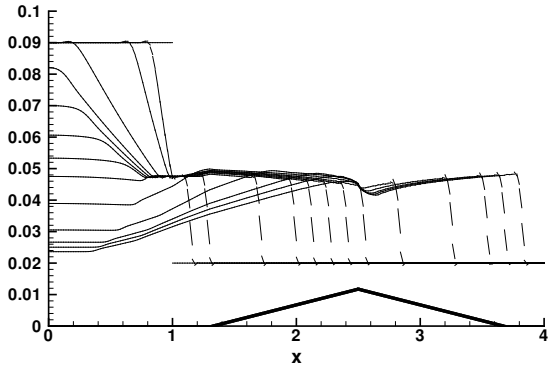

Figure 3.15: A bore propagates over a conical mound: profiles of the free surface $h + h_b$ are shown at $y = 1.3$ from time $t = 0$ to 10 with steps of 0.5. Topography h_b is also displayed.

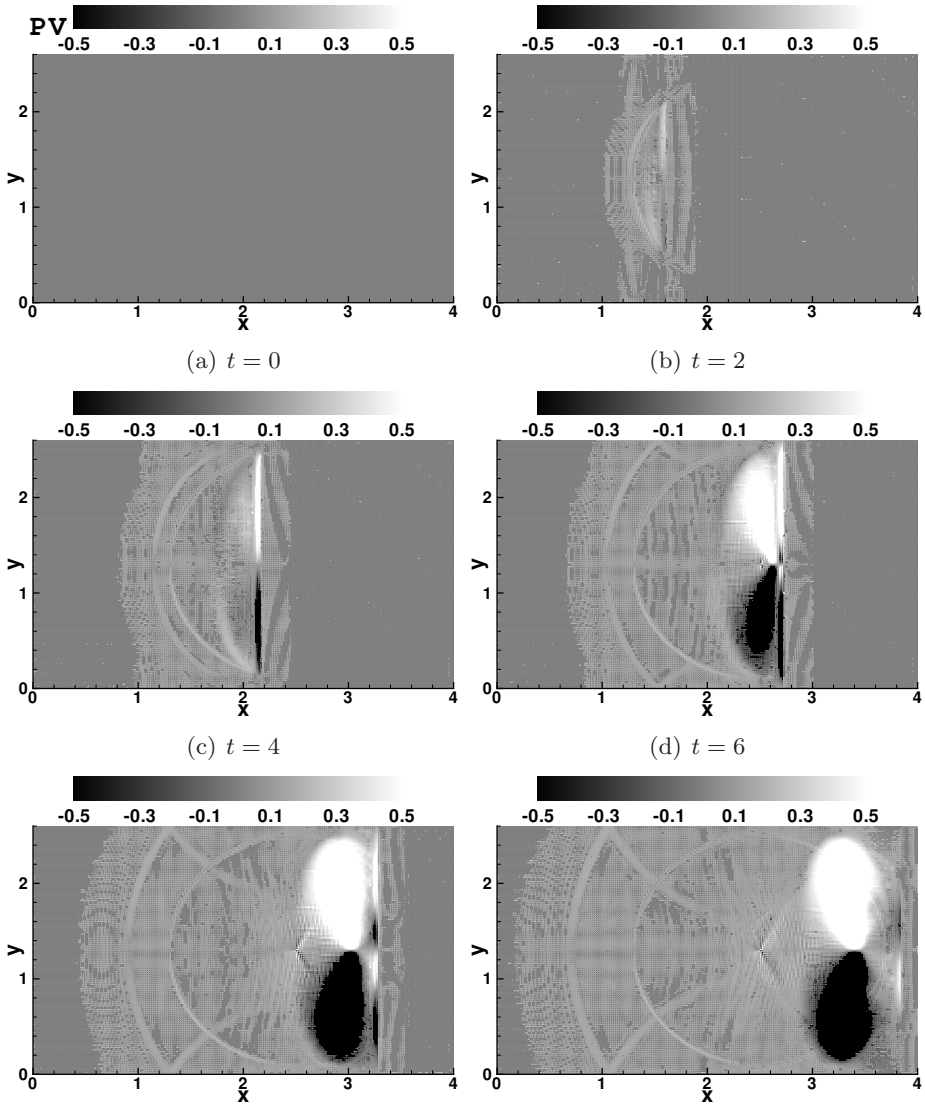

(a) $t = 0$ (b) $t = 2$

(c) $t = 4$ (d) $t = 6$

(e) $t = 8$ (f) $t = 10$

Figure 3.16: Conical mound case. Shown are contour plots of the PV at times $t = 0, 2, 4, 6, 8$, and 10. Note that PV is zero at $t = 0$. Computations are performed on a grid of size $200\times$ 130. Parameters are $L_x = 4.0$, $L_y = 2.6$, $x_m = 2.5$, $R_m = 1.2$ and $H_m = 0.012$.

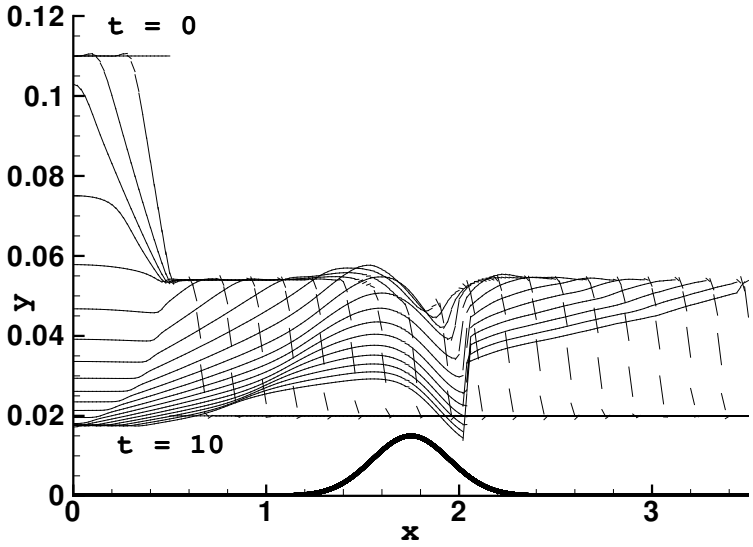

Figure 3.17: A bore propagates over a Gaussian mound: free surface profiles are shown at $y = 1.75$ from time $t = 0$ to 10.

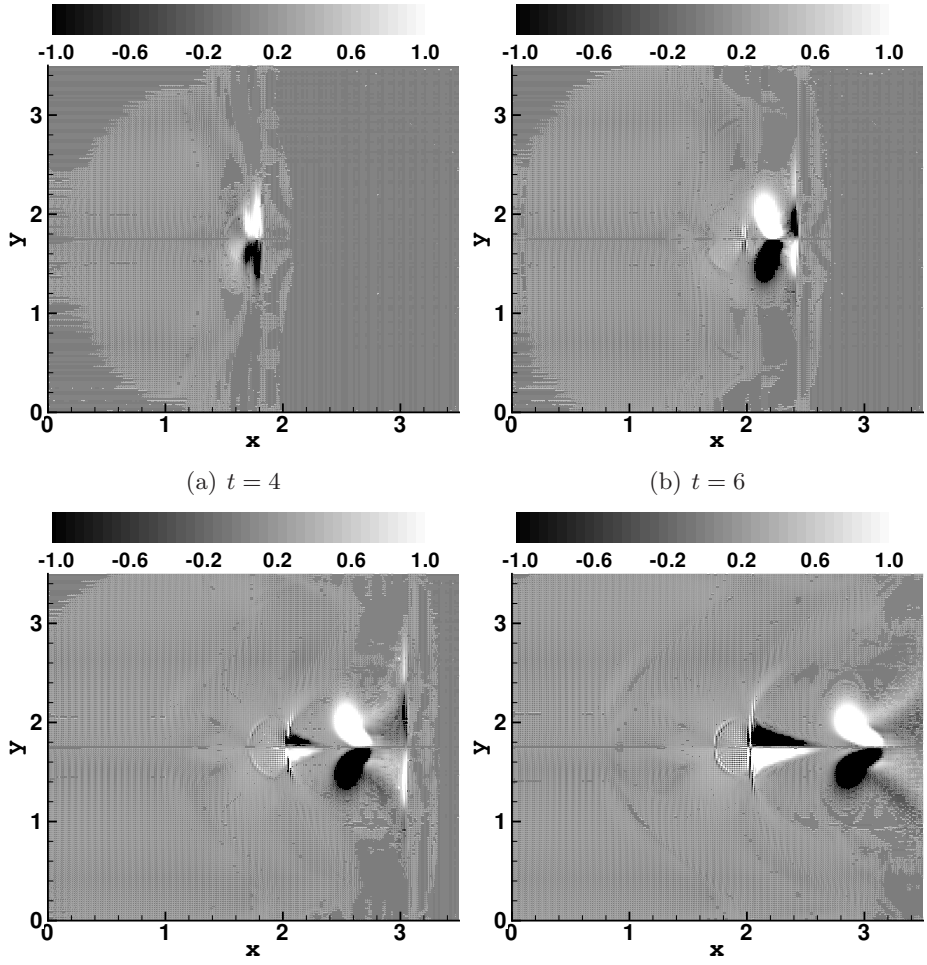

(a) $t = 4$ (b) $t = 6$

(c) $t = 8$ (d) $t = 10$

Figure 3.18: Gaussian mound case. Displayed are contour plots of PV at various times. Note that initially PV is zero. Computations are performed on a grid of size 175×175. We chose $L_x = L_y = 3.5$, $x_c = 0.5$, $h_L = 0.11$, $h_R = 0.02$, $H_m = 0.01$ and $c_m = 12.5$.

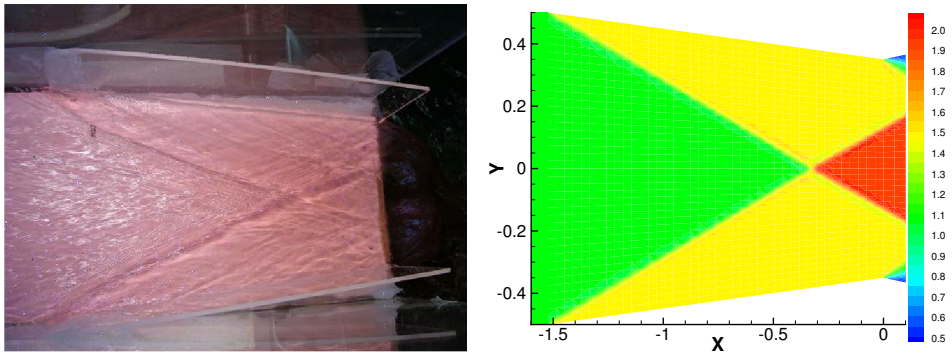

(a) (b)

Figure 3.19: a) Experimental: Steady oblique hydraulic jumps formed in the contraction with $b_c = 14$ cm and the Froude number at the inlet $F_0 = 3.65$. Measured jump angle $\theta_s = 23.61°$. b) Numerical: Steady oblique jumps formed in the contraction with friction coefficient $C_D = 0.00012$. Observed are the jump ratio $h_1/h_0 = 1.471 \pm 0.003$ and the jump angle $\theta_s = 23.27° \pm 0.34°$. Theoretical calculations show a jump ratio $h_1/h_0 = 1.49 \pm 0.003$ and a jump angle $\theta_s = 23.65° \pm 0.09°$. The computational domain is non-dimensionalized with the flume width $b_0 = 20$ cm and tessellated with 40×40 elements in the inlet section, 40×40 elements in the contraction section and 40×20 elements in the outlet section. We provide an outlet section of length 20 cm with a linearly increasing width from b_c to b_0 to achieve the critical condition at the exit of the contraction.

Chapter 4

Variational Space-time (Dis)continuous Galerkin Method for Linear Free Surface Waves

4.1 Introduction

A large class of water wave problems is captured by a model that consists of a potential flow equation coupled with nonlinear free surface boundary conditions. These equations are obtained from the Euler equations of fluid motion with the assumptions that the fluid is inviscid and incompressible, and the velocity field irrotational (see Johnson [27]). This model proves useful in studying many marine and offshore engineering problems such as the wave induced motion of ships and the control of wave generation by wave makers in laboratory basins.

The free surface gravity water wave equations are obtained in a succinct way via Luke's variational principle [39]. The essence of the variational principle is that the complete problem can be expressed in a single functional. In addition, the variational formulation is associated with the conservation of energy and phase space, under suitable boundary conditions. Variational

formulations also provide a basis for the construction of approximate finite element solutions. Such variational finite element methods for free surface waves can be found in Bai and Kim [8], Kim and Bai [28] and Kim et al. [29]. Klopman et al. [32] derive a variational Boussinesq model from Luke's variational principle; in essence their Boussinesq model is a vertical discretization thereof. It motivated us to investigate a (dis)continuous Galerkin finite element method based on a discretization of Luke's variational principle. Such a discretization aims to preserve the variational structure and the associated energy and phase-space conservation.

Standard finite element element methods for free surface gravity water waves are relatively new and can be found in [18, 41, 42, 43, 68, 70, 71]. Another widely used numerical method for free surface waves is the boundary integral method which started with the work of Longuet-Higgins and Cokelet [38], and Vinje and Brevig [67]. This method has been applied extensively to two dimensional free surface waves, see the surveys of Romate [51] and Tsai and Yue [62]. Applications in three dimensions (3D) using boundary integral methods include [16, 51, 10]. The discontinuous Galerkin (DG) methods for elliptic problems proposed by Arnold et al. [5] and Brezzi [15] have enabled researchers to model free surface water waves using a space discontinuous Galerkin method. The space DG finite element method for free surface wave problems can be found in van der Vegt and Tomar [63] and Tomar and van der Vegt [59]. Van der Vegt and Xu [65] have subsequently proposed the space-time DG method for three dimensional nonlinear free surface waves. However, DG methods for free surface waves based on its variational formulation appear to be non-existent.

Nonlinear free surface gravity water wave equations are difficult to solve because the solution to the governing equations depends on the position of the free surface which is not known apriori. To deal with such difficulties, we choose a space-time approach which is particularly suited for problems with time dependent boundaries (see van der Vegt and van der Ven [64], Ambati and Bokhove [4], van der Vegt and Xu [65]).

DG methods have several advantages, as follows:

(i) the scheme is local in the sense that the solution in each element only depends on its neighboring elements via the flux through element boundaries and is thus suitable for parallelization;

(ii) the scheme is extendable to have hp–adaptivity in which the fluid

flow field approximation can arbitrarily vary per element, known as"p–adaptivity", and the mesh can be locally refined, called "h–adaptivity".

Developing a space-time DG finite element scheme faces additional difficulties because

(i) it is nontrivial to develop an efficient solution technique for the nonlinear algebraic equations resulting from the discretization,

(ii) it is complicated to handle the grid deformation due to the nonlinear free surface evolution.

We therefore first consider the development of a variational space-time (dis)continuous Galerkin finite element method (DGFEM) for linear free surface gravity water waves based on Luke's variational principle.

In a variational space-time (dis)continuous Galerkin method, the domain is split into space-time slabs which are tessellated with space-time finite elements. On these elements, we define local basis functions to approximate the wave field and, define the test functions and variations. The local basis functions are defined such that the approximation of the wave field is discontinuous in space, but continuous in time. This kind of approximation is mainly chosen to satisfy the requirement of zero variation of the velocity potential at the end points in time.

The space-time variational formulation for this problem is obtained in two steps. In the first step, we establish a relation between the velocity field and velocity potential through the primal formulation given in Arnold et al. [5] and Brezzi et al. [15]. In the second step, we consider a discrete functional which is analogous to the continuum functional for linear free surface waves. Subsequently, we use Luke's variational principle to obtain a discrete variational problem for the linear free surface wave problem.

The space-time discretization of the discrete variational formulation for linear free surface waves results into a linear algebraic system of equations. The global matrix of this linear system has a very compact stencil, *i.e.,* the number of non-zero entries in each row of the matrix only depends on the number of neighbors of an element. Further, the linear system is symmetric and we can therefore use an efficient sparse matrix storage routine and an (iterative) sparse linear solver. The requirement to use efficient solver led us

to the PETSc package (see [52, 53, 54]) for assembling and solving the linear system of algebraic equations. The software library of PETSc has a large suite of well-tested sparse matrix storage routines and (iterative) sparse linear solvers with the extra advantage of parallelization options. Hence, we have incorporated the PETSc package in our numerical implementation. Within PETSc, we have used an efficient block sparse matrix storage routine for assembling the global matrix and a conjugate-gradient solver with ILU preconditioner for solving the linear system.

We have compared the variational space-time (dis)continuous Galerkin method with the "standard" space-time discontinuous Galerkin method developed by van der Vegt and Xu [65]. Hence, we also discuss the space-time discontinuous Galerkin method, which numerical implementation we extended to three space dimensions. The numerical results from both the variational and standard space-time (dis)continuous Galerkin methods are compared with two exact solutions: linear harmonic waves in a periodic domain and linear waves generated in a wave basin. We found for all the three dimensional test cases that both the numerical schemes are second order accurate for a linear polynomial approximation of the wave field. We also compare the present numerical scheme with the space-time DG scheme proposed by van der Vegt and Xu [65].

This chapter is organized as follows. We present Luke's variational formulation for linear free surface wave problem and subsequently derive the governing equations in §4.2. Tessellation of space-time domain, and the required function spaces and trace operators for the space-time finite element formulations are presented in §4.3. We present the standard and variational space-time (dis)continuous Galerkin finite element formulations of the linear free surface wave problem next in §4.4 and §4.5, respectively. Numerical results of the standard and variational space-time discontinuous Galerkin schemes are presented and compared in §4.6. Conclusions are drawn in §4.7.

4.2 Linear free surface gravity water waves

In fluid dynamics, the governing equations for free surface gravity water waves are derived from the incompressible Euler equations of fluid motion (see Johnson [27] or Whitham [69]). These governing equations can, how-

ever, also be derived from Luke's variational principle [39]. The advantage of using this principle is that the governing equations are obtained from a single energy functional. Conservation laws are thus directly associated with this variational principle via Noether's theorem. We therefore derive the linear free surface gravity water wave equations using Luke's variational principle.

4.2.1 Luke's variational principle

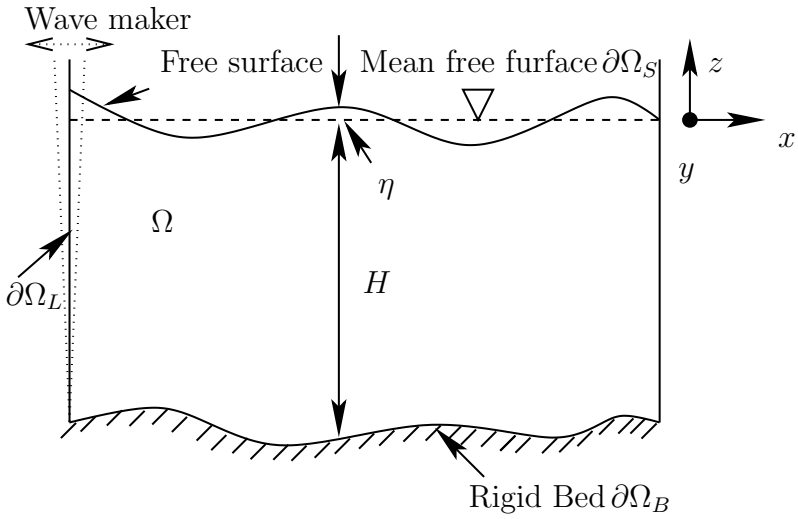

Figure 4.1: A sketch of the domain and its boundaries for the linear water wave problem including the waves generated by a wave maker. The flat mean free surface (top) and the fixed solid wall (left) for the wave maker arise as the fixed boundaries due to the linearization of the nonlinear free surface and the surface of the moving wave maker.

Consider an incompressible and inviscid fluid in a domain $\Omega \subset \mathbf{R}^3$ with boundaries $\partial\Omega = \partial\Omega_S \cup \partial\Omega_B \cup \partial\Omega_L$ as shown in Fig. 4.1, where $\partial\Omega_S$ is the free surface, $\partial\Omega_B$ is the rigid bed, and $\partial\Omega_L$ denotes lateral boundaries. Assuming a non-overturning free surface, we parameterize the free surface as $z = \eta(t, x, y)$, where $\eta(t, x, y)$ is a perturbation of the free surface around

a mean free surface located at $z = 0$ and measured at a height $H(x, y)$ from the rigid bottom surface $\partial\Omega_B$.

For free surface gravity water waves, it is justified to assume the flow field to be irrotational. It guarantees the existence of a velocity potential ϕ. Hence, $\mathbf{u} = \bar{\nabla}\phi$ such that $\bar{\nabla} \times \mathbf{u} = 0$ with $\bar{\nabla} = (\partial_x, \partial_y, \partial_z)^T$, $\mathbf{u} = (u, v, w)$ the velocity field, and u, v and w the components of the velocity in the x, y and z direction, respectively. We assume the perturbations of the free surface wave height η and the velocity potential ϕ to be of small amplitude. After linearization, the mean free surface $\partial\Omega_S$ instead of actual free surface and solid (vertical) walls $\partial\Omega_L$ instead of the wave makers emerge as the boundaries of the flow domain $\partial\Omega_S$ (see Fig. 4.1) for the linear problem.

To facilitate the use of Luke's variational principle, we first introduce a horizontal cross section of the flow domain Ω as $\bar{\Omega}(z)$ such that the flow domain Ω is obtained as

$$\Omega := \{(x, y, z) |\ 0 < z < -H \text{ and } (x, y) \in \bar{\Omega}(z)\}. \tag{4.1}$$

Next, we define the kinetic energy E_K and potential energy E_P of the waves in the flow domain Ω as

$$\begin{aligned} E_K &:= \int_\Omega \frac{1}{2} |\bar{\nabla}\phi|^2 \, \mathrm{d}\Omega - \int_{\partial\Omega_L} g_N \phi \, \mathrm{d}(\partial\Omega) \quad \text{and} \\ E_P &:= \int_{\partial\Omega_S} \frac{1}{2} g\eta^2 \, \mathrm{d}x \, \mathrm{d}y \end{aligned} \tag{4.2}$$

with g the gravitational acceleration and g_N a prescribed normal velocity at the lateral boundaries. Finally, we define the functional for linear free surface waves as

$$\mathcal{L}_f(\phi, \phi_s, \eta) = \int_0^T \int_{\partial\Omega_S} \phi_s \partial_t \eta \, \mathrm{d}x \, \mathrm{d}y \, \mathrm{d}t - \int_0^T (E_K + E_P) \, \mathrm{d}t \tag{4.3}$$

with T the final time, $\phi_s(x, y, t) = \phi(x, y, z = 0, t)$ the velocity potential evaluated at the free surface. The functional $\mathcal{L}_f(\phi, \phi_s, \eta)$ for the nonlinear case was originally defined by Luke [39].

The variational formulation for linear free surface waves is as follows:

$$\delta\mathcal{L}_f(\phi, \phi_s, \eta) = 0, \tag{4.4}$$

where $\delta\mathcal{L}_f(\phi,\phi_s,\eta)$ is the variational derivative. The variational derivative is defined by

$$\delta\mathcal{L}_f(\phi,\phi_s,\eta) := \lim_{\epsilon\to 0}\frac{1}{\epsilon}\Big(\mathcal{L}_f(\phi+\epsilon\delta\phi,\phi_s+\epsilon\delta\phi_s,\eta+\epsilon\delta\eta)-\mathcal{L}_f(\phi,\phi_s,\eta)\Big) \tag{4.5}$$

with $\delta\phi,\delta\phi_s$ and $\delta\eta$ arbitrary variations of ϕ,ϕ_s and η, respectively. The variational formulation (4.6) will form the basis to obtain the novel variational (dis)continuous Galerkin finite element discretization.

Applying Luke's variational principle (4.4) and using the definition of the variational derivative (4.5), we get

$$\int_0^T\Bigg(\int_{\partial\Omega_S}\big((\partial_t\eta)\delta\phi_s+\phi_s\partial_t\big)(\delta\eta)\,\mathrm{d}x\,\mathrm{d}y-\int_\Omega\bar\nabla\phi\cdot\bar\nabla(\delta\phi)\,\mathrm{d}\Omega + \int_{\partial\Omega_L}g_N\delta\phi\,\mathrm{d}(\partial\Omega)-\int_{\partial\Omega_S}g\eta\delta\eta\,\mathrm{d}(\partial\Omega)\Bigg)\,\mathrm{d}t=0. \tag{4.6}$$

To obtain the governing equations for linear free surface waves from the variational formulation (4.6), we integrate the the second term by parts and use Gauss' divergence theorem for the third term, and rearrange the boundary integrals using the end point conditions on the variation $\delta\eta(x,y,0)=\delta\eta(x,y,T)=0$. Hence, from (4.6) we derive

$$\int_0^T\Bigg(\int_{\partial\Omega_S}\Big(-(\partial_t\phi_s+g\eta)\delta\eta+(\partial_t\eta-\partial_z\phi)\delta\phi_s\Big)\,\mathrm{d}x\,\mathrm{d}y+\int_\Omega\bar\nabla^2\phi\,\delta\phi\,\mathrm{d}\Omega - \int_{\partial\Omega_L}(\tilde n_L\bar\nabla\cdot\phi-g_N)\delta\phi\,\mathrm{d}(\partial\Omega)-\int_{\partial\Omega_B}(\tilde{\mathbf{n}}_B\cdot\bar\nabla\phi)\delta\phi\,\mathrm{d}(\partial\Omega)\Bigg)\mathrm{d}t=0, \tag{4.7}$$

where $\tilde{\mathbf{n}}_L=(\pm1,0,0)^T$ and $\tilde{\mathbf{n}}_B$ are the outward unit normal vectors at the boundaries $\partial\Omega_L$ and $\partial\Omega_B$, respectively. Using the arbitrariness of the variations $\delta\phi$, $\delta\phi_s$ and $\delta\eta$ in (4.7), the governing equations for linear free surface gravity water waves emerge

$$\begin{aligned}\bar\nabla^2\phi=0 \quad &\text{on} \quad \Omega(t),\\ \partial_t\eta-\partial_z\phi=0 \quad &\text{and} \quad \partial_t\phi_s+g\eta=0 \text{ on } \partial\Omega_S,\\ \tilde{\mathbf{n}}_L\cdot\bar\nabla\phi=g_N \text{ on } \partial\Omega_L, \quad &\text{and} \quad \tilde{\mathbf{n}}_B\cdot\bar\nabla\phi=0 \text{ on } \partial\Omega_B.\end{aligned} \tag{4.8}$$

4.3 Basis for space-time formulation

4.3.1 Space-time domain and tesellation

In space-time discontinuous Galerkin methods, we do not distinguish between space and time, and directly define the space-time flow domain $\mathcal{E} \in \mathbb{R}^4$ as

$$\mathcal{E} := \{\mathbf{x} \in \mathbb{R}^4 : \bar{\mathbf{x}} \in \Omega, t_0 < t < T)\} \subseteq \mathbb{R}^4 \tag{4.9}$$

with $\mathbf{x} = (t, \mathbf{x})$ the space-time coordinates, $\bar{\mathbf{x}} = (x, y, z)$ the spatial coordinates, t_0 the initial time, T the final time and $\Omega \in \mathbb{R}^3$ the flow domain. The space-time boundary $\partial\mathcal{E}$ consists of the hypersurfaces $\Omega_0 := \{\mathbf{x} \in \partial\mathcal{E} : t = t_0\}$, $\Omega_T := \{\mathbf{x} \in \partial\mathcal{E} : t = T\}$ and $\mathcal{Q} := \{\mathbf{x} \in \partial\mathcal{E} : t_0 < t < T\}$. The unit outward space-time normal vector of the space-time domain boundary is defined as $\mathbf{n} := (n_t, \bar{\mathbf{n}})$ with n_t the temporal component and $\bar{\mathbf{n}}$ the spatial component.

To tessellate the space-time domain $\mathcal{E}$, we first divide the time interval $I = [t_0, T]$ into N_T time intervals with each time interval denoted as $I_n = [t_{n-1}, t_n]$. Second, at each time level t_n, we tessellate the flow domain Ω with N_e shape regular spatial elements K_{k}^n to form a computational flow domain Ω_{h} such that $\Omega_{\mathsf{h}} \to \Omega$ as $\mathsf{h} \to 0$, where h is the radius of the smallest sphere containing all elements K_{k}^n with $\mathsf{k} = 1, \ldots, N_e$. Finally, in each time interval I_n, we obtain the space-time tessellation $\mathcal{T}_{\mathsf{h}}^n$ for the computational space-time domain $\mathcal{E}_{\mathsf{h}}^n$ which consists of the space-time elements $\mathcal{K}_{\mathsf{k}}^n$ obtained by joining the spatial elements K_{k}^{n-1} and K_{k}^n at the successive time intervals t_{n-1} and t_n. For linear free surface waves, the computational flow domain Ω_{h} is fixed in time and hence the corresponding spatial elements K_{k}^{n-1} and K_{k}^n of the space-time element $\mathcal{K}_{\mathsf{k}}^n$ are identical. Hereafter, we thus drop the superscript n of the spatial element.

To define function spaces and apply quadrature rules, each spatial element K_{k} is mapped onto a reference element $\hat{K}$ and its mapping $F_K : \hat{K} \to K_{\mathsf{k}}$ is defined as

$$F_K : \hat{K} \to K_{\mathsf{k}} : \bar{\zeta} \mapsto \bar{\mathbf{x}} := \sum_{\mathsf{j}} \bar{\mathbf{x}}_{\mathsf{j}} \, \chi_{\mathsf{j}}(\bar{\zeta}) \tag{4.10}$$

with $\bar{\zeta} = (\zeta_1, \zeta_2, \zeta_2)$ the spatial reference coordinates, $\bar{\mathbf{x}} = (x, y, z)$ the spatial coordinates, $\bar{\mathbf{x}}_{\mathsf{j}}$ the nodal coordinates of the spatial element and

$\chi_{\mathsf{j}}(\bar{\zeta})$ the standard shape functions of element K_{k}. Subsequently, the space-time element $\mathcal{K}^n_{\mathsf{k}}$ is mapped to a reference element $\hat{\mathcal{K}}$ and its mapping is defined as

$$G^n_{\mathcal{K}} : \hat{\mathcal{K}} \to \mathcal{K}^n_{\mathsf{k}} : \zeta \mapsto \mathbf{x} := \Big(\frac{1}{2}\big((1+\zeta_0)t_n + (1-\zeta_0)t_{n-1}\big), F_K(\bar{\zeta})\Big) \quad (4.11)$$

with $\zeta = (\zeta_0, \bar{\zeta})$ the space-time reference coordinates.

In the space-time tessellation $\mathcal{T}^n_{\mathsf{h}}$, we further define interior faces $\mathcal{S}_{int}$, which connect two space-time elements $\mathcal{K}^n_{\mathsf{l}}$ and $\mathcal{K}^n_{\mathsf{r}}$, and boundary faces $\mathcal{S}_{bou}$ which connect space-time elements $\mathcal{K}^n_{\mathsf{l}}$ to the boundary $\partial\mathcal{E}$. The union of all faces in the space-time domain $\mathcal{E}^n_{\mathsf{h}}$ is represented as $\Gamma = \Gamma_{int} \cup \Gamma_{bou}$, with Γ_{int} the union of interior faces and Γ_{bou} the union of boundary faces. The union of boundary faces $\Gamma_{bou} := \Gamma_S \cup \Gamma_B \cup \Gamma_L$ further consists of Γ_S the union of free surface faces, Γ_B the union of rigid boundary faces and Γ_L the union of lateral boundary faces of the computational space-time domain $\mathcal{E}^n_{\mathsf{h}}$ which may include a wave maker.

4.3.2 Function spaces

To define the space-time discontinuous Galerkin formulation, we introduce the finite element function spaces V_{h} and Σ_{h} associated with the space-time tessellation $\mathcal{T}^n_{\mathsf{h}}$ which are defined as

$$\begin{aligned} V_{\mathsf{h}} &:= \{v_{\mathsf{h}} \in L^2(\mathcal{E}^n_{\mathsf{h}}) :\ v_{\mathsf{h}} \circ G^n_{\mathcal{K}} \in \mathcal{P}_p(\hat{\mathcal{K}}),\ \forall \mathcal{K}^n_{\mathsf{k}} \in \mathcal{T}^n_{\mathsf{h}}\}, \\ \Sigma_{\mathsf{h}} &:= \{\tau_{\mathsf{h}} \in L^2(\mathcal{E}^n_{\mathsf{h}}) :\ \tau_{\mathsf{h}} \circ G^n_{\mathcal{K}} \in [\mathcal{P}_p(\hat{\mathcal{K}})]^3,\ \forall \mathcal{K}^n_{\mathsf{k}} \in \mathcal{T}^n_{\mathsf{h}}\} \end{aligned} \quad (4.12)$$

with $L^2(\mathcal{E}^n_{\mathsf{h}})$ the space of Lebesgue square integrable functions on $\mathcal{E}^n_{\mathsf{h}}$ and $\mathcal{P}_p$ polynomials of order p. We also introduce the function space W_{h} associated with the space-time free surface Γ_S which is defined as

$$W_{\mathsf{h}} := \{v_{\mathsf{h}} \in L^2(\Gamma_S) :\ v_{\mathsf{h}} \circ G_{\mathcal{K}} \in \mathcal{P}_p(\hat{\mathcal{S}}),\ \forall \mathcal{S} \subset \Gamma_S\}, \quad (4.13)$$

with $\hat{\mathcal{S}}$ a face of $\hat{\mathcal{K}}$ and $L^2(\Gamma_S)$ the space of Lebesgue square integrable functions on the space-time free surface boundary Γ_S.

For the space-time discontinuous Galerkin formulation, we approximate flow fields $(\mathbf{u}, \phi, \eta)$ as

$$\phi_{\mathsf{h}} = \sum_{j=1}^{n_p} \hat{\phi}_{\mathsf{k},j}\psi_{\mathsf{k},j}, \quad \mathbf{u}_{\mathsf{h}} = \sum_{j=1}^{n_p} \hat{\mathbf{u}}_{\mathsf{k},j}\psi_{\mathsf{k},j} \quad \text{and} \quad \eta_{\mathsf{h}} = \sum_{j=1}^{n_q} \hat{\eta}_{\mathsf{k},j}\varphi_{\mathsf{k},j}, \quad (4.14)$$

with $\phi_\mathsf{h} \in V_\mathsf{h}$, $\mathbf{u}_\mathsf{h} \in \Sigma_\mathsf{h}$ and $\eta_\mathsf{h} \in W_\mathsf{h}$ the approximated wave fields; $(\hat{\phi}_{\mathsf{k},j}, \hat{\mathbf{u}}_{\mathsf{k},j}, \hat{\eta}_{\mathsf{k},j})$ the expansion coefficients; $\psi_{\mathsf{k},j} \circ G^n_\mathcal{K} \in \mathcal{P}_p(\hat{\mathcal{K}})$ and $\varphi_{\mathsf{k},j} \circ G^n_\mathcal{K} \in \mathcal{P}_p(\hat{\mathcal{S}})$ the polynomial basis functions; and, n_p and n_q the number of basis functions in the space-time elements and at the space-time free surface, respectively.

To define the space-time variational formulation, we introduce the finite element function spaces $\bar{V}_\mathsf{h}$ and $\bar{\Sigma}_\mathsf{h}$ associated with the computational space domain Ω_h which are defined as

$$\begin{aligned} \bar{V}_\mathsf{h} &:= \{\bar{v}_\mathsf{h} \in L^2(\Omega_\mathsf{h}) : \ \bar{v}_\mathsf{h} \circ F_K \in \mathcal{P}_p(\hat{K})\}, \\ \bar{\Sigma}_\mathsf{h} &:= \{\bar{\tau}_\mathsf{h} \in L^2(\Omega_\mathsf{h}) : \ \bar{\tau}_\mathsf{h} \circ F_K \in [\mathcal{P}_p(\hat{K})]^3\}, \end{aligned} \tag{4.15}$$

where $L^2(\Omega_\mathsf{h})$ is the space of Lebesgue square integrable functions on Ω_h and $\mathcal{P}_p$ the polynomials of order p. We also introduce the function space $\bar{W}_\mathsf{h}$ associated with the free surface $\partial\Omega_S$ which is defined as

$$\bar{W}_\mathsf{h} := \{\bar{v}_\mathsf{h} \in L^2(\partial\Omega_S) : \ \bar{v}_\mathsf{h} \circ F_K \in \mathcal{P}_p(\hat{S})\} \tag{4.16}$$

with $\hat{S}$ a face of $\hat{K}$ and $L^2(\partial\Omega_S)$ the space of Lebesgue square integrable functions on the free surface $\partial\Omega_S$.

For the space-time variational formulation, we first approximate the flow field $(\mathbf{u}, \phi, \eta)$ on the computational space domain Ω_h at time level t_n as

$$\bar{\phi}^n_\mathsf{h} = \sum_{j=1}^{n_p} \hat{\phi}^n_{\mathsf{k},j} \bar{\psi}_{\mathsf{k},j}, \quad \bar{\mathbf{u}}^n_\mathsf{h} = \sum_{j=1}^{n_p} \hat{\mathbf{u}}^n_{\mathsf{k},j} \bar{\psi}_{\mathsf{k},j} \quad \text{and} \quad \bar{\eta}^n_\mathsf{h} = \sum_{j=1}^{n_q} \hat{\eta}^n_{\mathsf{k},j} \bar{\varphi}_{\mathsf{k},j} \tag{4.17}$$

with $\bar{\phi}^n_\mathsf{h}, \bar{\mathbf{u}}^n_\mathsf{h}, \bar{\eta}^n_\mathsf{h}$ the approximated flow fields; $(\hat{\phi}^n_{\mathsf{k},i}, \hat{\mathbf{u}}^n_{\mathsf{k},i}, \hat{\eta}^n_{\mathsf{k},j})$ the expansion coefficients; $\bar{\psi}_{\mathsf{k},j} \circ F_K \in \mathcal{P}_p(\hat{K})$ and $\bar{\varphi}_{\mathsf{k},j} \circ F^n_K \in \mathcal{P}_p(\hat{S})$ the polynomial basis functions; and, n_p and n_q the number of basis functions in the spatial element and at the free surface, respectively.

Second, we define the polynomial basis functions in time ψ^{n-1} and ψ^n as follows

$$\psi^{n-1} := \frac{1}{2}(1 - \zeta_0)t_{n-1} \quad \text{and} \quad \psi^n := \frac{1}{2}(1 + \zeta_0)t_n. \tag{4.18}$$

Finally, we obtain the approximation of the wave field on each space-time element $\mathcal{K}^n_\mathsf{k}$ as

$$(\phi_\mathsf{h}, \mathbf{u}_\mathsf{h}, \eta_\mathsf{h}) = (\bar{\phi}^n_\mathsf{h}, \bar{\mathbf{u}}^n_\mathsf{h}, \bar{\eta}^n_\mathsf{h})\psi^n + (\bar{\phi}^{n-1}_\mathsf{h}, \bar{\mathbf{u}}^{n-1}_\mathsf{h}, \bar{\eta}^{n-1}_\mathsf{h})\psi^{n-1} \tag{4.19}$$

with $\bar{\phi}_\mathsf{h} \in \bar{V}_\mathsf{h}$, $\bar{\mathbf{u}}_\mathsf{h} \in \bar{\Sigma}_\mathsf{h}$ and $\bar{\eta}_\mathsf{h} \in \bar{W}_\mathsf{h}$ with the restriction that the approximation is continuous in time but discontinuous in space.

4.3.3 Traces

To define and manipulate the numerical fluxes in the discontinuous Galerkin formulation, we define the traces of functions $v \in V_\mathsf{h}$ and vector functions $\mathbf{q} \in \Sigma_\mathsf{h}$ on the element boundary $\partial\mathcal{K}^n_\mathsf{k}$ taken from inside of the element $\mathcal{K}^n_\mathsf{k}$ as

$$v_\mathsf{h}|_{\partial\mathcal{K}^n_\mathsf{k}} := v^- = \lim_{\epsilon\downarrow 0} v(\mathbf{x} - \epsilon\mathbf{n}_\mathcal{K}) \text{ and } \mathbf{q}_\mathsf{h}|_{\partial\mathcal{K}^n_\mathsf{k}} := \mathbf{q}^- := \lim_{\epsilon\downarrow 0} \mathbf{q}(\mathbf{x} - \epsilon\mathbf{n}_\mathcal{K}) \tag{4.20}$$

with $n_\mathcal{K}$ the unit outward normal vector of the element boundary $\partial\mathcal{K}^n_\mathsf{k}$. For convenience, we also denote the traces v^- and $\mathbf{q}^-$ on $\partial\mathcal{K}^n_\mathsf{k}$ as v_k and $\mathbf{q}_\mathsf{k}$, respectively. Now, we define the following trace operators:

Definition 4.3.1 (Average). *The averages $\{\!\{v\}\!\}$ of a scalar function $v \in V_\mathsf{h}$ and $\{\!\{\mathbf{q}\}\!\}$ of a vector function $\mathbf{q} \in \Sigma_\mathsf{h}$ on a face $\mathcal{S} \in \Gamma$ are defined as*

$$\begin{array}{llll} \{\!\{v\}\!\} & := \frac{1}{2}(v_\mathsf{l} + v_\mathsf{r}), & \{\!\{\mathbf{q}\}\!\} & := \frac{1}{2}(\mathbf{q}_\mathsf{l} + \mathbf{q}_\mathsf{r}) \quad \forall \mathcal{S} \in \Gamma_{int}; \text{ and} \\ \{\!\{v\}\!\} & := v_\mathsf{l}, & \{\!\{\mathbf{q}\}\!\} & := \mathbf{q}_\mathsf{l} \quad \forall \mathcal{S} \in \Gamma_{bou} \end{array} \tag{4.21}$$

with v_l and v_r the traces of the scalar function v_h, and $\mathbf{q}_\mathsf{l}$ and $\mathbf{q}_\mathsf{r}$ the traces of the vector function $\mathbf{q}_\mathsf{h}$ taken from the inside of the elements $\mathcal{K}^n_\mathsf{l}$ and $\mathcal{K}^n_\mathsf{r}$ which are connected at the face $\mathcal{S}$.

Definition 4.3.2 (Jump). *The jumps $[\![v]\!]$ of a scalar function $v \in V_\mathsf{h}$ and $[\![\mathbf{q}]\!]$ of a vector function $\mathbf{q} \in \Sigma_\mathsf{h}$ on a face $\mathcal{S} \in \Gamma$ are defined as*

$$\begin{array}{llll} [\![v]\!] & := v_\mathsf{l}\bar{\mathbf{n}}^\mathsf{l}_\mathcal{K} + v_r\bar{\mathbf{n}}^r_\mathcal{K}, & [\![\mathbf{q}]\!] & := \mathbf{q}_\mathsf{l} \cdot \bar{\mathbf{n}}^\mathsf{l}_\mathcal{K} + \mathbf{q}_\mathsf{r} \cdot \bar{\mathbf{n}}^\mathsf{r}_\mathcal{K} \quad \forall \mathcal{S} \in \Gamma_{int}; \text{ and} \\ [\![v]\!] & := v_\mathsf{l}\bar{\mathbf{n}}^\mathsf{l}_\mathcal{K}, & [\![\mathbf{q}]\!] & := \mathbf{q}_\mathsf{l} \cdot \bar{\mathbf{n}}^\mathsf{l}_\mathcal{K} \quad \forall \mathcal{S} \in \Gamma_{bou} \end{array} \tag{4.22}$$

with $\bar{\mathbf{n}}^\mathsf{l}_\mathcal{K}$ and $\bar{\mathbf{n}}^\mathsf{r}_\mathcal{K}$ the spatial part of the unit space-time normal vectors $\mathbf{n}^\mathsf{l}_\mathcal{K} = (n^\mathsf{l}_t, \bar{\mathbf{n}}^\mathsf{l}_\mathcal{K})$ and $\mathbf{n}^\mathsf{r}_\mathcal{K} = (n^\mathsf{r}_t, \bar{\mathbf{n}}^\mathsf{r}_\mathcal{K})$ of the elements $\mathcal{K}^n_\mathsf{l}$ and $\mathcal{K}^n_\mathsf{r}$, respectively, at the face $\mathcal{S}$. Note that $\bar{\mathbf{n}}^\mathsf{l}_\mathcal{K} = -\bar{\mathbf{n}}^\mathsf{r}_\mathcal{K}$.

Now the following relation holds between jumps and averages:

$$\sum_{\mathcal{K}} \int_{\partial \mathcal{K}_{\mathsf{k}}^n} v^- (\bar{\mathbf{n}}_{\mathcal{K}} \cdot \mathbf{q}^-) \, \mathrm{d}(\partial \mathcal{K}) = \int_{\Gamma} [\![v]\!] \cdot \{\!\{ \mathbf{q} \}\!\} \, \mathrm{d}\mathcal{S} + \int_{\Gamma_{int}} \{\!\{ v \}\!\} [\![\mathbf{q}]\!] \, \mathrm{d}\mathcal{S}. \quad (4.23)$$

Further, we can deduce the following properties of trace operators:

$$\begin{gathered} [\![f \pm g]\!] = [\![f]\!] \pm [\![g]\!], \quad \{\!\{ f \pm g \}\!\} = \{\!\{ f \}\!\} \pm \{\!\{ g \}\!\}, \\ \{\!\{ \{\!\{ f \}\!\} \}\!\} = \{\!\{ f \}\!\} \quad \text{and} \quad [\![\{\!\{ f \}\!\}]\!] = 0 \end{gathered} \quad (4.24)$$

with $f, g \in V_{\mathsf{h}}$ or Σ_{h}.

4.3.4 Global and local lifting operators

For the standard space-time discontinuous Galerkin formulation, we need to define the global lifting operator $\mathcal{R} : (L^2(\Gamma))^3 \to \Sigma_{\mathsf{h}}$ as

$$\int_{\mathcal{E}_{\mathsf{h}}^n} \mathcal{R}(p) \cdot \tau \, \mathrm{d}\mathcal{K} := \int_{\Gamma} p \cdot \{\!\{ \tau \}\!\} \, \mathrm{d}\mathcal{S} \quad (4.25)$$

and the local lifting operator $\mathcal{R}_{\mathcal{S}} : (L^2(\mathcal{S}))^3 \to \Sigma_{\mathsf{h}}$ as

$$\int_{\mathcal{E}_{\mathsf{h}}^n} \mathcal{R}_{\mathcal{S}}(p) \cdot \tau \, \mathrm{d}\mathcal{K} := \int_{\mathcal{S}} p \cdot \{\!\{ \tau \}\!\} \, \mathrm{d}\mathcal{S}. \quad (4.26)$$

Since $\Gamma = \bigcup \mathcal{S}$ is the union of all faces $\mathcal{S}$, we can relate the global and local lifting operators as

$$\int_{\mathcal{E}_{\mathsf{h}}^n} \mathcal{R}(p) \cdot \tau \, \mathrm{d}\mathcal{K} = \sum_{\mathcal{S}} \int_{\mathcal{S}} p \cdot \{\!\{ \tau \}\!\} \, \mathrm{d}\mathcal{S} = \sum_{\mathcal{S}} \int_{\mathcal{E}_{\mathsf{h}}^n} \mathcal{R}_{\mathcal{S}}(p) \cdot \tau \, \mathrm{d}\mathcal{K}. \quad (4.27)$$

The global and local lifting operator $\mathcal{R}(p)$ and $\mathcal{R}_{\mathcal{S}}(p)$ can be further split per space-time element $\mathcal{K}_{\mathsf{k}}^n$ as

$$\begin{aligned} \int_{\mathcal{E}_{\mathsf{h}}^n} \mathcal{R}(p) \cdot \tau \, \mathrm{d}\mathcal{K} &= \sum_{\mathcal{K}} \int_{\mathcal{K}_{\mathsf{k}}^n} \mathcal{R}_{\mathsf{k}}(p) \cdot \tau_{\mathsf{k}} \, \mathrm{d}\mathcal{K} \quad \text{and} \\ \int_{\mathcal{E}_{\mathsf{h}}^n} \mathcal{R}_{\mathcal{S}}(p) \cdot \tau \, \mathrm{d}\mathcal{K} &= \sum_{\mathcal{K}} \int_{\mathcal{K}_{\mathsf{k}}^n} \mathcal{R}_{\mathcal{S},\mathsf{k}}(p) \cdot \tau_{\mathsf{k}} \, \mathrm{d}\mathcal{K} \end{aligned} \quad (4.28)$$

with $\mathcal{R}_{\mathsf{k}}(p)$ the global lifting operator, $\mathcal{R}_{\mathcal{S},\mathsf{k}}(p)$ the local lifting operator and τ_{k} the test function per space-time element $\mathcal{K}^n_{\mathsf{k}}$. Now using the arbitrariness of the test functions τ, we can find that the local lifting operator of a face $\mathcal{S}$ is non zero only w.r.t the elements $\mathcal{K}^n_{\mathsf{l}}$ and $\mathcal{K}^n_{\mathsf{r}}$ connected to it because using (4.28) in (4.26), we get

$$\int_{\mathcal{K}^n_{\mathsf{l}}} \mathcal{R}_{\mathcal{S},\mathsf{l}}(p) \cdot \tau_{\mathsf{l}} \, \mathrm{d}\mathcal{K} + \int_{\mathcal{K}^n_{\mathsf{r}}} \mathcal{R}_{\mathcal{S},\mathsf{r}}(p) \cdot \tau_{\mathsf{r}} \, \mathrm{d}\mathcal{K} = \frac{1}{2} \int_{\mathcal{S}} p \cdot \tau_{\mathsf{l}} \, \mathrm{d}\mathcal{S} + \frac{1}{2} \int_{\mathcal{S}} p \cdot \tau_{\mathsf{r}} \, \mathrm{d}\mathcal{S}. \tag{4.29}$$

Moreover, we obtain the local lifting operators per space-time element $\mathcal{K}^n_{\mathsf{k}}$ from (4.29) as

$$\int_{\mathcal{K}^n_{\mathsf{k}}} \mathcal{R}_{\mathcal{S},\mathsf{k}}(p) \cdot \tau_k = \int_{\mathcal{S}} \frac{1}{2} p \cdot \tau_{\mathsf{k}} \, \mathrm{d}\mathcal{S} \quad \text{with } \mathcal{S} \subseteq \partial\mathcal{K}^n_{\mathsf{k}}. \tag{4.30}$$

The global and local lifting operators can be further related per space-time element $\mathcal{K}^n_{\mathsf{k}}$ using (4.28) and (4.29) in (4.27) as

$$\begin{aligned} \sum_{\mathcal{K}} \int_{\mathcal{K}^n_{\mathsf{k}}} \mathcal{R}_{\mathsf{k}}(p) \cdot \tau_{\mathsf{k}} \, \mathrm{d}\mathcal{K} &= \sum_{\mathcal{S}} \int_{\mathcal{E}^n_{\mathsf{h}}} \mathcal{R}_{\mathcal{S}}(p) \cdot \tau \, \mathrm{d}\mathcal{K} \\ &= \sum_{\mathcal{S}} \Big(\int_{\mathcal{K}^n_{\mathsf{l}}} \mathcal{R}_{\mathcal{S},\mathsf{l}}(p) \cdot \tau_{\mathsf{l}} \, \mathrm{d}\mathcal{K} + \int_{\mathcal{K}^n_{\mathsf{r}}} \mathcal{R}_{\mathcal{S},\mathsf{r}}(p) \cdot \tau_{\mathsf{r}} \, \mathrm{d}\mathcal{K} \Big) \\ &= \sum_{\mathcal{K}} \int_{\mathcal{K}^n_{\mathsf{k}}} \Big(\sum_{\mathcal{S} \subset \partial\mathcal{K}^n_{\mathsf{k}}} \mathcal{R}_{\mathcal{S},\mathsf{k}}(p) \Big) \cdot \tau_{\mathsf{k}} \, \mathrm{d}\mathcal{K} \end{aligned} \tag{4.31}$$

and thus,

$$\mathcal{R}_{\mathsf{k}}(p) = \sum_{\mathcal{S} \subset \partial\mathcal{K}^n_{\mathsf{k}}} \mathcal{R}_{\mathcal{S},\mathsf{k}}(p). \tag{4.32}$$

4.3.5 Primal relation

To obtain the standard space-time DG formulation and the variational space-time DG formulation, we establish a relation between the approximations of velocity field $\mathbf{u}_{\mathsf{h}}$ and the velocity potential ϕ_{h} using the primal

formulation introduced by Arnold et al. [5] and Brezzi et al. [15]. For the primal formulation, we use the product rule

$$\bar{\nabla} \cdot (v\mathbf{q}) = \bar{\nabla} v \cdot \mathbf{q} + v(\bar{\nabla} \cdot \mathbf{q}), \tag{4.33}$$

with $v \in V_\mathsf{h}$ and $\mathbf{q} \in \Sigma_\mathsf{h}$, and the divergence theorem in space-time:

$$\begin{aligned}\int_{\mathcal{K}_\mathsf{k}^n} \bar{\nabla} \cdot (v\mathbf{q}) \, \mathrm{d}\mathcal{K} = \int_{\mathcal{K}_\mathsf{k}^n} \nabla \cdot (0, v\mathbf{q}) \, \mathrm{d}\mathcal{K} &= \int_{\partial\mathcal{K}_\mathsf{k}^n} \mathbf{n}_\mathcal{K} \cdot (0, v^- \mathbf{q}^-) \, \mathrm{d}(\partial\mathcal{K}) \\ &= \int_{\partial\mathcal{K}_\mathsf{k}^n} \bar{\mathbf{n}}_\mathcal{K} \cdot (v^- \mathbf{q}^-) \, \mathrm{d}(\partial\mathcal{K})\end{aligned} \tag{4.34}$$

with $\nabla := (\partial_t, \partial_x, \partial_y, \partial_z)^T$.

To obtain the primal formulation, we discretize the auxiliary equation $\mathbf{u} = \bar{\nabla}\phi$ in (4.8) by multiplying it with arbitrary test functions $\tau_\mathsf{h} \in \Sigma_\mathsf{h}$ and introducing the approximations of the velocity and potential field $\mathbf{u}_\mathsf{h} \in \Sigma_\mathsf{h}$ and $\phi_\mathsf{h} \in V_\mathsf{h}$, respectively. Next, we integrate by parts over each space-time element $\mathcal{K}_\mathsf{k}^n$ using (4.33), Gauss' divergence theorem in space-time and relation (4.23). We obtain after summation over all elements

$$\int_{\mathcal{E}_\mathsf{h}^n} \mathbf{u}_\mathsf{h} \cdot \tau_\mathsf{h} \, \mathrm{d}\mathcal{K} = -\int_{\mathcal{E}_\mathsf{h}^n} \phi_\mathsf{h} (\bar{\nabla} \cdot \tau_\mathsf{h}) \, \mathrm{d}\mathcal{K} + \int_\Gamma [\![\hat{\phi}]\!] \cdot \{\!\{\tau\}\!\} \, \mathrm{d}\mathcal{S} + \int_{\Gamma_{int}} \{\!\{\hat{\phi}\}\!\} [\![\tau]\!] \, \mathrm{d}\mathcal{S} \tag{4.35}$$

In (4.35), we have introduced a numerical flux for the velocity potential $\hat{\phi} = \hat{\phi}(\phi_\mathsf{l}, \phi_\mathsf{r})$ to take into account the multivalued traces ϕ_l and ϕ_r on each face $\mathcal{S} \in \Gamma$. The numerical flux $\hat{\phi}$ for elliptic problems (as suggested in Brezzi et al. [15]) is taken

$$\hat{\phi} := \{\!\{\phi_\mathsf{h}\}\!\} \text{ on } \mathcal{S} \in \Gamma_{int} \text{ and } \hat{\phi} := \phi_\mathsf{h} \text{ on } \mathcal{S} \in \Gamma_{bou}. \tag{4.36}$$

To obtain a primal relation between the velocity and potential field, we integrate (4.35) again by parts to get

$$\begin{aligned}\int_{\mathcal{E}_\mathsf{h}^n} \mathbf{u}_\mathsf{h} \cdot \tau_\mathsf{h} \mathrm{d}\mathcal{K} = &\int_{\mathcal{E}_\mathsf{h}^n} \bar{\nabla}\phi_\mathsf{h} \cdot \tau_\mathsf{h} \mathrm{d}\mathcal{K} + \\ &\int_\Gamma [\![\hat{\phi} - \phi_\mathsf{h}]\!] \cdot \{\!\{\tau\}\!\} \mathrm{d}\mathcal{S} + \int_{\Gamma_{int}} \{\!\{\hat{\phi} - \phi_\mathsf{h}\}\!\} [\![\tau]\!] \mathrm{d}\mathcal{S}.\end{aligned} \tag{4.37}$$

Now, we introduce the definition of global lifting operator (4.25) in (4.37) and use (4.36) to find

$$\int_{\mathcal{E}_{\mathsf{h}}^n} \mathbf{u}_{\mathsf{h}} \cdot \tau_{\mathsf{h}} \, \mathrm{d}\mathcal{K} = \int_{\mathcal{E}_{\mathsf{h}}^n} \left(\bar{\nabla} \phi_{\mathsf{h}} + \mathcal{R}(\llbracket \hat{\phi} - \phi_{\mathsf{h}} \rrbracket) \right) \cdot \tau_{\mathsf{h}} \, \mathrm{d}\mathcal{K}. \tag{4.38}$$

Since test functions τ_{h} are arbitrary, we have established the primal relation between $\mathbf{u}_{\mathsf{h}}$ and ϕ_{h} to be

$$\mathbf{u}_{\mathsf{h}} = \bar{\nabla} \phi_{\mathsf{h}} + \mathcal{R}(\llbracket \hat{\phi} - \phi_{\mathsf{h}} \rrbracket). \tag{4.39}$$

4.4 Standard space-time discontinuous Galerkin method

4.4.1 Weak formulation

The weak formulation of the velocity potential describing the free surface waves is obtained by multiplying the continuity equation $\bar{\nabla} \cdot \mathbf{u} = 0$ with arbitrary test functions $v \in V_{\mathsf{h}}$, introducing the approximated velocity field $\mathbf{u}_{\mathsf{h}} \in \Sigma_{\mathsf{h}}$, integrating by parts and applying Gauss' divergence theorem (4.34) in space-time. Summing up over all elements and using relation (4.23), we obtain

$$\int_{\mathcal{E}_{\mathsf{h}}^n} \mathbf{u}_{\mathsf{h}} \cdot \bar{\nabla} v \, \mathrm{d}\mathcal{K} = \int_{\Gamma} \hat{\mathbf{u}} \cdot \llbracket v \rrbracket \, \mathrm{d}\mathcal{S}. \tag{4.40}$$

In the weak formulation (4.40), we have introduced a numerical flux $\hat{\mathbf{u}}$ for the velocity field as

$$\hat{\mathbf{u}} \cdot \bar{\mathbf{n}} := \begin{cases} \{\!\{ \mathbf{u}_{\mathsf{h}} \}\!\} \cdot \bar{\mathbf{n}} & \text{on } \Gamma_{int}, \\ g_N & \text{on } \Gamma_L, \\ 0 & \text{on } \Gamma_B, \\ \mathbf{u}_{\mathsf{h}} \cdot \bar{\mathbf{n}} & \text{on } \Gamma_S. \end{cases} \tag{4.41}$$

Now, we eliminate the velocity field $\mathbf{u}_{\mathsf{h}}$ from (4.40) using the primal relation (4.39) and by coupling the kinematic free surface boundary condition in (4.8) through the numerical flux (4.41) as

$$\hat{\mathbf{u}} \cdot \bar{\mathbf{n}} = \mathbf{u}_{\mathsf{h}} \cdot \bar{\mathbf{n}} = \partial_z \phi_{\mathsf{h}} = \partial_t \eta_{\mathsf{h}}. \tag{4.42}$$

The weak formulation (4.40) now becomes

$$\int_{\mathcal{E}_{\mathsf{h}}^n} \bar{\nabla}\phi_{\mathsf{h}} \cdot \bar{\nabla} v \, \mathrm{d}\mathcal{K} + \int_{\mathcal{E}_{\mathsf{h}}^n} \mathcal{R}([\![\hat{\phi} - \phi_{\mathsf{h}}]\!]) \cdot \bar{\nabla} v \, \mathrm{d}\mathcal{K} = \int_{\Gamma_{int}} \{\!\{\bar{\nabla}\phi_{\mathsf{h}}\}\!\} \cdot [\![v]\!] \, \mathrm{d}\mathcal{S} + \int_{\Gamma_{int}} \{\!\{\mathcal{R}([\![\hat{\phi} - \phi_{\mathsf{h}}]\!])\}\!\} \cdot [\![v]\!] \, \mathrm{d}\mathcal{S} + \int_{\Gamma_L} g_N v \, \mathrm{d}\mathcal{S} + \int_{\Gamma_S} (\partial_t \eta_{\mathsf{h}}) v \, \mathrm{d}\mathcal{S}. \tag{4.43}$$

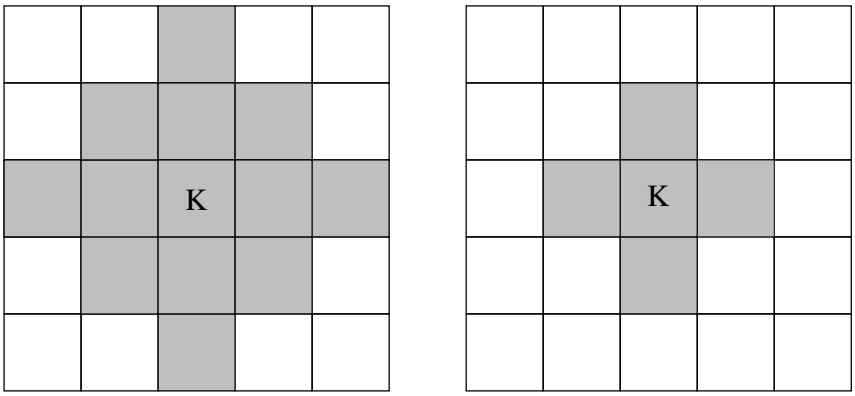

Figure 4.2: Sparsity of the global matrix w.r.t element K when using the global lifting operator $\mathcal{R}([\![\phi]\!])$ (left) and the approximate global lifting operator $n_{\mathcal{S}}\mathcal{R}_{\mathcal{S}}([\![\phi]\!])$ (right).

For the space-time DG discretization, it is advantageous to expand and simplify the global lifting operator in the L.H.S. (4.43) using (4.25) and (4.36) as

$$\int_{\mathcal{E}_{\mathsf{h}}^n} \mathcal{R}([\![\hat{\phi} - \phi_{\mathsf{h}}]\!]) \cdot \bar{\nabla} v \, \mathrm{d}\mathcal{K} = -\int_{\Gamma_{int}} [\![\phi_{\mathsf{h}}]\!] \cdot \{\!\{\bar{\nabla} v\}\!\} \mathrm{d}S. \tag{4.44}$$

Also, the global lifting operator in the R.H.S. of (4.43) is approximated as

$$\{\!\{\mathcal{R}([\![\phi_{\mathsf{h}}]\!])\}\!\} = \frac{1}{2}\left(\sum_{\mathcal{S} \subset \partial\mathcal{K}_{\mathsf{l}}^n} \mathcal{R}_{\mathcal{S},\mathsf{l}}([\![\phi_{\mathsf{h}}]\!]) + \sum_{\mathcal{S} \subset \partial\mathcal{K}_{\mathsf{l}}^n} \mathcal{R}_{\mathcal{S},\mathsf{r}}([\![\phi_{\mathsf{h}}]\!]) \right)$$

$$\approx n_{\mathcal{S}}\Big(\mathcal{R}_{\mathcal{S},\mathsf{l}}([\![\phi_{\mathsf{h}}]\!]) + \mathcal{R}_{\mathcal{S},\mathsf{r}}([\![\phi_{\mathsf{h}}]\!])\Big) = n_{\mathcal{S}}\mathcal{R}_{\mathcal{S}}([\![\phi_{\mathsf{h}}]\!]). \tag{4.45}$$

with $n_{\mathcal{S}}$ the number of faces of a space-time element. The approximation of the global lifting operator (4.45) improves the sparsity of the global matrix resulting from the discretization of (4.43) as depicted in Fig. 4.2. Substituting (4.44) and (4.45) in (4.43), we obtain the simplified weak formulation

$$\int_{\mathcal{E}_{\mathsf{h}}^n} \bar{\nabla}\phi_{\mathsf{h}} \cdot \bar{\nabla} v \,\mathrm{d}\mathcal{K} = \int_{\Gamma_{int}} [\![\phi_{\mathsf{h}}]\!] \cdot \{\!\{\bar{\nabla} v\}\!\} \,\mathrm{d}\mathcal{S} + \int_{\Gamma_{int}} \{\!\{\bar{\nabla}\phi_{\mathsf{h}}\}\!\} \cdot [\![v]\!] \,\mathrm{d}\mathcal{S} - \int_{\Gamma_{int}} n_{\mathcal{S}}\, \mathcal{R}_{\mathcal{S}}([\![\phi_{\mathsf{h}}]\!]) \cdot [\![v]\!] \mathrm{d}\mathcal{S} + \int_{\Gamma_N} g_N v \mathrm{d}\mathcal{S} + \int_{\Gamma_S} \partial_t \eta_{\mathsf{h}} \mathrm{d}\mathcal{S}. \tag{4.46}$$

Now it remains to relate the free surface height to the velocity potential using the dynamic free surface boundary condition. Multiplying the dynamic free surface boundary condition in (4.8) with arbitrary test functions $w_{\mathsf{h}} \in W_{\mathsf{h}}$, introducing the approximations η_{h} and ϕ_{h}, and integrating over each face $\mathcal{S}$ of the free surface Γ_S, we obtain

$$\int_{\Gamma_S} (\partial_t \phi_{\mathsf{h}} + g\eta_{\mathsf{h}}) w_{\mathsf{h}} \mathrm{d}\mathcal{S} = 0. \tag{4.47}$$

The weak formulation (4.46) and (4.47) in the space-time slab $\mathcal{E}_{\mathsf{h}}^n$ are not, however, coupled to the previous space-time slab $\mathcal{E}_{\mathsf{h}}^{n-1}$.

To couple the space-time slab, the last contribution in (4.46) is integrated by parts twice in time on each face $\mathcal{S} \in \Gamma_S$ of the free surface boundary, and we obtain after summing up over all free surfaces

$$\int_{\Gamma_S} (\partial_t \eta) v_{\mathsf{h}} \mathrm{d}\mathcal{S} = \int_{\Gamma_S} (\partial_t \eta) v_{\mathsf{h}} \mathrm{d}\mathcal{S} - \sum_{\mathcal{S}\in\Gamma_S} \int_{\partial\mathcal{S}} n_{\mathcal{S},t} (\hat{\eta} - \eta^-) v^- \mathrm{d}(\partial\mathcal{S}) \tag{4.48}$$

in which $n_{\mathcal{S},t}$ is the temporal component of the outward unit normal vector $\mathbf{n}_{\mathcal{S}}$ of the free surface boundary edge $\partial\mathcal{S}$ w.r.t. the free surface $\mathcal{S} \in \Gamma_S$, $\hat{\eta}$ is the numerical flux in time for the wave height η, and $\eta^- = \lim_{\epsilon\to 0} \eta_{\mathsf{h}}(t - \epsilon n_{\mathcal{S},t})$. Similarly, we also treat the time derivatives on ϕ in (4.47) to obtain

$$\int_{\Gamma_S} (\partial_t \phi) w_{\mathsf{h}} \mathrm{d}\mathcal{S} = \int_{\Gamma_S} (\partial_t \phi) w_{\mathsf{h}} \mathrm{d}\mathcal{S} - \sum_{\mathcal{S}\in\Gamma_S} \int_{\partial\mathcal{S}} n_{\mathcal{S},t} (\hat{\phi} - \phi^-) w^- \mathrm{d}(\partial\mathcal{S}) \tag{4.49}$$

with $\hat{\phi}$ the numerical flux in time for the velocity potential ϕ. The numerical fluxes $\hat{\eta}$ and $\hat{\phi}$ are defined as

$$\hat{\phi} := \begin{cases} \phi^+ & \text{on } \partial\mathcal{S}(t_{n-1}^-), \\ \phi^- & \text{on } \partial\mathcal{S}\backslash\partial\mathcal{S}(t_{n-1}^-), \end{cases} \text{ and } \hat{\eta} := \begin{cases} \eta^+ & \text{on } \partial\mathcal{S}(t_{n-1}^-), \\ \eta^- & \text{on } \partial\mathcal{S}\backslash\partial\mathcal{S}(t_{n-1}^-). \end{cases} \tag{4.50}$$

Finally, we introduce the bilinear form $B_{\mathsf{h}} : V_{\mathsf{h}} \times V_{\mathsf{h}} \mapsto \mathbb{R}$ as

$$\begin{aligned} B_{\mathsf{h}}(\phi_{\mathsf{h}}, v) := &\int_{\mathcal{E}_{\mathsf{h}}^n} \bar{\nabla}\phi_{\mathsf{h}} \cdot \bar{\nabla} v \, \mathrm{d}\mathcal{K} - \int_{\Gamma_{int}} [\![\phi]\!] \cdot \{\!\{\bar{\nabla} v\}\!\} \, \mathrm{d}\mathcal{S} - \int_{\Gamma_{int}} \{\!\{\bar{\nabla}\phi_{\mathsf{h}}\}\!\} \cdot [\![v]\!] \, \mathrm{d}\mathcal{S} \\ &+ \int_{\Gamma_{int}} n_{\mathcal{S}}\Big(\mathcal{R}_{\mathcal{S}}([\![\phi]\!]) \cdot [\![v]\!]\Big) \, \mathrm{d}\mathcal{S}, \end{aligned} \tag{4.51}$$

the linear form $L_{\mathsf{h}} : V_{\mathsf{h}} \mapsto \mathbb{R}$ as

$$L_{\mathsf{h}}(v) := \int_{\Gamma_N} g_N v \, \mathrm{d}\mathcal{S}, \tag{4.52}$$

and substitute (4.48), (4.49) and (4.50) into (4.46) and (4.47). Hence, we can state the space-time discontinuous Galerkin weak formulation for linear free surface water waves as the following:
Find a $\phi_{\mathsf{h}} \in V_{\mathsf{h}}$ *and* $\eta_{\mathsf{h}} \in W_{\mathsf{h}}$ *such that for all* $v_{\mathsf{h}} \in V_{\mathsf{h}}$ *and* $w_{\mathsf{h}} \in W_{\mathsf{h}}$

$$\begin{aligned} B_{\mathsf{h}}(\phi_{\mathsf{h}}, v_{\mathsf{h}}) - \Big(\partial_t \eta_{\mathsf{h}}, v_{\mathsf{h}}\Big)_{\Gamma_S} - \Big(\eta^- - \eta^+, v^-\Big)_{\Gamma_S(t_{n-1}^-)} &= L_{\mathsf{h}}(v_{\mathsf{h}}) \\ \Big(\partial_t \phi_{\mathsf{h}}, w_{\mathsf{h}}\Big)_{\Gamma_S} + \Big(g\eta_{\mathsf{h}}, w_{\mathsf{h}}\Big)_{\Gamma_S} + \Big(\phi^- - \phi^+, w^-\Big)_{\Gamma_S(t_{n-1}^-)} &= 0 \end{aligned} \tag{4.53}$$

is satisfied with $\Gamma_S(t_{n-1}^-) = \bigcup \partial\mathcal{S}(t_{n-1}^-)$ *and* $(u, v)_{\Gamma_S} := \int_{\Gamma_S} u \, v \, \mathrm{d}\mathcal{S}$.

4.4.2 Space-time discontinuous Galerkin discretization

To obtain the space-time DG discretization, we first discretize the local lifting operator $\mathcal{R}_{\mathcal{S},\mathsf{k}}([\![\phi]\!])$ per space-time element $\mathcal{K}_{\mathsf{k}}^n$. This is done by expanding the local lifting operator $\mathcal{R}_{\mathcal{S},\mathsf{k}}([\![\phi]\!])$ as

$$(\mathcal{R}_{\mathcal{S},\mathsf{k}}([\![\phi]\!]))_k = \sum_{j=1}^{n_p} \hat{R}_{k,j}^{\mathcal{S},\mathsf{k}} \psi_{\mathsf{k},j} \tag{4.54}$$

and choosing the test function τ_{h} in (4.30) as $\psi_{\mathsf{k},\mathsf{i}}$, to get

$$\sum_{j=1}^{n_p} \hat{R}_{k,j}^{\mathcal{S},\mathsf{k}} \int_{\mathcal{K}_{\mathsf{k}}^n} \psi_{\mathsf{k},j}\psi_{\mathsf{k},i}\,\mathrm{d}\mathcal{K} = \frac{1}{2}\sum_{j=1}^{n_p}\Big(\hat{\phi}_{\mathsf{l},j}\int_{\mathcal{S}} n_k^{\mathsf{l}}\psi_{\mathsf{l},j}\psi_{\mathsf{k},i}\,\mathrm{d}\mathcal{S} + \hat{\phi}_{\mathsf{r},j}\int_{\mathcal{S}} n_k^{\mathsf{r}}\psi_{\mathsf{r},j}\psi_{\mathsf{k},i}\,\mathrm{d}\mathcal{S}\Big), \tag{4.55}$$

for each face $\mathcal{S} \in \Gamma_{int} \cap \partial\mathcal{K}_{\mathsf{k}}^n$, where the $\psi_{\mathsf{k},j}$'s are the basis functions and $\hat{R}_{k,j}^{\mathcal{S},\mathsf{k}}$ the expansion coefficients for each component of $\mathcal{R}_{\mathcal{S},\mathsf{k}}([\![\phi]\!])_k$ with $k = 1, 2, 3$.

The space-time finite element discretization is obtained by substituting the polynomial expansions for the velocity potential ϕ_{h}, the free surface height η_{h} and the local lifting operator $\mathcal{R}_{\mathcal{S},\mathsf{k}}([\![\phi]\!])$ in space-time discontinuous Galerkin weak formulation (4.53), and choosing the test functions v_{h} and w_{h} as $\psi_{\mathsf{k},i}$ and φ_i, respectively. The resulting space-time finite element discretization for (4.53) is given in (4.92), (4.93) and (4.94), which are presented in the Appendix 4.8.1. Subsequently, we obtain a linear system of algebraic equations by eliminating $\hat{R}_{k,j}^{\mathcal{S},\mathsf{k}}$ and $\hat{\eta}_{\mathsf{l},j}^n$ using the relations (4.55) and (4.94) into (4.92) and (4.93), and combining them.

With the help of the notations (4.95) introduced in Appendix 4.8.1, the expansion coefficients of local lifting opertor $\mathcal{R}_{\mathcal{S},\mathsf{k}}$ for each face $\mathcal{S}$ can be expressed in terms of the expansion coefficients of the velocity potential ϕ_{h} using (4.55) as

$$\hat{R}_k^{\mathcal{S},\mathsf{k}} = \frac{1}{2}(A^{\mathcal{K},\mathsf{k}})^{-1}\big(D_k^{\mathcal{S},\mathsf{lk}}\,\hat{\phi}_{\mathsf{l}} + D_k^{\mathcal{S},\mathsf{rk}}\,\hat{\phi}_{\mathsf{r}}\big). \tag{4.56}$$

Similarly, we can relate the expansion coefficients $\hat{\eta}_{\mathsf{l}}^n$ and $\hat{\phi}_{\mathsf{l}}^n$ using (4.94) as

$$\hat{\eta}_{\mathsf{l}}^n = -[(H^{\mathcal{S}})^{-1}]_{n_q\times n_q}\Big([G^{\mathcal{S}}]_{n_q\times n_p}\hat{\phi}_{\mathsf{l}}^n - [F^{\mathcal{S},\phi}]_{n_q\times 1}\Big). \tag{4.57}$$

Substituting (4.92) and (4.93) in the first equation of the (4.53), rearranging some terms, and eliminating $\hat{\eta}^n$ and $\hat{R}_k^{\mathcal{S},\mathsf{k}}$ using the algebraic relations (4.56) and (4.57); we obtain the following linear algebraic system

$$\mathcal{L}\Phi^n = \mathcal{X} \tag{4.58}$$

with $\mathcal{L}$ the global matrix, Φ^n the unknown expansion coefficients of velocity potential and $\mathcal{X}$ the right hand side. The global matrix $\mathcal{L}$ is defined as

$$\begin{aligned}\mathcal{L} := &\sum_{\mathcal{K}} B^{\mathsf{kk}} + \sum_{\mathcal{S}\in\Gamma_S} [\bar{G}^{\mathcal{S}}]_{n_p\times n_q}[(H^{\mathcal{S}})^{-1}]_{n_q\times n_q}[G^{\mathcal{S}}]_{n_q\times n_p} \\ &\sum_{\mathcal{S}\in\Gamma_{int}} -\frac{1}{2}\big(C^{\mathsf{ll},\mathcal{S}} + (C^{\mathsf{ll},\mathcal{S}})^T + \frac{n_{\mathcal{S}}}{4}M_{ij}^{ll} - \frac{1}{2}\big(C^{\mathsf{lr},\mathcal{S}} + (C^{\mathsf{rl},\mathcal{S}})^T + \frac{n_{\mathcal{S}}}{4}M_{ij}^{lr} \\ &- \frac{1}{2}\big(C^{\mathsf{rl},\mathcal{S}} + (C^{\mathsf{lr},\mathcal{S}})^T + \frac{n_{\mathcal{S}}}{4}M_{ij}^{rl} - \frac{1}{2}\big(C^{\mathsf{rr},\mathcal{S}} + (C^{\mathsf{rr},\mathcal{S}})^T + \frac{n_{\mathcal{S}}}{4}M_{ij}^{rr}\end{aligned} \tag{4.59}$$

and the right hand side

$$\mathcal{X} = \sum_{\mathcal{S}\in\Gamma_L} E^{\mathcal{S},\mathsf{l}} + \sum_{\mathcal{S}\in\Gamma_S} (-F^{\mathcal{S},\eta} + [\bar{G}^{\mathcal{S}}]_{n_p\times n_q}[(H^{\mathcal{S}})^{-1}]_{n_q\times n_q}[F^{\mathcal{S},\phi}]_{n_q\times 1}) \tag{4.60}$$

Given $\hat{\phi}^{n-1}$ and $\hat{\eta}^{n-1}$, we can construct the linear system $\mathcal{L}\Phi^n = \mathcal{X}$ and solve for Φ^n. Subsequently, we obtain $\hat{\eta}^n$ using (4.57).

4.5 Space-time variational (dis)continuous Galerkin method

4.5.1 Variational formulation

For the discrete variational formulation of linear free surface waves, we introduce the horizontal cross section of the computational flow domain Ω_{h} as $\bar{\Omega}_{\mathsf{h}}(z)$. Now, we define the total discrete kinetic energy $E_{K_{\mathsf{h}}}$ and the total discrete potential energy $E_{P_{\mathsf{h}}}$ in each space-time slab $\mathcal{E}_{\mathsf{h}}^n$ as

$$E_{K_{\mathsf{h}}} = \int_{\mathcal{E}_{\mathsf{h}}^n} \frac{1}{2}|\mathbf{u}_{\mathsf{h}}|^2 \,\mathrm{d}\mathcal{K} - \int_{\Gamma_L} g_N\phi_{\mathsf{h}} \,\mathrm{d}\mathcal{S} \text{ and } E_{P_{\mathsf{h}}} \quad = \int_{\Gamma_S} \frac{1}{2} g\eta_{\mathsf{h}}^2 \,\mathrm{d}\mathcal{S}, \tag{4.61}$$

where

$$\int_{\mathcal{E}_{\mathsf{h}}^n} \mathrm{d}\mathcal{K} = \int_{t_{n-1}}^{t_n}\int_{-H}^{0}\int_{\bar{\Omega}_{\mathsf{h}}} \mathrm{d}x\mathrm{d}y\mathrm{d}z\mathrm{d}t \text{ and } \int_{\Gamma_S} \mathrm{d}\mathcal{S} = \int_{t_{n-1}}^{t_n}\int_{\bar{\Omega}_{\mathsf{h}}(z=0)} \mathrm{d}x\mathrm{d}y\mathrm{d}t$$

In (4.61), we directly introduce the relation $\mathbf{u}_\mathsf{h} = \bar{\nabla}\phi_\mathsf{h} + \mathcal{R}(\llbracket\hat{\phi} - \phi_\mathsf{h}\rrbracket)$ obtained from the primal relation (4.39). The use of the global lifting operator, however, does not result into a discretization with a compact stencil. We therefore redefine the first term of the kinetic energy in (4.61) using local lifting operators as

$$E_{K_\mathsf{h}} = \int_{\mathcal{E}_\mathsf{h}^n} \frac{1}{2n_S} \left(\sum_{\mathcal{S}\subset\partial\mathcal{K}_\mathsf{k}^n} \left(\bar{\nabla}\phi_\mathsf{h} + n_S \mathcal{R}_{\mathcal{S},\mathsf{k}}(\llbracket\hat{\phi} - \phi_\mathsf{h}\rrbracket) \right)^2 \right) \mathrm{d}\mathcal{K} - \int_{\Gamma_L} g_N \phi_\mathsf{h} \mathrm{d}\mathcal{S} \tag{4.62}$$

with n_S the number of faces of each space-time element $\mathcal{K}_\mathsf{k}^n$. The discrete kinetic energy (4.62) is further expanded as

$$\begin{aligned} E_{K_\mathsf{h}} = &\int_{\mathcal{E}_\mathsf{h}^n} \frac{1}{2} |\bar{\nabla}\phi_\mathsf{h}|^2 \, \mathrm{d}\mathcal{K} + \int_{\mathcal{E}_\mathsf{h}^n} \sum_{\mathcal{S}\subset\partial\mathcal{K}_\mathsf{k}^n} \left(\bar{\nabla}\phi_\mathsf{h} \cdot \mathcal{R}_{\mathcal{S},\mathsf{k}}(\llbracket\hat{\phi} - \phi_\mathsf{h}\rrbracket) \right) \mathrm{d}\mathcal{K} + \\ &\int_{\mathcal{E}_\mathsf{h}^n} \frac{n_S}{2} \sum_{\mathcal{S}\subset\partial\mathcal{K}_\mathsf{k}^n} |\mathcal{R}_{\mathcal{S},\mathsf{k}}(\llbracket\hat{\phi} - \phi_\mathsf{h}\rrbracket)|^2 \, \mathrm{d}\mathcal{K} - \int_{\Gamma_L} g_N \phi_\mathsf{h} \, \mathrm{d}\mathcal{S}, \end{aligned} \tag{4.63}$$

where $\int_{\Gamma_L} \mathrm{d}\mathcal{S} = \int_{t_{n-1}}^{t_n} \int_{\partial\Omega_L} \mathrm{d}l\mathrm{d}z\mathrm{d}t$ with l the horizontal coordinate of the boundary $\partial\Omega_L$. Finally, we define the discrete functional for linear free surfaces as

$$\mathcal{L}_\mathsf{h}(\phi_\mathsf{h}, \phi_{\mathsf{h},s}, \eta_\mathsf{h}) = \int_{\Gamma_S} \phi_{\mathsf{h},s}(\partial_t \eta_\mathsf{h}) \, \mathrm{d}\mathcal{S} - (E_{K_\mathsf{h}} + E_{P_\mathsf{h}}). \tag{4.64}$$

To obtain the discrete variational formulation for the linear free surface waves, we now state the discrete Luke's variational principle as

$$\delta\mathcal{L}_\mathsf{h}(\phi_\mathsf{h}, \phi_{\mathsf{h},s}, \eta_\mathsf{h}) = 0, \tag{4.65}$$

where $\phi_{\mathsf{h},s} = \phi_\mathsf{h}(t, x, y, z = 0)$ is the approximated velocity potential evaluated at the mean free surface and $\delta\mathcal{L}_\mathsf{h}$ is the variational derivative defined as

$$\delta\mathcal{L}_\mathsf{h} = \lim_{\epsilon\to 0} \frac{1}{\epsilon} \Big(\mathcal{L}_\mathsf{h}(\phi_\mathsf{h} + \epsilon\delta\phi_\mathsf{h}, \phi_{\mathsf{h},s} + \epsilon\delta\phi_{\mathsf{h},s}, \eta_\mathsf{h} + \epsilon\delta\eta_\mathsf{h}) - \mathcal{L}_\mathsf{h}((\phi_\mathsf{h}, \phi_{\mathsf{h},s}, \eta_\mathsf{h}) \Big) \tag{4.66}$$

with $\delta\phi_{\mathsf{h}}$, $\delta\phi_{\mathsf{h},s}$ and $\delta\eta_{\mathsf{h}}$ the arbitrary variations.

Applying Luke's variational principle (4.65), and using (4.66) and the relation

$$\mathcal{R}_{\mathcal{S},\mathsf{k}}([\![\hat{\phi}-\phi_{\mathsf{h}}+\epsilon(\delta\hat{\phi}-\delta\phi_{\mathsf{h}})]\!])=\mathcal{R}_{\mathcal{S},\mathsf{k}}([\![\hat{\phi}-\phi_{\mathsf{h}}]\!])+\epsilon\mathcal{R}_{\mathcal{S},\mathsf{k}}([\![\delta\hat{\phi}-\delta\phi_{\mathsf{h}}]\!]), \tag{4.67}$$

we get

$$\begin{aligned}
&\int_{\Gamma_S}\big(\phi_{\mathsf{h},s}\partial_t(\delta\eta_{\mathsf{h}})-g\eta_{\mathsf{h}}\delta\eta_{\mathsf{h}}+(\partial_t\eta_{\mathsf{h}})\delta\phi_{\mathsf{h},s}\big)\mathrm{d}\mathcal{S}-\int_{\mathcal{E}_{\mathsf{h}}^n}\bar{\nabla}\phi_{\mathsf{h}}\cdot\bar{\nabla}(\delta\phi_{\mathsf{h}})\,\mathrm{d}\mathcal{K}\\
&-\int_{\mathcal{E}_{\mathsf{h}}^n}\sum_{\mathcal{S}\subset\partial\mathcal{K}_{\mathsf{k}}^n}\Big(\bar{\nabla}\phi_{\mathsf{h}}\cdot\mathcal{R}_{\mathcal{S},\mathsf{k}}([\![\delta\hat{\phi}-\delta\phi_{\mathsf{h}}]\!])+\bar{\nabla}(\delta\phi_{\mathsf{h}})\cdot\mathcal{R}_{\mathcal{S},\mathsf{k}}([\![\hat{\phi}-\phi_{\mathsf{h}}]\!])\Big)\,\mathrm{d}\mathcal{K}\\
&-\int_{\mathcal{E}_{\mathsf{h}}^n}\sum_{\mathcal{S}\subset\partial\mathcal{K}_{\mathsf{k}}^n}n_S\Big(\mathcal{R}_{\mathcal{S},\mathsf{k}}([\![\hat{\phi}-\phi_{\mathsf{h}}]\!])\cdot\mathcal{R}_{\mathcal{S},\mathsf{k}}([\![\delta\hat{\phi}-\delta\phi_{\mathsf{h}}]\!])\Big)\mathrm{d}\mathcal{K}\\
&+\int_{\Gamma_L}g_N\delta\phi_{\mathsf{h}}\,\mathrm{d}\mathcal{S}=0
\end{aligned}\tag{4.68}$$

with $\delta\phi_{\mathsf{h}}$, $\delta\phi_{s,\mathsf{h}}$ and $\delta\eta_{\mathsf{h}}$ the arbitrary variations.

From a computational point of view, the local lifting operators are easier to compute on the faces of an element rather than on the element itself. So, we first rearrange the sum over elements in (4.68) into a sum over faces and use the fact that the local lifting operators are only non-zero in the elements connected to the face $\mathcal{S}$, to obtain

$$\begin{aligned}
&\int_{\Gamma_S}\big(\phi_{\mathsf{h},s}\partial_t(\delta\eta_{\mathsf{h}})-g\eta_{\mathsf{h}}\delta\eta_{\mathsf{h}}+(\partial_t\eta_{\mathsf{h}})\delta\phi_{\mathsf{h},s}\big)\mathrm{d}\mathcal{S}\\
&+\int_{\Gamma_L}g_N\delta\phi_{\mathsf{h}}\,\mathrm{d}\mathcal{S}-\int_{\mathcal{E}_{\mathsf{h}}^n}\bar{\nabla}\phi_{\mathsf{h}}\cdot\bar{\nabla}(\delta\phi_{\mathsf{h}})\,\mathrm{d}\mathcal{K}\\
&-\sum_{\mathcal{S}\in\Gamma_{int}}\Bigg(\int_{\mathcal{K}_{\mathsf{l}}^n}\Big(\bar{\nabla}\phi_{\mathsf{h}}\cdot\mathcal{R}_{\mathcal{S},\mathsf{l}}([\![\delta\hat{\phi}-\delta\phi_{\mathsf{h}}]\!])+\bar{\nabla}(\delta\phi_{\mathsf{h}})\cdot\mathcal{R}_{\mathcal{S},\mathsf{l}}([\![\hat{\phi}-\phi_{\mathsf{h}}]\!])\Big)\,\mathrm{d}\mathcal{K}\\
&\qquad+\int_{\mathcal{K}_{\mathsf{r}}^n}\Big(\bar{\nabla}\phi_{\mathsf{h}}\cdot\mathcal{R}_{\mathcal{S},\mathsf{r}}([\![\delta\hat{\phi}-\delta\phi_{\mathsf{h}}]\!])+\bar{\nabla}(\delta\phi_{\mathsf{h}})\cdot\mathcal{R}_{\mathcal{S},\mathsf{r}}([\![\hat{\phi}-\phi_{\mathsf{h}}]\!])\Big)\,\mathrm{d}\mathcal{K}\Bigg)\\
&-\sum_{\mathcal{S}\in\Gamma_{int}}\Bigg(\int_{\mathcal{K}_{\mathsf{l}}^n}n_S\Big(\mathcal{R}_{\mathcal{S},\mathsf{l}}([\![\hat{\phi}-\phi_{\mathsf{h}}]\!])\cdot\mathcal{R}_{\mathcal{S},\mathsf{l}}([\![\delta\hat{\phi}-\delta\phi_{\mathsf{h}}]\!])\Big)\mathrm{d}\mathcal{K}
\end{aligned}$$

$$
\begin{aligned}
&+ \int_{\mathcal{K}_{\mathsf{r}}^n} n_S \Big(\mathcal{R}_{\mathcal{S},\mathsf{r}}([\![\hat{\phi} - \phi_{\mathsf{h}}]\!]) \cdot \mathcal{R}_{\mathcal{S},\mathsf{r}}([\![\delta\hat{\phi} - \delta\phi_{\mathsf{h}}]\!]) \Big) \mathrm{d}\mathcal{K} \Bigg) \\
&- \sum_{\mathcal{S}\in\Gamma_{bou}} \int_{\mathcal{K}_{\mathsf{l}}^n} \Big(\bar{\nabla}\phi_{\mathsf{h}} \cdot \mathcal{R}_{\mathcal{S},\mathsf{l}}([\![\delta\hat{\phi} - \delta\phi_{\mathsf{h}}]\!]) + \bar{\nabla}(\delta\phi_{\mathsf{h}}) \cdot \mathcal{R}_{\mathcal{S},\mathsf{l}}([\![\hat{\phi} - \phi_{\mathsf{h}}]\!]) \Big) \, \mathrm{d}\mathcal{K} \\
&- \sum_{\mathcal{S}\in\Gamma_{bou}} \int_{\mathcal{K}_{\mathsf{l}}^n} n_S \Big(\mathcal{R}_{\mathcal{S},\mathsf{l}}([\![\hat{\phi} - \phi_{\mathsf{h}}]\!]) \cdot \mathcal{R}_{\mathcal{S},\mathsf{l}}([\![\delta\hat{\phi} - \delta\phi_{\mathsf{h}}]\!]) \Big) \mathrm{d}\mathcal{K} = 0. \qquad (4.69)
\end{aligned}
$$

In (4.69), we define the numerical flux on the variations $\delta\phi_{\mathsf{h}}$ as

$$
\delta\hat{\phi} := \{\!\{\delta\phi_{\mathsf{h}}\}\!\} \text{ on } \mathcal{S} \in \Gamma_{int} \quad \text{and} \quad \delta\hat{\phi} := \delta\phi_{\mathsf{h}} \text{ on } \mathcal{S} \in \Gamma_{bou}, \qquad (4.70)
$$

which follows the definition of numerical flux for ϕ_{h} in (4.36). By using the definitions (4.36) and (4.70), and the properties in (4.24), we can deduce the following relations

$$
\begin{aligned}
&[\![\hat{\phi} - \phi_{\mathsf{h}}]\!] = -[\![\phi_{\mathsf{h}}]\!] \text{ on } \mathcal{S} \in \Gamma_{int}, && [\![\hat{\phi} - \phi_{\mathsf{h}}]\!] = 0 \text{ on } \mathcal{S} \in \Gamma_{bou}, \\
&[\![\delta\hat{\phi} - \delta\phi_{\mathsf{h}}]\!] = -[\![\delta\phi_{\mathsf{h}}]\!] \text{ on } \mathcal{S} \in \Gamma_{int} \quad \text{and} && [\![\delta\hat{\phi} - \delta\phi_{\mathsf{h}}]\!] = 0 \text{ on } \mathcal{S} \in \Gamma_{bou}.
\end{aligned} \qquad (4.71)
$$

We now simplify (4.69) using (4.71) to obtain

$$
\begin{aligned}
&\int_{\Gamma_S} \big(\phi_{\mathsf{h},s} \partial_t(\delta\eta_{\mathsf{h}}) - g\eta_{\mathsf{h}}\delta\eta_{\mathsf{h}} + (\partial_t\eta_{\mathsf{h}})\delta\phi_{\mathsf{h},s} \big) \mathrm{d}\mathcal{S} \\
&+ \int_{\Gamma_L} g_N \delta\phi_{\mathsf{h}} \, \mathrm{d}\mathcal{S} - \int_{\mathcal{E}_{\mathsf{h}}^n} \bar{\nabla}\phi_{\mathsf{h}} \cdot \bar{\nabla}(\delta\phi_{\mathsf{h}}) \, \mathrm{d}\mathcal{K} \\
&+ \sum_{\mathcal{S}\in\Gamma_{int}} \Bigg(\int_{\mathcal{K}_{\mathsf{l}}^n} \Big(\bar{\nabla}\phi_{\mathsf{h}} \cdot \mathcal{R}_{\mathcal{S},\mathsf{l}}([\![\delta\phi_{\mathsf{h}}]\!]) + \bar{\nabla}(\delta\phi_{\mathsf{h}}) \cdot \mathcal{R}_{\mathcal{S},\mathsf{l}}([\![\phi_{\mathsf{h}}]\!]) \Big) \, \mathrm{d}\mathcal{K} \\
&+ \int_{\mathcal{K}_{\mathsf{r}}^n} \Big(\bar{\nabla}\phi_{\mathsf{h}} \cdot \mathcal{R}_{\mathcal{S},\mathsf{r}}([\![\delta\phi_{\mathsf{h}}]\!]) + \bar{\nabla}(\delta\phi_{\mathsf{h}}) \cdot \mathcal{R}_{\mathcal{S},\mathsf{r}}([\![\phi_{\mathsf{h}}]\!]) \Big) \, \mathrm{d}\mathcal{K} \Bigg) \\
&- \sum_{\mathcal{S}\in\Gamma_{int}} \Bigg(\int_{\mathcal{K}_{\mathsf{l}}^n} n_S \Big(\mathcal{R}_{\mathcal{S},\mathsf{l}}([\![\phi_{\mathsf{h}}]\!]) \cdot \mathcal{R}_{\mathcal{S},\mathsf{l}}([\![\delta\phi_{\mathsf{h}}]\!]) \Big) \mathrm{d}\mathcal{K} \\
&+ \int_{\mathcal{K}_{\mathsf{r}}^n} n_S \Big(\mathcal{R}_{\mathcal{S},\mathsf{r}}([\![\phi_{\mathsf{h}}]\!]) \cdot \mathcal{R}_{\mathcal{S},\mathsf{r}}([\![\delta\phi_{\mathsf{h}}]\!]) \Big) \mathrm{d}\mathcal{K} \Bigg) = 0. \qquad (4.72)
\end{aligned}
$$

Finally, using the definition of average in (4.21), the definition of the local lifting operator (4.26) and the arbitrariness of variations, we obtain the discrete variational formulation of the linear free surface waves as

Find a $\bar{\phi}_{\mathsf{h}}^n \in \bar{V}_{\mathsf{h}}$ *and* $\bar{\eta}_{\mathsf{h}}^n \in \bar{W}_{\mathsf{h}}$ *such that for all* $\delta\bar{\phi}_{\mathsf{h}}^n \in \bar{V}_{\mathsf{h}}$ *and* $\delta\bar{\eta}_{\mathsf{h}}^n \in \bar{W}_{\mathsf{h}}$*, the equations*

$$\int_{\mathcal{E}_{\mathsf{h}}^n} \bar{\nabla}\phi_{\mathsf{h}} \cdot \bar{\nabla}(\delta\phi_{\mathsf{h}}) \, \mathrm{d}\mathcal{K} - \sum_{\mathcal{S}\in\Gamma_{int}} \int_{\mathcal{S}} \Big(\{\!\{\bar{\nabla}\phi_{\mathsf{h}}\}\!\} \cdot [\![\delta\phi_{\mathsf{h}}]\!] + \{\!\{\bar{\nabla}(\delta\phi_{\mathsf{h}})\}\!\} \cdot [\![\phi_{\mathsf{h}}]\!] - n_S \{\!\{\mathcal{R}_{\mathcal{S}}([\![\phi_{\mathsf{h}}]\!])\}\!\} \cdot [\![\delta\phi_{\mathsf{h}}]\!] \Big) \, \mathrm{d}\mathcal{S} - \int_{\Gamma_L} g_N \delta\phi_{\mathsf{h}} \, \mathrm{d}\mathcal{S} - \int_{\Gamma_S} (\partial_t \eta_{\mathsf{h}}) \delta\phi_{\mathsf{h},s} \, \mathrm{d}\mathcal{S} = 0 \tag{4.73}$$

and

$$\int_{\Gamma_S} \big(\phi_{\mathsf{h},s} \partial_t(\delta\eta_{\mathsf{h}}) - g\eta_{\mathsf{h}}\delta\eta_{\mathsf{h}} \big) \mathrm{d}\mathcal{S} = 0 \tag{4.74}$$

are satisfied with the end point conditions on the variations as $\delta\phi_{\mathsf{h}}(t_{n-1}) = \delta\eta_{\mathsf{h}}(t_{n-1}) = \delta\phi_{\mathsf{h}}(t_n) = \delta\eta_{\mathsf{h}}(t_n) = 0$*, where the approximations* ϕ_{h} *and* η_{h} *are defined as in (4.19).* To satisfy these end point conditions on the variations, we define the expansions of variations

$$\delta\phi_{\mathsf{h}} = \psi^n \psi^{n-1} \delta\bar{\phi}_{\mathsf{h}}^n \quad \text{and} \quad \delta\bar{\eta}_{\mathsf{h}} = \psi^n \psi^{n-1} \delta\bar{\eta}_{\mathsf{h}}^n \tag{4.75}$$

such that they vanish at t_n and t_{n-1} but are non-zero within the space-time element. In addition, we use the approximations defined in (4.19) for ϕ_{h} and η_{h}. These are coupled with the previous space-time domain $\mathcal{E}_{\mathsf{h}}^{n-1}$ by imposing the continuity in time. While the variables are a piecewise continuous linear approximation in time between the two time levels, the variations are forced to be zero at the end points and are thus defined differently. The basis and test functions are therefore unequal. For the harmonic oscillator, such a choice of continuous approximation for variables and vanishing test functions at the end points in each time interval leads to the modified mid-point scheme, which is energy-conserving.

4.5.2 Variational finite element discretization

To obtain the variational finite element discretization, we first have to discretize the local lifting operators $\mathcal{R}_{\mathcal{S},\mathsf{k}}([\![\phi_{\mathsf{h}}]\!])$ per space-time element $\mathcal{K}_{\mathsf{k}}^n$.

Using a similar approximation as given in (4.19) for ϕ_{h}, the local lifting operator $\mathcal{R}_{\mathcal{S},\mathsf{k}}([\![\phi_{\mathsf{h}}]\!])$ is expanded as

$$\mathcal{R}_{\mathcal{S},\mathsf{k}}([\![\phi_{\mathsf{h}}]\!]) = \bar{\mathcal{R}}^{n}_{\mathcal{S},\mathsf{k}}([\![\phi_{\mathsf{h}}]\!])\psi^{n} + \bar{\mathcal{R}}^{n-1}_{\mathcal{S},\mathsf{k}}([\![\phi_{\mathsf{h}}]\!])\psi^{n-1}. \tag{4.76}$$

with $\bar{\mathcal{R}}^{n}_{\mathcal{S},\mathsf{k}}([\![\phi_{\mathsf{h}}]\!])$ the local lifting operator on the spatial element K^{n}_{k}. Thereafter, we define the expansion of the local lifting operator $\bar{\mathcal{R}}^{n}_{\mathcal{S},\mathsf{k}}([\![\phi_{\mathsf{h}}]\!])$ akin to (4.54) as

$$(\bar{\mathcal{R}}^{n}_{\mathcal{S},\mathsf{k}}([\![\phi_{\mathsf{h}}]\!]))_{k} = \sum_{j=1}^{n_p} \hat{R}^{\mathcal{S},\mathsf{k}n}_{k,j}\bar{\psi}_{\mathsf{k},j} \tag{4.77}$$

with $\hat{R}^{\mathcal{S},\mathsf{k}n}_{k,j}$ the expansion coefficients for each component of $\bar{\mathcal{R}}^{n}_{\mathcal{S},\mathsf{k}}([\![\phi_{\mathsf{h}}]\!])_{k}$ with $k = 1, 2, 3$. The discretization of the local lifting operator $\bar{\mathcal{R}}^{n}_{\mathcal{S},\mathsf{k}}([\![\phi_{\mathsf{h}}]\!])$ arises from (4.30) as

$$\sum_{j=1}^{n_p} \hat{R}^{\mathcal{S},\mathsf{k}n}_{k,j} \int_{\mathcal{K}^{n}_{\mathsf{k}}} \bar{\psi}_{\mathsf{k},j}\bar{\psi}_{\mathsf{k},i}\,\mathrm{d}K = \frac{1}{2}\sum_{j=1}^{n_p}\Big(\hat{\phi}^{n}_{\mathsf{l},j}\int_{\mathcal{S}} \bar{n}^{\mathsf{l}}_{k}\bar{\psi}_{\mathsf{l},j}\bar{\psi}_{\mathsf{k},i}\,\mathrm{d}\mathcal{S} + \hat{\phi}^{n}_{\mathsf{r},j}\int_{\mathcal{S}} \bar{n}^{\mathsf{r}}_{k}\bar{\psi}_{\mathsf{r},j}\bar{\psi}_{\mathsf{k},i}\,\mathrm{d}\mathcal{S}\Big) \tag{4.78}$$

for $\mathcal{S} \in \Gamma_{int} \cap \partial\mathcal{K}^{n}_{\mathsf{k}}$ with $\bar{\psi}_{\mathsf{k},j}$ the basis function.

The space-time variational finite element discretization can now be obtained by substituting the polynomial expansion for the velocity potential ϕ_{h}, the free surface height η_{h} and the local lifting operator $\mathcal{R}_{\mathcal{S},\mathsf{k}}([\![\phi]\!])$ in the variational formulation (4.73) and (4.74), and using the arbitrariness of the variations $\delta\bar{\phi}^{n}_{\mathsf{h}}$, $\delta\bar{\phi}_{s,\mathsf{h}}$ and $\delta\bar{\eta}_{\mathsf{h}}$. The variations $\delta\phi_{\mathsf{h}}$ are varied as $\psi^{n}\psi^{n-1}\bar{\psi}_{\mathsf{k},i}$ for $i = 1, \ldots, n_p$, and $\delta\eta_{\mathsf{h}}$ as $\psi^{n}\psi^{n-1}\bar{\varphi}_{\mathsf{l},i}$ for $i = 1, \ldots, n_q$ such that they vanish at t_n and t_{n-1}. Further, to simplify the finite element discretization we use the fact that the basis functions ψ^{n} and ψ^{n-1} are independent of space, the basis functions $\bar{\psi}_{\mathsf{k},i}$ and $\bar{\varphi}_{\mathsf{l},i}$ are independent of time, and the spatial element K_{k} does not deform in time to get the following simplifications:

$$\partial_t\bar{\psi}_{\mathsf{k},i} = 0, \quad \partial_t\bar{\varphi}_{\mathsf{l},i} = 0, \quad \bar{\nabla}\psi^{n} = 0 \quad \text{and} \quad \bar{\nabla}\psi^{n-1} = 0. \tag{4.79}$$

The resulting finite element discretization for the variational formulation (4.73) and (4.74) are given in (4.96) and (4.97), which are presented in

the Appendix 4.8.2. Subsequently, we obtain a linear system of algebraic equations by eliminating $\hat{R}_{k,j}^{\mathcal{S},\mathsf{k}n}\ \hat{\eta}_{\mathsf{l},j}^{n}$ using the relations (4.78) and (4.97) into (4.96).

With the help of the notations (4.98) introduced in Appendix 4.8.2, the expansion coefficients of local lifting opertor $\mathcal{R}_{\mathcal{S},\mathsf{k}}^{n}$ for each face $\mathcal{S}$ can be expressed in terms of the expansion coefficients of the velocity potential ϕ_{h}^{n} using (4.77) as

$$\hat{R}_{k}^{\mathcal{S},\mathsf{k}n} = \frac{1}{2}(A^{\mathcal{K},\mathsf{k}})^{-1}\big(\hat{D}_{k}^{\mathcal{S},\mathsf{lk}}\ \hat{\phi}_{\mathsf{l}}^{n} + \hat{D}_{k}^{\mathcal{S},\mathsf{rk}}\ \hat{\phi}_{\mathsf{r}}^{n}\big). \tag{4.80}$$

Similarly, we can relate the expansion coefficients $\hat{\eta}_{\mathsf{l}}^{n}$ and $\hat{\phi}_{\mathsf{l}}^{n}$ using (4.97) with (4.98) as

$$\hat{\eta}_{\mathsf{l}}^{n} = (H^{\mathcal{S}})^{-1}\big(L^{\mathcal{S}}\hat{\phi}_{\mathsf{l}}^{n} + \bar{L}^{\mathcal{S}}\hat{\phi}_{\mathsf{l}}^{n-1} - \bar{H}^{\mathcal{S}}\hat{\eta}_{\mathsf{l}}^{n-1}\big). \tag{4.81}$$

Eliminating $\hat{\eta}^{n}$, $\hat{R}_{k}^{\mathcal{S},\mathsf{k}n}$ and $\hat{R}_{k}^{\mathcal{S},\mathsf{k}(n-1)}$ from (4.96) using (4.81) and (4.80), we obtain the following linear algebraic system

$$\mathcal{L}\Phi^{n} = \mathcal{X} \tag{4.82}$$

with $\mathcal{L}$ the global matrix, Φ^{n} the unknown expansion coefficients of the velocity potential, and $\mathcal{X}$ the right hand side. The global matrix $\mathcal{L}$ is defined as

$$\begin{aligned}\mathcal{L} = &\sum_{\mathcal{K}} B^{\mathsf{kk}} - \sum_{\mathcal{S}\in\Gamma_S} G^{\mathcal{S}}(H^{\mathcal{S}})^{-1}L^{\mathcal{S}} \\ &\sum_{\mathcal{S}\in\Gamma_{int}} -\frac{1}{2}\big(C^{\mathsf{ll},\mathcal{S}} + (C^{\mathsf{ll},\mathcal{S}})^{T}\big) + \frac{n_{\mathcal{S}}}{4}M_{ij}^{ll} - \frac{1}{2}\big(C^{\mathsf{lr},\mathcal{S}} + (C^{\mathsf{rl},\mathcal{S}})^{T}\big) + \frac{n_{\mathcal{S}}}{4}M_{ij}^{lr} \\ &- \frac{1}{2}\big(C^{\mathsf{rl},\mathcal{S}} + (C^{\mathsf{lr},\mathcal{S}})^{T}\big) + \frac{n_{\mathcal{S}}}{4}M_{ij}^{rl} - \frac{1}{2}\big(C^{\mathsf{rr},\mathcal{S}} + (C^{\mathsf{rr},\mathcal{S}})^{T}\big) + \frac{n_{\mathcal{S}}}{4}M_{ij}^{rr},\end{aligned} \tag{4.83}$$

and the right hand side $\mathcal{X}$ as

$$\begin{aligned}\mathcal{X} = &-\sum_{\mathcal{K}} \bar{B}^{\mathsf{kk}}\hat{\phi}_{\mathsf{k}}^{n-1} + \sum_{\mathcal{S}\in\Gamma_L} E^{\mathcal{S},\mathsf{l}} \\ &+ \sum_{\mathcal{S}\in\Gamma_S} G^{\mathcal{S}}(H^{\mathcal{S}})^{-1}\bar{L}^{\mathcal{S}}\hat{\phi}_{\mathsf{l}}^{n-1} + \Big(\bar{G}^{\mathcal{S}} - G^{\mathcal{S}}(H^{\mathcal{S}})^{-1}\bar{H}^{\mathcal{S}}\Big)\hat{\eta}_{\mathsf{l}}^{n-1}\end{aligned}$$

$$
\begin{aligned}
&+ \sum_{\mathcal{S}\in\Gamma_{int}} \Big(\frac{1}{2}\big(\bar{C}^{\mathsf{ll},\mathcal{S}} + \bar{C}^{\mathsf{ll},\mathcal{S}})^T\big) - \frac{n_{\mathcal{S}}}{4}\bar{M}_{ij}^{ll}\Big)\hat{\phi}_{\mathsf{l}}^{n-1} + \\
&\qquad \Big(\frac{1}{2}\big(\bar{C}^{\mathsf{lr},\mathcal{S}} + (\bar{C}^{\mathsf{rl},\mathcal{S}})^T\big) - \frac{n_{\mathcal{S}}}{4}\bar{M}_{ij}^{lr}\Big)\hat{\phi}_{\mathsf{r}}^{n-1} + \\
&\qquad \Big(\frac{1}{2}\big(\bar{C}^{\mathsf{rl},\mathcal{S}} + (\bar{C}^{\mathsf{lr},\mathcal{S}})^T\big) - \frac{n_{\mathcal{S}}}{4}\bar{M}_{ij}^{rl}\Big)\hat{\phi}_{\mathsf{l}}^{n-1} + \\
&\qquad \Big(\frac{1}{2}\big(\bar{C}^{\mathsf{rr},\mathcal{S}} + (\bar{C}^{\mathsf{rr},\mathcal{S}})^T\big) - \frac{n_{\mathcal{S}}}{4}\bar{M}_{ij}^{rr}\Big)\hat{\phi}_{\mathsf{r}}^{n-1}. \qquad (4.84)
\end{aligned}
$$

Given ϕ_{h}^{n-1} and η_{h}^{n-1}, we can construct the linear system $\mathcal{L}\Phi^n = \mathcal{X}$ and solve it for ϕ_{h}^n. Subsequently, we obtain η_{h}^n using (4.81).

4.5.3 Solving the linear systems (4.58) and (4.82)

The global matrix $\mathcal{L}$ of the linear algebraic system has size $N_e n_p \times N_e n_p$, where N_e is the number of elements in the computational domain $\mathcal{E}_{\mathsf{h}}^n$ and n_p the number of degrees of freedom per element. It can be divided into $N_e \times N_e$ blocks with size $n_p \times n_p$. Further, the number of non-zero block rows in the global matrix $\mathcal{L}$ w.r.t each space-time element $\mathcal{K}_{\mathsf{k}}^n$ is directly dependent on its immediate neighbouring elements connected through the boundary of $\partial\mathcal{K}_{\mathsf{k}}^n$. Therefore, the global matrix $\mathcal{L}$ is of block sparse type with a compact stencil. Hence, we use a well-tested software tool kit called PETSc (see [52, 53, 54]) for building and solving the linear system.

This tool kit PETSc, a "Portable, Extensible Toolkit for Scientific Computation", consists of a number of sparse matrix storage routines and both iterative and direct sparse linear solvers. In particular, we use a sequential block sparse matrix storage routine for building the global matrix $\mathcal{L}$ and a linear solver based on a biconjugate gradient method with ILU preconditioner for solving the linear system $\mathcal{L}\Phi^n = \mathcal{X}$ (see the manual by Satish et al. [52]). For building the matrices, PETSc offers a preallocated matrix storage routine for which we have to specify the number of non zero blocks in each row of the matrix. We have observed a tremendous increase of performance by choosing this particular option.

4.6 Numerical Results

In this section, we present the numerical results obtained using the standard space-time DG and the variational space-time (dis)continuous Galerkin finite element schemes, and compare the numerical results with two exact solutions of the linear wave equations. The numerical implementation is done for the equations in non-dimensional form. We used the following scaling:

$$(x, y, z) \mapsto H\,(x, y, z), \quad t \mapsto \sqrt{\frac{H}{g}}\,t, \quad \phi \mapsto H\sqrt{gH}\,\phi \text{ and } \eta \mapsto H\,\eta. \tag{4.85}$$

For the sake of testing the space-time DG finite element scheme, we also consider some exact solutions of the Laplace and Poisson equations. We compute the $L^2(\Omega_{\mathsf{h}})$–norms of the errors in numerical results for the velocity potential and free surface height as

$$\|\phi - \phi_{\mathsf{h}}\|_{L^2(\Omega_{\mathsf{h}})} := \Big(\sum_{\mathcal{K}} \int_{\mathcal{K}_{\mathsf{k}}^n} (\phi - \phi_{\mathsf{h}})^2 \,\mathrm{d}\mathcal{K}\Big)^{1/2} \text{ and} \tag{4.86}$$

$$\|\eta - \eta_{\mathsf{h}}\|_{L^2(\Gamma_S(t_n^-))} := \Big(\sum_{\mathcal{S}\in\Gamma_S} \int_{\partial\mathcal{S}(t_n^-)} (\eta - \eta_{\mathsf{h}})^2 \,\mathrm{d}(\partial\mathcal{S})\Big)^{1/2}, \tag{4.87}$$

where (ϕ, η) and $(\phi_{\mathsf{h}}, \eta_{\mathsf{h}})$ are the exact and numerical solutions of the velocity potential and free surface wave height, respectively. The order of accuracy of the numerical scheme can be determined using

$$\mathsf{order} = \Big(\ln(\mathsf{Error}^{(1)}) - \ln(\mathsf{Error}^{(2)})\Big) / \Big(\ln(\mathsf{h}_{\mathcal{K}}^{(1)}) - \ln(\mathsf{h}_{\mathcal{K}}^{(2)})\Big), \tag{4.88}$$

where $\mathsf{Error}^{(1)}$ and $\mathsf{Error}^{(2)}$ are the errors computed on the meshes with cell measures $\mathsf{h}_{\mathcal{K}}^{(1)}$ and $\mathsf{h}_{\mathcal{K}}^{(2)}$, respectively. For all wave simulations, the computational grid size in the z-direction is chosen such that it decreases as we move from the free surface at $z = 0$ down to the bottom topography. This is in line with the harmonic solution in which the amplitude decreases expenentially going from the rest level at $z = 0$.

4.6.1 Poisson equation

Consider the Poisson equation $\bar{\nabla}^2\phi = S$ on $\Omega = [0,1]^3$ which satisfies the exact solution $\phi(\bar{\mathbf{x}}) = 1 + \sin(2\pi x)\sin(2\pi y)\sin(2\pi z)$ with source term $S = 12\pi^2 \sin(2\pi x)\sin(2\pi y)\sin(2\pi z)$ and boundary condition $\phi = 1$ on $\partial\Omega$.

In the space-time DG scheme, we exclude the free surface and include the source terms to solve the Poisson equation numerically. Figure (4.3) (a) and (b) shows a plot of the numerical solution ϕ_h and a plot of the difference between exact and numerical solutions, respectively, on a grid of size $16 \times 16 \times 16$ at $z = 0.25$. We also compute the L^2–error for various grid sizes and plot the results on a log-log scale as shown in Fig. (4.4). The results show that the numerical scheme is second order accurate in space for linear polynomials.

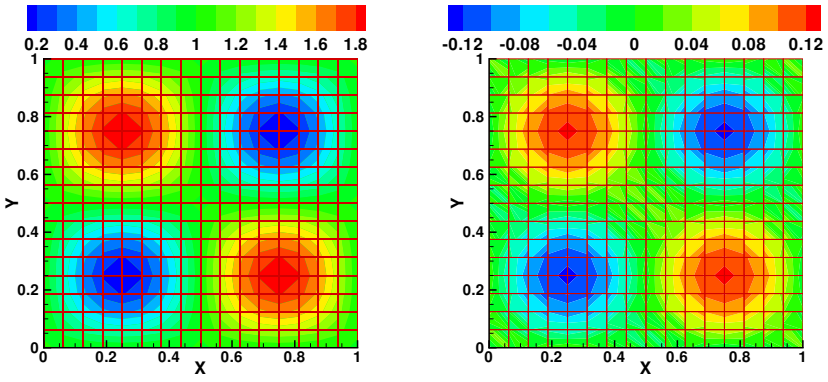

(a) Numerical solution ϕ_h. (b) Numerical error $\phi - \phi_\mathsf{h}$.

Figure 4.3: Contour plots of (a) the numerical solution ϕ_h and (b) the numerical error $\phi - \phi_\mathsf{h}$ at $z = 0.25$. The numerical solution is computed using a grid of size $16 \times 16 \times 16$ with the space-time DG scheme.

4.6.2 Laplace equation

Consider the Laplace equation $\bar{\nabla}^2\phi = 0$ on $\Omega = [0,1]^3$ which is satisfied by the exact solution $\phi = A\cos(k_x x + k_y y)\cosh(k_z z)$ with $k_z^2 = k_x^2 + k_y^2$, $k_x = 2\pi$, $k_y = 2\pi$, $A = 1$ the amplitude, periodic boundary conditions in

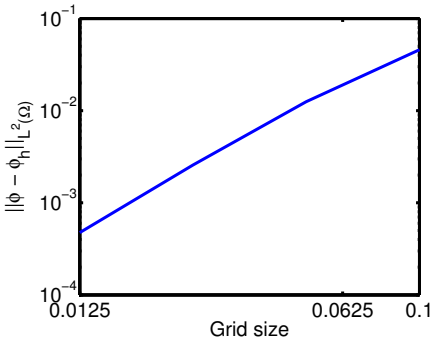

Figure 4.4: L^2–error versus grid size on a log-log scale. L^2–errors are computed on grids of size $8\times8\times8$, $16\times16\times16$, $32\times32\times32$ and $64\times64\times64$ with the space-time DG scheme.

the $x-$ and $y-$ directions, and Neumann boundary conditions $\partial_z\phi = 0$ at $z = 0$ and $\partial_z\phi = A\cos(k_x x + k_y y)\sinh(k_z)$ at $z = 1$.

We numerically solve the Laplace equation on various grids of size $N_x \times N_y \times N_z$ with N_x, N_y and N_z the number of elements in all three coordinate directions. In Tables 4.1 and 4.2, we present the errors of ϕ_h in the L^2–norm and the order of accuracy of the numerical scheme.

4.6.3 Harmonic waves

The governing equations for the linear free surface waves in (4.8) satisfy harmonic wave modes which are obtained as

$$\phi(x, y, z, t) = A_{l,m}\cos(k_x x + k_y y + \omega t)\cosh(k_z(z + H)) \tag{4.89}$$

on $\Omega = [0, 1]^2 \times [-H, 0]$, where $A_{l,m}$ is the amplitude; H the mean water depth; $k_x = 2\pi l$, $k_y = 2\pi m$, and $k_z = \pm\sqrt{k_x^2 + k_y^2}$ are the wave numbers; l and m are integers; ω the frequency and the dispersion relation is $\omega^2 = k_z \tanh(k_z H)$. The free surface evolution of the harmonic wave modes is obtained by using the kinematic free surface boundary condition $\partial_t\phi = g\eta$ as

$$\eta(x, y, t) = -A_{l,m}\omega\sin(k_x x + k_y y + \omega t)\cosh(k_z H) \text{ at } z = 0. \tag{4.90}$$

Table 4.1: L^2–errors of ϕ_{h} in the solution of the Laplace equation computed on regular grids (space-time DG scheme).

Grid $N_x \times N_y \times N_z$	Cell size h	Regular grid L^2–error	order
$8 \times 8 \times 2$	0.785155	$2.5342 \cdot 10^{-04}$	–
$16 \times 16 \times 4$	0.465848	$8.9136 \cdot 10^{-05}$	2.00
$32 \times 32 \times 8$	0.252864	$2.3569 \cdot 10^{-05}$	2.18
$64 \times 64 \times 16$	0.131652	$5.9896 \cdot 10^{-06}$	2.10

Table 4.2: L^2–errors of ϕ_{h} in the solution of the Laplace equation computed on irregular grids (space-time DG scheme).

Grid $N_x \times N_y \times N_z$	Cell size h	Irregular grid L^2–error	order
$8 \times 8 \times 2$	0.795757	$2.5429 \cdot 10^{-04}$	–
$16 \times 16 \times 4$	0.470324	$9.0512 \cdot 10^{-05}$	1.96
$32 \times 32 \times 8$	0.255019	$2.5272 \cdot 10^{-05}$	2.08
$64 \times 64 \times 16$	0.132687	$7.7551 \cdot 10^{-06}$	1.81

In both the space-time DG and space-time variational schemes, we initialize two harmonic modes with mean water depth $H = 1$, $(l, m) = (1, 1)$ and $(1, -1)$, and amplitudes $A_{1,1} = 2.32 \cdot 10^{-04}$ and $A_{1,-1} = 1.12 \cdot 10^{-04}$. The two modes have a time period $T = 2.1078$ and travel in diagonally opposite directions. The projections of the initial condition for the velocity potential and the free surface wave height are shown in Figs. 4.5(a) and (b). To test the space-time discontinuous Galerkin scheme and space-time

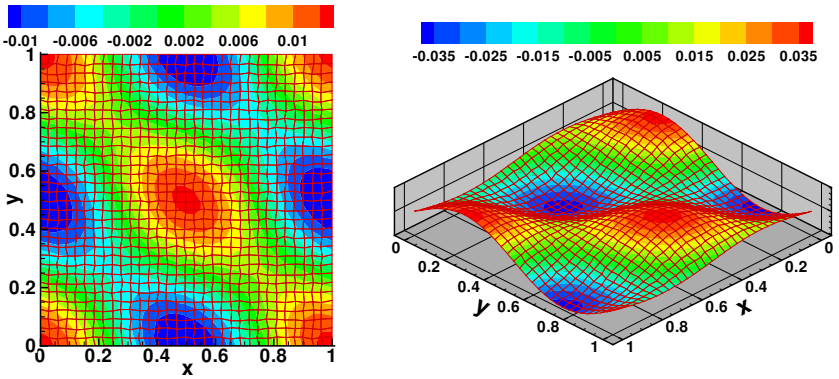

(a) Velocity potential. (b) Free surface wave height.

Figure 4.5: Contour plots of the velocity potential and the free surface wave height at time $t = 0$ on an irregular grid of size $32 \times 32 \times 8$.

variational scheme for accuracy, we simulated these harmonic waves for one time period T on various grids of sizes $8 \times 8 \times 2$, $16 \times 16 \times 2$, $32 \times 32 \times 4$ and $64 \times 64 \times 8$ with time steps $\Delta t = T/10$, $T/20$, $T/40$ and $T/80$, respectively. We also compute the errors of the velocity potential and free surface wave height in the L^2–norm and subsequently, determine the order of accuracy which are presented in Tables. 4.3 and 4.4. The contour plots of the velocity potential and free surface wave height of the numerical simulations from both schemes are presented in Figs. 4.6 and 4.7. To qualitatively show the dispersion error and dissipation error of the space-time DG scheme and space-time variational scheme, we have simulated the harmonic waves for about 10 time periods. We observe from the Figs. 4.8(a)-(j) that amplitude of the waves decay when simulated with the space-time DG scheme and does not decay in the space-time variational scheme.

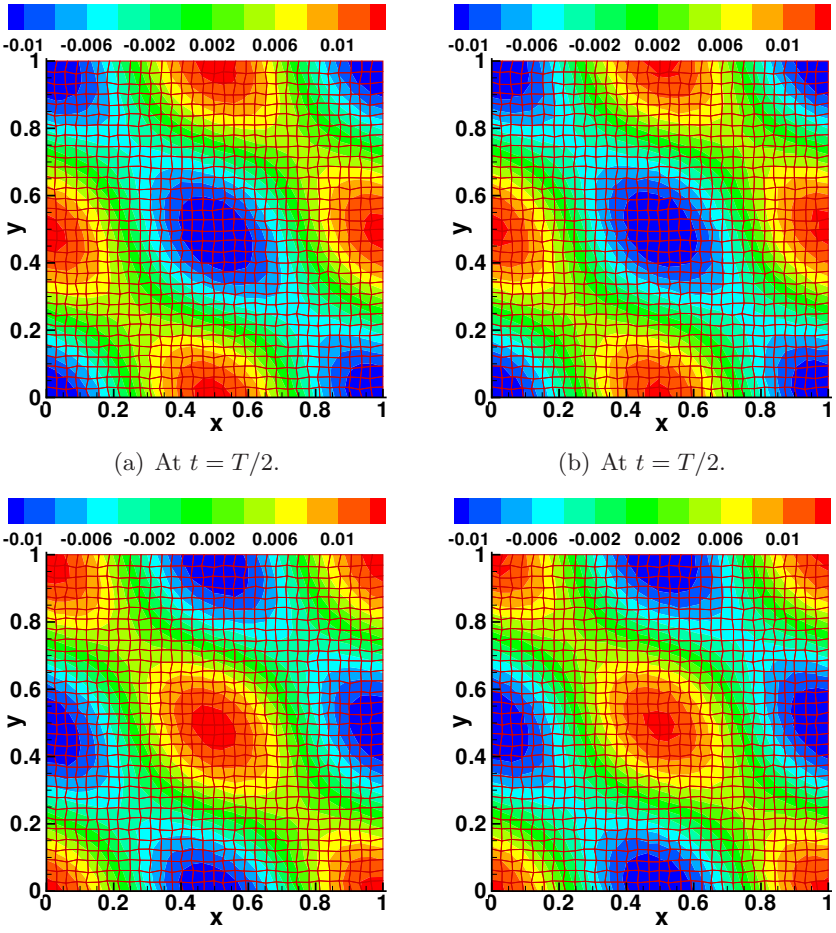

(a) At $t = T/2$.

(b) At $t = T/2$.

(c) At $t = T$.

(d) At $t = T$.

Figure 4.6: Contour plots of the velocity potential on the mean free surface obtained with the space-time variational scheme (left) and the space-time DG scheme (right). These results are obtained on an irregular grid of size $32 \times 32 \times 8$ with time step $\Delta t = T/40$, where T is the time period of the harmonic waves.

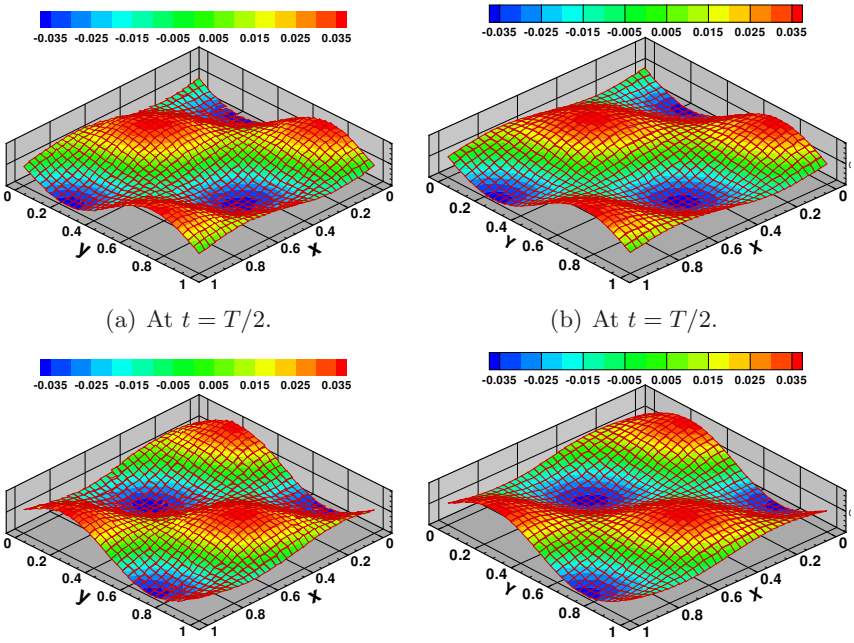

(a) At $t = T/2$. (b) At $t = T/2$.

(c) At $t = T$. (d) At $t = T$.

Figure 4.7: Contour plots of the free surface wave height obtained with the space-time variational scheme (left) and the space-time DG scheme (right). These results are obtained on an irregular grid of size $32 \times 32 \times 8$ with time step $\Delta t = T/40$, where T is the time period of the harmonic waves.

Table 4.3: L^2–errors of the velocity potential and the free surface height at $t = T$ on a regular grid using (space-time DG scheme).

Grid		Velocity potential		Free surface height	
$N_x \times N_y \times N_z$	h	L^2–error	order	L^2–error	order
$8 \times 8 \times 2$	0.785155	$9.0079 \cdot 10^{-04}$	–	$5.2950 \cdot 10^{-03}$	–
$16 \times 16 \times 4$	0.465848	$1.9761 \cdot 10^{-04}$	2.85	$1.4053 \cdot 10^{-03}$	2.54
$32 \times 32 \times 8$	0.252864	$4.9046 \cdot 10^{-05}$	2.29	$3.5070 \cdot 10^{-04}$	2.27
$64 \times 64 \times 16$	0.131652	$1.1961 \cdot 10^{-05}$	2.17	$8.7284 \cdot 10^{-05}$	2.13

Table 4.4: L^2–errors of the velocity potential and the free surface height at $t = T$ on a regular grid (space-time variational scheme).

Grid	Cell size	Velocity potential		Free surface height	
$N_x \times N_y \times N_z$	h	L^2–error	order	L^2–error	order
$8 \times 8 \times 2$	0.785155	$1.8445 \cdot 10^{-03}$	–	$2.3505 \cdot 10^{-02}$	–
$16 \times 16 \times 4$	0.465848	$6.1255 \cdot 10^{-04}$	2.11	$8.2809 \cdot 10^{-03}$	2.00
$32 \times 32 \times 8$	0.252864	$1.9072 \cdot 10^{-04}$	1.91	$2.4410 \cdot 10^{-03}$	2.00
$64 \times 64 \times 16$	0.131652	$4.9538 \cdot 10^{-05}$	2.07	$6.3329 \cdot 10^{-04}$	2.07

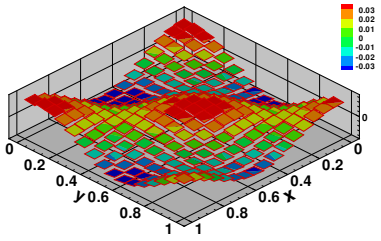

(a) At $t = T$.

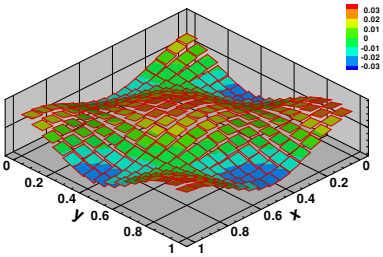

(b) At $t = T$.

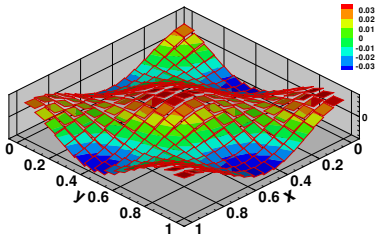

(c) At $t = 2T$.

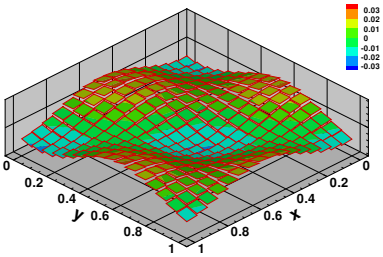

(d) At $t = 2T$.

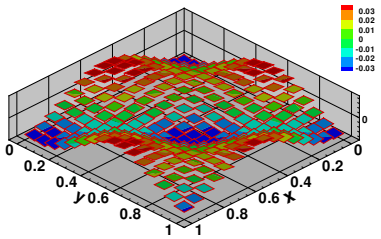

(e) At $t = 4T$.

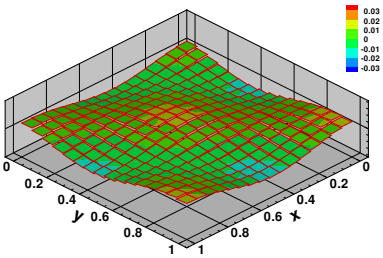

(f) At $t = 4T$.

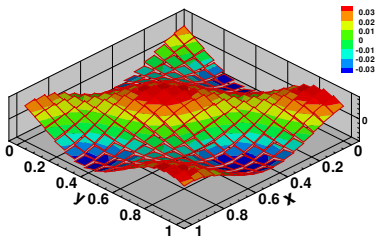

(g) At $t = 8T$

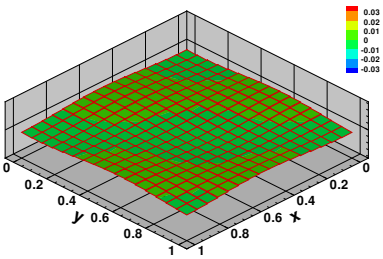

(h) At $t = 8T$

Figure 4.8: Contour plots of the free surface height obtained using space-time variational scheme (left) and space-time DG scheme (right). These results are obtained on an irregular grid of size $16 \times 16 \times 4$ with time step $\Delta t = T/10$, where T is the time period of the harmonic wave. Observe the decay of wave amplitude for space-time DG schems.

4.6.4 Linear waves generated by a wave maker

Consider a wave basin $\Omega = [0,1]^2 \times [-H, 0]$ with solid walls on all sides except a piston type wave maker on the side at $x = 1$. Given the normal velocity of the wave maker as $g_N = -Ak_x \cos(\omega t)\cos(k_y y)\cosh(k_z(z+H))$, we construct an exact solution for the velocity potential and free surface height as

$$\begin{aligned} \phi(t,x,y,z) &= A\cos(\omega t)\ \cos(k_x x)\cos(k_y y)\cosh(k_z(z+H)) \quad \text{and} \\ \eta(t,x,y) &= -A\omega\sin(\omega t)\ \cos(k_x x)\cos(k_y y)\cosh(k_z H) \end{aligned} \tag{4.91}$$

with A the wave amplitude, H the mean water depth, $k_x = (2l+1)\pi/2$, $k_y = 2m\pi$, $k_z^2 = (k_x^2 + k_y^2)$, ω the frequency satisfying the dispersion relation $\omega^2 = k_z \tanh(k_z H)$, and l and m are integers.

To simulate the waves generated by a wave maker, we initialize the flow field (η, ϕ) with the exact solution, prescribe the normal velocity of the wave maker at the boundary $x = 1$ and take the slip flow boundary conditions at the remaining solid wall boundaries. We set the parameters $H = 1$, $l = 0$, $m = 1$ and $A = 2.32 \cdot 10^{-04}$ and simulate the waves for one time period $T = 2\pi/\omega = 2.4763$ with time step $\Delta t = T/10$, $T/20$, $T/40$ and $T/80$ for computational grids of size $8 \times 8 \times 2$, $16 \times 16 \times 4$, $32 \times 32 \times 8$ and $64 \times 64 \times 16$. The simulations were again performed with both the space-time DG scheme and space-time variational scheme. The numerical results obtained are compared with the exact solutions and the errors in the L^2–norm are computed to verify the order of accuracy of both schemes. The errors in the L^2–norm and the orders of accuracy are presented in Tables 4.5 - 4.8 for both the velocity potential and the free surface height. The free surface waves generated by a wave maker are shown in Figs. 4.9(a)-(j) and 4.10(a)-(j) simulated with the space-time DG scheme and space-time variational scheme, respectively.

4.7 Concluding Remarks

A novel space-time variational (dis)continuous Galerkin method has been presented for the irrotational dynamics of linear free surface waves. It is based on a novel numerical discretization of Luke's variational principle. To achieve such a variational formulation, we derived a discrete functional

Table 4.5: L^2–errors of the velocity potential and the free surface height at $t = T$ on regular grids with the space-time DG scheme.

Grid $N_x \times N_y \times N_z$	Cell size h	Velocity potential L^2–error	order	Free surface height L^2–error	order
$8 \times 8 \times 2$	0.785155	$3.9801 \cdot 10^{-04}$	–	$5.0199 \cdot 10^{-03}$	–
$16 \times 16 \times 4$	0.465848	$7.4137 \cdot 10^{-05}$	3.22	$1.5546 \cdot 10^{-03}$	1.69
$32 \times 32 \times 8$	0.252864	$2.0123 \cdot 10^{-05}$	2.13	$3.9705 \cdot 10^{-04}$	1.97
$64 \times 64 \times 16$	0.131652	$5.3061 \cdot 10^{-06}$	2.04	$9.8416 \cdot 10^{-05}$	2.01

Table 4.6: L^2–errors of the velocity potential and the free surface height at $t = T$ on irregular grids with the space-time DG scheme.

Grid size $N_x \times N_y \times N_z$	Cell size h	Velocity potential L^2–error	order	Free surface height L^2–error	order
$8 \times 8 \times 2$	0.795757	$3.9649 \cdot 10^{-04}$	–	$4.9753 \cdot 10^{-03}$	–
$16 \times 16 \times 4$	0.470324	$7.5895 \cdot 10^{-05}$	3.14	$1.4990 \cdot 10^{-03}$	1.73
$32 \times 32 \times 8$	0.255019	$2.0966 \cdot 10^{-05}$	2.10	$3.0505 \cdot 10^{-04}$	2.30
$64 \times 64 \times 16$	0.132687	$5.3061 \cdot 10^{-06}$	2.08	$9.8416 \cdot 10^{-05}$	1.63

Table 4.7: L^2–errors of the velocity potential and the free surface height at $t = T$ on regular grids with the space-time variational scheme.

Grid	Cell size	Velocity potential		Free surface height	
$N_x \times N_y \times N_z$	h	L^2–error	order	L^2–error	order
$8 \times 8 \times 2$	0.785155	$3.9906 \cdot 10^{-04}$	–	$8.2652 \cdot 10^{-03}$	–
$16 \times 16 \times 4$	0.465848	$1.0063 \cdot 10^{-04}$	2.64	$3.4336 \cdot 10^{-03}$	1.27
$32 \times 32 \times 8$	0.252864	$2.1776 \cdot 10^{-05}$	2.51	$9.7198 \cdot 10^{-04}$	1.82
$64 \times 64 \times 16$	0.131652	$5.4312 \cdot 10^{-06}$	2.13	$2.4843 \cdot 10^{-04}$	1.97

Table 4.8: L^2–errors of the velocity potential and the free surface height at $t = T$ on irregular grids with the space-time variational scheme.

Grid	Cell size	Velocity potential		Free surface height	
$N_x \times N_y \times N_z$	h	L^2–error	order	L^2–error	order
$8 \times 8 \times 2$	0.795757	$4.0721 \cdot 10^{-04}$	–	$4.9753 \cdot 10^{-03}$	–
$16 \times 16 \times 4$	0.470324	$1.0595 \cdot 10^{-04}$	2.56	$1.4990 \cdot 10^{-03}$	1.64
$32 \times 32 \times 8$	0.255019	$2.3249 \cdot 10^{-05}$	2.48	$3.0505 \cdot 10^{-04}$	1.95
$64 \times 64 \times 16$	0.132687	$5.4312 \cdot 10^{-06}$	2.20	$9.8416 \cdot 10^{-05}$	2.22

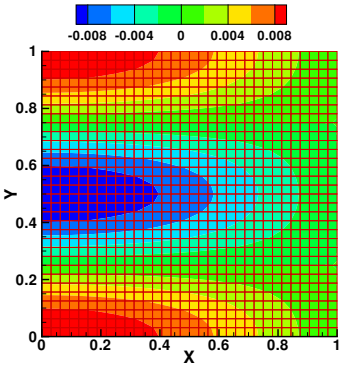

(a) At $t = 0$.

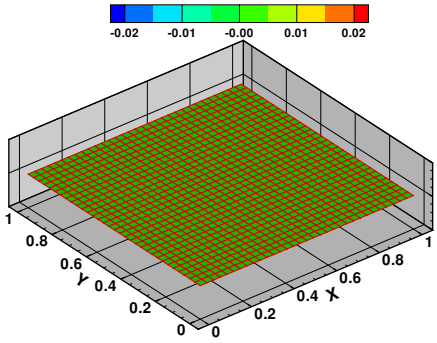

(b) At $t = 0$.

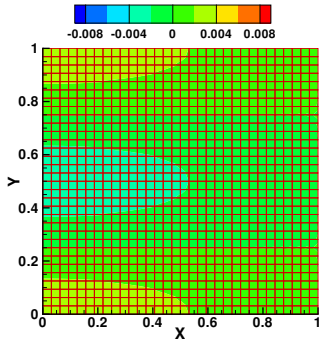

(c) At $t = 2T/5$.

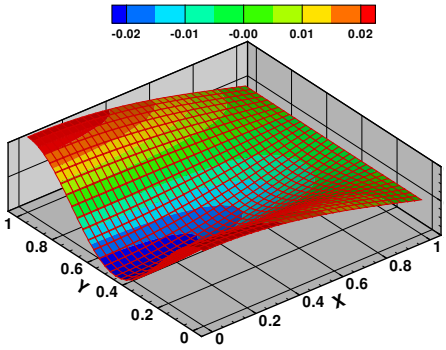

(d) At $t = 2T/5$.

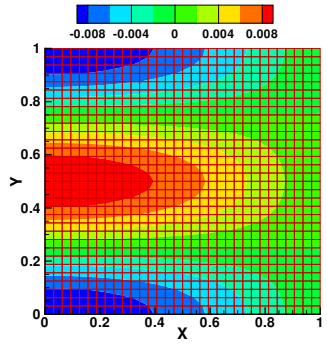

(e) At $t = T/2$.

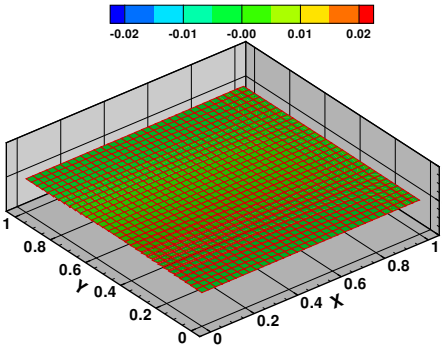

(f) At $t = T/2$.

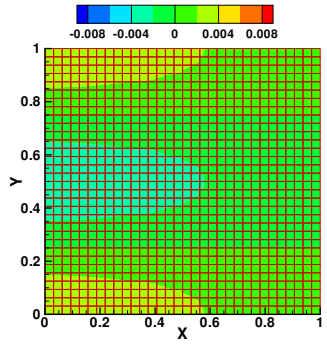

(g) At $t = 4T/5$.

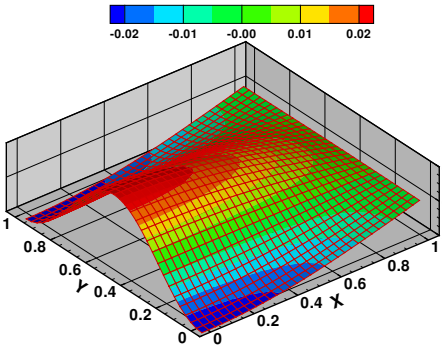

(h) At $t = 4T/5$.

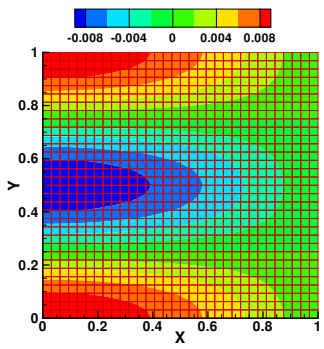

(i) At $t = T$.

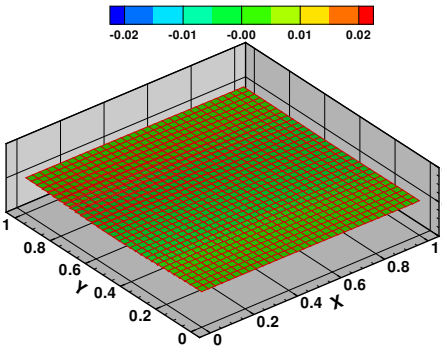

(j) At $t = T$.

Figure 4.9: Contour plots of the velocity potential ϕ_{h} at the mean free surface (left) and the free surface height η_{h} (right) on a regular grid of size $32 \times 32 \times 8$ (Space-time DG scheme).

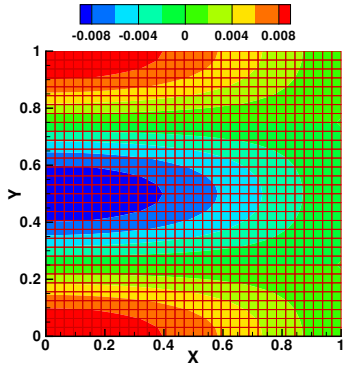

(a) At $t = 0$.

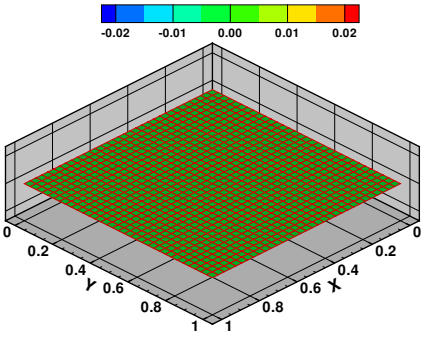

(b) At $t = 0$.

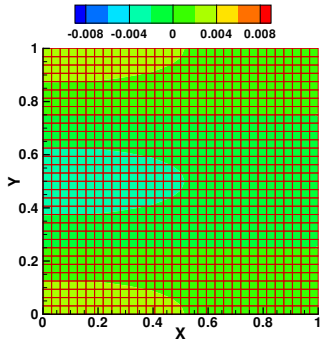

(c) At $t = 2T/5$.

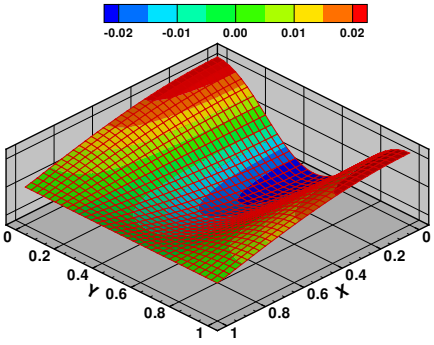

(d) At $t = 2T/5$.

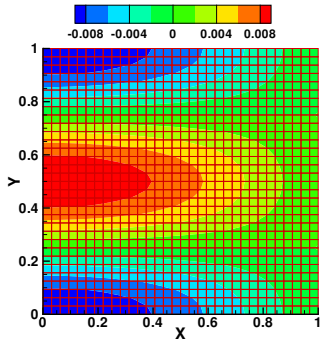

(e) At $t = T/2$.

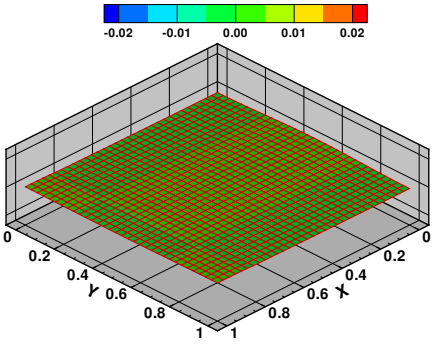

(f) At $t = T/2$.

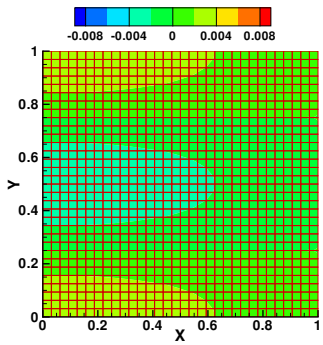

(g) At $t = 4T/5$.

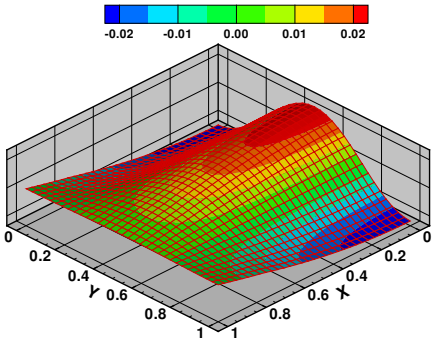

(h) At $t = 4T/5$.

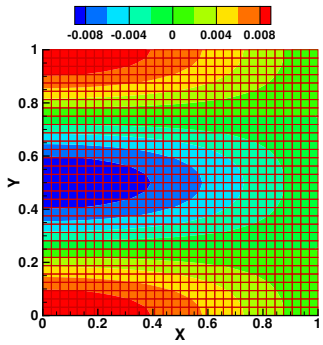

(i) At $t = T$.

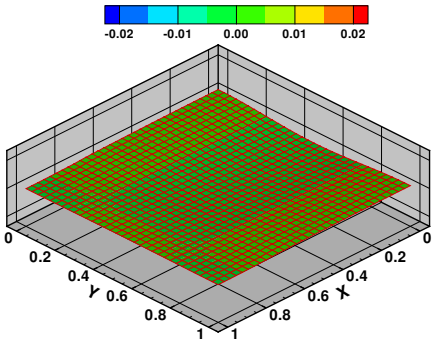

(j) At $t = T$.

Figure 4.10: Contour plots of the velocity potential ϕ_{h} at the mean free surface (left) and the free surface height η_{h} (right) on a regular grid of size $32 \times 32 \times 8$ (space-time variational scheme).

which is analogous to that of the continuum case for linear free surface waves. The variational discretization preserves the advantageous features of the space-time DG scheme such as the locality of the discretization. In addition, it ensured the resulting system to be symmetric leading to a speed-up in the computation, and conservation of energy and phase space.

For comparison, we considered the space-time DG of van der Vegt and Xu [65], extended with novel numerical tests in three space dimensions. The numerical discretization resulting from this method consists of linear systems of algebraic equations with a compact stencil. It also allowed us to use efficient sparse matrix storage routines and iterative linear solvers in the PETSc package. The PETSc package gave a good performance relative to other methods, such as direct solvers and locally build and optimized conjugate gradient solvers. We found that preallocation of memory for the matrix storage rather than a dynamic memory allocation improves the performance of the package. An extra advantage of PETSc is that the parallelization is a built-in feature.

The numerical results of the space-time DG and variational schemes have been compared with exact solutions of linear harmonic free surface waves in a periodic domain and linear waves generated by a wave maker. Both schemes show second order accurate results for a linear polynomial approximation of the wave field. Further, the space-time variational DG scheme does not show any decay in the amplitude of the waves whereas the space-time DG scheme shows significant amount of decay in the wave amplitude. However, the space-time variational DG finite element scheme shows a large dispersion error. We recommend, therefore, to extend the space-time variational (dis)continuous Galerkin scheme to nonlinear free surface waves. Further, investigate the time discretization in the space-time variational method to improve the dispersion accuracy while preserving the zero amplitude decay.

4.8 Appendix

4.8.1 Space-time DG discretization

In this Appendix, we present the space-time finite element discretization of the space-time discontinuous Galerkin weak formulation (4.53) by substituting the polynomial expansions for the velocity potential ϕ_{h}, the free

surface height η_{h} and the local lifting operator $\mathcal{R}_{\mathcal{S},\mathsf{k}}([\![\phi]\!])$ in (4.53), and choosing the test functions v_{h} and w_{h} as $\psi_{\mathsf{k},i}$ and $\varphi_{\mathsf{l},i}$, respectively.

First, we present the discretization of the bilinear form $B_{\mathsf{h}}(\phi_{\mathsf{h}}, v)$ in (4.53) is as follows:

$$\begin{aligned}
B_{\mathsf{h}}(\phi_{\mathsf{h}}, \psi_i) :=& \sum_{\mathsf{k}=1}^{N_e} \sum_{j=1}^{n_p} \hat{\phi}_{\mathsf{k},j} \int_{\mathcal{K}_{\mathsf{k}}^n} \bar{\nabla}\psi_{\mathsf{k},j} \cdot \bar{\nabla}\psi_{\mathsf{k},i} \,\mathrm{d}\mathcal{K} \\
&- \sum_{\mathcal{S}\in\Gamma_{int}} \sum_{j=1}^{n_p} \left(\frac{1}{2}\hat{\phi}_{\mathsf{l},j} \int_{\mathcal{S}} \psi_{\mathsf{l},j}(\bar{\mathbf{n}}^{\mathsf{l}} \cdot \bar{\nabla}\psi_{\mathsf{l},i} + \bar{\mathbf{n}}^{\mathsf{l}} \cdot \bar{\nabla}\psi_{\mathsf{r},i}) \,\mathrm{d}\mathcal{S} \right. \\
&\qquad \left. + \frac{1}{2}\hat{\phi}_{\mathsf{r},j} \int_{\mathcal{S}} \psi_{\mathsf{r},j}(\bar{\mathbf{n}}^{\mathsf{r}} \cdot \bar{\nabla}\psi_{\mathsf{l},i} + \bar{\mathbf{n}}^{\mathsf{r}} \cdot \bar{\nabla}\psi_{\mathsf{r},i}) \,\mathrm{d}\mathcal{S} \right) \\
&- \sum_{\mathcal{S}\in\Gamma_{int}} \sum_{j=1}^{n_p} \left(\frac{1}{2}\hat{\phi}_{\mathsf{l},j} \int_{\mathcal{S}} \left((\bar{\mathbf{n}}^{l} \cdot \bar{\nabla}\psi_{\mathsf{l},j})\psi_{\mathsf{l},i} + (\bar{\mathbf{n}}^{r} \cdot \bar{\nabla}\psi_{\mathsf{l},j})\psi_{\mathsf{r},i} \right) \mathrm{d}\mathcal{S} \right. \\
&\qquad \left. + \frac{1}{2}\hat{\phi}_{\mathsf{r},j} \int_{\mathcal{S}} \left((\bar{\mathbf{n}}^{l} \cdot \bar{\nabla}\psi_{\mathsf{r},j})\psi_{\mathsf{l},i} + (\bar{\mathbf{n}}^{r} \cdot \bar{\nabla}\psi_{\mathsf{r},j})\psi_{\mathsf{r},i} \right) \mathrm{d}\mathcal{S} \right) \\
&- \sum_{\mathcal{S}\in\Gamma_{int}} \sum_{j=1}^{n_p} \sum_{k=1}^{3} n_{\mathcal{S}} \left(\frac{1}{2}\hat{R}_{k,j}^{\mathcal{S},\mathsf{l}} \int_{\mathcal{S}} \left(n_k^{\mathsf{l}}\psi_{\mathsf{l},j}\psi_{\mathsf{l},i} + n_k^{\mathsf{r}}\psi_{\mathsf{l},j}\psi_{\mathsf{r},i} \right) \mathrm{d}\mathcal{S} \right. \\
&\qquad \left. + \frac{1}{2}\hat{R}_{k,j}^{\mathcal{S},\mathsf{r}} \int_{\mathcal{S}} \left(n_k^{\mathsf{l}}\psi_{\mathsf{r},j}\psi_{\mathsf{l},i} + n_k^{\mathsf{r}}\psi_{\mathsf{r},j}\psi_{\mathsf{r},i} \right) \mathrm{d}\mathcal{S} \right).
\end{aligned} \tag{4.92}$$

Second, the discretization of the linear form and the other free surface terms of the first equation in (4.53) is

$$\begin{aligned}
&L_{\mathsf{h}}(\psi_i) = \sum_{\mathcal{S}\in\Gamma_L} \int_{\mathcal{S}} g_N \psi_i \,\mathrm{d}\mathcal{S}, \quad \left(\partial_t \eta_{\mathsf{h}}, \psi_i\right)_{\Gamma_S} = \sum_{\mathcal{S}\in\Gamma_S} \sum_{j=1}^{n_q} \hat{\eta}_{\mathsf{l},j}^n \int_{\mathcal{S}} (\partial_t \varphi_{\mathsf{l},j})\psi_{\mathsf{l},i} \,\mathrm{d}\mathcal{S} \\
&\text{and } \left(\eta^- - \eta^+, \psi_i\right)_{\Gamma_S(t_{n-1}^-)} = \sum_{\mathcal{S}\in\Gamma_S} \sum_{j=1}^{n_q} \left(\hat{\eta}_{\mathsf{l},j}^n \int_{\partial\mathcal{S}(t_{n-1}^-)} \varphi_{\mathsf{l},j}\psi_{\mathsf{l},i} \,\mathrm{d}(\partial\mathcal{S}) \right. \\
&\qquad\qquad \left. - \hat{\eta}_{\mathsf{r},j}^{n-1} \int_{\partial\mathcal{S}(t_{n-1}^-)} \varphi_{\mathsf{l},j}\psi_{\mathsf{l},i} \,\mathrm{d}(\partial\mathcal{S}) \right).
\end{aligned} \tag{4.93}$$

Finally, the discretization of the second equation in (4.53) is given as

$$\sum_{\mathcal{S}\in\Gamma_S}\sum_{j=1}^{n_p}\Bigg(\phi_{\mathsf{l},j}^n\int_{\mathcal{S}}(\partial_t\psi_{\mathsf{l},j})\varphi_{\mathsf{l},i}\,\mathrm{d}\mathcal{S}+\hat{\phi}_{\mathsf{l},j}^n\int_{\partial\mathcal{S}(t_{n-1}^-)}\psi_{\mathsf{l},j}\varphi_{\mathsf{l},i}\,\mathrm{d}(\partial\mathcal{S})$$
$$-\hat{\phi}_{\mathsf{r},j}^{n-1}\int_{\partial\mathcal{S}(t_{n-1}^-)}\psi_{\mathsf{r},j}\varphi_{\mathsf{l},i}\,\mathrm{d}(\partial\mathcal{S})+\hat{\eta}_{\mathsf{l},j}^n\int_{\mathcal{S}}\varphi_{\mathsf{l},j}\varphi_{\mathsf{l},i}\,\mathrm{d}\mathcal{S}\Bigg)=0. \quad (4.94)$$

To obtain and describe the linear system of algebraic equations resulting from (4.92) to (4.94), we introduce and use the following matrix and vector notations:

$$A_{ij}^{\mathcal{K},\mathsf{k}}:=\int_{\mathcal{K}_\mathsf{k}}\psi_{\mathsf{k},i}\psi_{\mathsf{k},j}\mathrm{d}\mathcal{K},\qquad B_{ij}^{\mathcal{K},\mathsf{kk}}:=\int_{\mathcal{K}_\mathsf{k}}\bar{\nabla}\psi_{\mathsf{k},i}\cdot\bar{\nabla}\psi_{\mathsf{k},j}\mathrm{d}\mathcal{K},$$
$$C_{ij}^{\mathcal{S},\mathsf{lr}}:=\int_{\mathcal{S}}(\bar{\mathbf{n}}^{\mathsf{l}}\cdot\bar{\nabla}\psi_{\mathsf{l},i})\,\psi_{\mathsf{r},j}\mathrm{d}\mathcal{S},\qquad D_{k,ij}^{\mathcal{S},\mathsf{lr}}:=\int_{\mathcal{S}}n_k^{\mathsf{l}}\psi_{\mathsf{l},i}\psi_{\mathsf{r},j}\mathrm{d}\mathcal{S},$$
$$F_i^{\mathcal{S},\phi}:=\hat{\phi}_{\mathsf{r},j}^{n-1}\int_{\partial\mathcal{S}(t_{n-1}^-)}\psi_{\mathsf{r},j}\varphi_{\mathsf{l},i}\,\mathrm{d}(\partial\mathcal{S}),\qquad H_{ij}^{\mathcal{S}}:=\int_{\mathcal{S}}\varphi_{\mathsf{l},j}\varphi_{\mathsf{l},i}\,\mathrm{d}\mathcal{S},$$
$$F_i^{\mathcal{S},\eta}:=\hat{\eta}_{\mathsf{r},j}^{n-1}\int_{\partial\mathcal{S}(t_{n-1}^-)}\varphi_{\mathsf{r},j}\psi_{\mathsf{l},i}\,\mathrm{d}(\partial\mathcal{S}),\qquad E_i^{\mathcal{S},\mathsf{l}}:=\int_{\mathcal{S}_\mathsf{m}}g_N\psi_{\mathsf{l},i}\mathrm{d}\mathcal{S},$$
$$G_{ij}^{\mathcal{S}}:=\int_{\mathcal{S}}(\partial_t\psi_{\mathsf{l},j})\varphi_{\mathsf{l},i}\,\mathrm{d}\mathcal{S}+\int_{\partial\mathcal{S}(t_{n-1}^-)}\psi_{\mathsf{l},j}\varphi_{\mathsf{l},i}\,\mathrm{d}(\partial\mathcal{S}),$$
$$\bar{G}_{ij}^{\mathcal{S}}:=\int_{\mathcal{S}}(\partial_t\varphi_{\mathsf{l},j})\psi_{\mathsf{l},i}\,\mathrm{d}\mathcal{S}+\int_{\partial\mathcal{S}(t_{n-1}^-)}\varphi_{\mathsf{l},j}\psi_{\mathsf{l},i}\,\mathrm{d}(\partial\mathcal{S}),$$
$$M^{\mathsf{ll}}:=\sum_{k=1}^{3}\Big(D_k^{\mathcal{S},\mathsf{ll}}(A^{\mathcal{K},\mathsf{l}})^{-1}(D_k^{\mathcal{S},\mathsf{ll}})^T+D_k^{\mathcal{S},\mathsf{lr}}(A^{\mathcal{K},\mathsf{r}})^{-1}(D_k^{\mathcal{S},\mathsf{rl}})^T\Big),$$
$$M^{\mathsf{lr}}:=\sum_{k=1}^{3}\Big(D_k^{\mathcal{S},\mathsf{ll}}(A^{\mathcal{K},\mathsf{l}})^{-1}(D_k^{\mathcal{S},\mathsf{rl}})^T+D_k^{\mathcal{S},\mathsf{lr}}(A^{\mathcal{K},\mathsf{r}})^{-1}(D_k^{\mathcal{S},\mathsf{rr}})^T\Big),$$
$$M^{\mathsf{rl}}:=\sum_{k=1}^{3}\Big(D_k^{\mathcal{S},\mathsf{rl}}(A^{\mathcal{K},\mathsf{l}})^{-1}(D_k^{\mathcal{S},\mathsf{ll}})^T+D_k^{\mathcal{S},\mathsf{rr}}(A^{\mathcal{K},\mathsf{r}})^{-1}(D_k^{\mathcal{S},\mathsf{lr}})^T\Big),$$
$$M^{\mathsf{rr}}:=\sum_{k=1}^{3}\Big(D_k^{\mathcal{S},\mathsf{rl}}(A^{\mathcal{K},\mathsf{l}})^{-1}(D_k^{\mathcal{S},\mathsf{rl}})^T+D_k^{\mathcal{S},\mathsf{rr}}(A^{\mathcal{K},\mathsf{r}})^{-1}(D_k^{\mathcal{S},\mathsf{rr}})^T\Big). \quad (4.95)$$

4.8.2 Space-time variational discretization

In this Appendix, we present the space-time variational discretization of the variational formulation (4.73) and (4.74) by substituting the polynomial expansion of the velocity potential ϕ_{h}, the free surface height η_{h} and the local lifting operator $\mathcal{R}_{\mathcal{S},\mathsf{k}}([\![\phi]\!])$ (4.76) into the variational formulation (4.73) and (4.74), and choosing the arbitrariness of the variations $\delta\bar{\phi}^n_{\mathsf{h}}$ and $\delta\bar{\eta}_{\mathsf{h}}$ as $\psi^n\psi^{n-1}\bar{\psi}_{\mathsf{k},i}$ and $\psi^n\psi^{n-1}\bar{\varphi}_{\mathsf{l},i}$, respectively. Now, the space-time variational discretization of the variational formulation (4.73) using (4.79) is as follows:

$$
\begin{aligned}
&\sum_{\mathcal{K}}\sum_{j=1}^{n_p}\hat{\phi}^n_{\mathsf{k},j}\int_{\mathcal{K}^n_{\mathsf{k}}}(\psi^n_{\mathsf{k}})^2\psi^{n-1}_{\mathsf{k}}(\bar{\nabla}\bar{\psi}_{\mathsf{k},j}\cdot\bar{\nabla}\bar{\psi}_{\mathsf{k},i})\,\mathrm{d}\mathcal{K}+\\
&\sum_{\mathcal{K}}\sum_{j=1}^{n_p}\hat{\phi}^{n-1}_{\mathsf{k},j}\int_{\mathcal{K}^n_{\mathsf{k}}}\psi^n_{\mathsf{k}}(\psi^{n-1}_{\mathsf{k}})^2(\bar{\nabla}\bar{\psi}_{\mathsf{k},j}\cdot\bar{\nabla}\bar{\psi}_{\mathsf{k},i})\,\mathrm{d}\mathcal{K}\\
&-\sum_{\mathcal{S}\in\Gamma_{int}}\sum_{j=1}^{n_p}\Bigg(\frac{1}{2}\hat{\phi}^n_{\mathsf{l},j}\int_{\mathcal{S}}\psi^n_{\mathsf{l}}\bar{\psi}_{\mathsf{l},j}\Big(\psi^n_{\mathsf{l}}\psi^{n-1}_{\mathsf{l}}(\bar{\mathbf{n}}^{\mathsf{l}}\cdot\bar{\nabla}\bar{\psi}_{\mathsf{l},i})+\\
&\qquad\qquad\psi^n_{\mathsf{r}}\psi^{n-1}_{\mathsf{r}}(\bar{\mathbf{n}}^{\mathsf{l}}\cdot\bar{\nabla}\bar{\psi}_{\mathsf{r},i})\Big)\,\mathrm{d}\mathcal{S}\\
&\qquad+\frac{1}{2}\hat{\phi}^n_{\mathsf{r},j}\int_{\mathcal{S}}\psi^n_{\mathsf{r}}\bar{\psi}_{\mathsf{r},j}\big(\psi^n_{\mathsf{l}}\psi^{n-1}_{\mathsf{l}}(\bar{\mathbf{n}}^{\mathsf{r}}\cdot\bar{\nabla}\bar{\psi}_{\mathsf{l},i})+\\
&\qquad\qquad\psi^n_{\mathsf{r}}\psi^{n-1}_{\mathsf{r}}(\bar{\mathbf{n}}^{\mathsf{r}}\cdot\bar{\nabla}\bar{\psi}_{\mathsf{r},i})\big)\,\mathrm{d}\mathcal{S}\Bigg)\\
&-\sum_{\mathcal{S}\in\Gamma_{int}}\sum_{j=1}^{n_p}\Bigg(\frac{1}{2}\hat{\phi}^{n-1}_{\mathsf{l},j}\int_{\mathcal{S}}\psi^{n-1}_{\mathsf{l}}\bar{\psi}_{\mathsf{l},j}\Big(\psi^n_{\mathsf{l}}\psi^{n-1}_{\mathsf{l}}(\bar{\mathbf{n}}^{\mathsf{l}}\cdot\bar{\nabla}\bar{\psi}_{\mathsf{l},i})+\\
&\qquad\qquad\psi^n_{\mathsf{r}}\psi^{n-1}_{\mathsf{r}}(\bar{\mathbf{n}}^{\mathsf{l}}\cdot\bar{\nabla}\bar{\psi}_{\mathsf{r},i})\Big)\,\mathrm{d}\mathcal{S}\\
&\qquad+\frac{1}{2}\hat{\phi}^{n-1}_{\mathsf{r},j}\int_{\mathcal{S}}\psi^{n-1}_{\mathsf{r}}\bar{\psi}_{\mathsf{r},j}\big(\psi^n_{\mathsf{l}}\psi^{n-1}_{\mathsf{l}}(\bar{\mathbf{n}}^{\mathsf{r}}\cdot\bar{\nabla}\bar{\psi}_{\mathsf{l},i})+\\
&\qquad\qquad\psi^n_{\mathsf{r}}\psi^{n-1}_{\mathsf{r}}(\bar{\mathbf{n}}^{\mathsf{r}}\cdot\bar{\nabla}\bar{\psi}_{\mathsf{r},i})\big)\,\mathrm{d}\mathcal{S}\Bigg)\\
&-\sum_{\mathcal{S}\in\Gamma_{int}}\sum_{j=1}^{n_p}\Bigg(\frac{1}{2}\hat{\phi}^n_{\mathsf{l},j}\int_{\mathcal{S}}\psi^n_{\mathsf{l}}\Big(\psi^n_{\mathsf{l}}\psi^{n-1}_{\mathsf{l}}(\bar{\mathbf{n}}^{\mathsf{l}}\cdot\bar{\nabla}\bar{\psi}_{\mathsf{l},j})\bar{\psi}_{\mathsf{l},i}+
\end{aligned}
$$

$$\psi_{\mathsf{r}}^n \psi_{\mathsf{r}}^{n-1} (\bar{\mathbf{n}}^{\mathsf{r}} \cdot \bar{\nabla} \bar{\psi}_{\mathsf{l},j}) \bar{\psi}_{\mathsf{r},i} \Big) \, \mathrm{d}\mathcal{S}$$

$$+ \frac{1}{2} \hat{\phi}_{\mathsf{r},j}^n \int_{\mathcal{S}} \psi_{\mathsf{r}}^n \Big(\psi_{\mathsf{l}}^n \psi_{\mathsf{l}}^{n-1} (\bar{\mathbf{n}}^{\mathsf{l}} \cdot \bar{\nabla} \bar{\psi}_{\mathsf{r},j}) \bar{\psi}_{\mathsf{l},i} +$$

$$\psi_{\mathsf{r}}^n \psi_{\mathsf{r}}^{n-1} (\bar{\mathbf{n}}^{\mathsf{r}} \cdot \bar{\nabla} \bar{\psi}_{\mathsf{r},j}) \bar{\psi}_{\mathsf{r},i} \Big) \, \mathrm{d}\mathcal{S} \Bigg)$$

$$- \sum_{\mathcal{S} \in \Gamma_{int}} \sum_{j=1}^{n_p} \Bigg(\frac{1}{2} \hat{\phi}_{\mathsf{l},j}^{n-1} \int_{\mathcal{S}} \psi_{\mathsf{l}}^{n-1} \Big(\psi_{\mathsf{l}}^n \psi_{\mathsf{l}}^{n-1} (\bar{\mathbf{n}}^{\mathsf{l}} \cdot \bar{\nabla} \bar{\psi}_{\mathsf{l},j}) \bar{\psi}_{\mathsf{l},i} +$$

$$\psi_{\mathsf{r}}^n \psi_{\mathsf{r}}^{n-1} (\bar{\mathbf{n}}^{\mathsf{r}} \cdot \bar{\nabla} \bar{\psi}_{\mathsf{l},j}) \bar{\psi}_{\mathsf{r},i} \Big) \, \mathrm{d}\mathcal{S}$$

$$+ \frac{1}{2} \hat{\phi}_{\mathsf{r},j}^{n-1} \int_{\mathcal{S}} \psi_{\mathsf{r}}^{n-1} \Big(\psi_{\mathsf{l}}^n \psi_{\mathsf{l}}^{n-1} (\bar{\mathbf{n}}^{\mathsf{l}} \cdot \bar{\nabla} \bar{\psi}_{\mathsf{r},j}) \bar{\psi}_{\mathsf{l},i} +$$

$$\psi_{\mathsf{r}}^n \psi_{\mathsf{r}}^{n-1} (\bar{\mathbf{n}}^{\mathsf{r}} \cdot \bar{\nabla} \bar{\psi}_{\mathsf{r},j}) \bar{\psi}_{\mathsf{r},i} \Big) \, \mathrm{d}\mathcal{S} \Bigg)$$

$$- \sum_{\mathcal{S} \in \Gamma_{int}} \sum_{j=1}^{n_p} \sum_{k=1}^{3} n_{\mathcal{S}} \Bigg(\frac{1}{2} \hat{R}_{k,j}^{\mathcal{S},\mathsf{l}n} \int_{\mathcal{S}} \psi_{\mathsf{l}}^n \Big(\psi_{\mathsf{l}}^n \psi_{\mathsf{l}}^{n-1} n_k^{\mathsf{l}} \bar{\psi}_{\mathsf{l},j} \bar{\psi}_{\mathsf{l},i} +$$

$$\psi_{\mathsf{r}}^n \psi_{\mathsf{r}}^{n-1} n_k^{\mathsf{r}} \psi_{\mathsf{l},j} \psi_{\mathsf{r},i} \Big) \, \mathrm{d}\mathcal{S}$$

$$+ \frac{1}{2} \hat{R}_{k,j}^{\mathcal{S},\mathsf{r}n} \int_{\mathcal{S}} \psi_{\mathsf{r}}^n \Big(\psi_{\mathsf{l}}^n \psi_{\mathsf{l}}^{n-1} n_k^{\mathsf{l}} \psi_{\mathsf{r},j} \psi_{\mathsf{l},i} +$$

$$\psi_{\mathsf{r}}^n \psi_{\mathsf{r}}^{n-1} n_k^{\mathsf{r}} \psi_{\mathsf{r},j} \psi_{\mathsf{r},i} \Big) \, \mathrm{d}\mathcal{S} \Bigg)$$

$$- \sum_{\mathcal{S} \in \Gamma_{int}} \sum_{j=1}^{n_p} \sum_{k=1}^{3} n_{\mathcal{S}} \Bigg(\frac{1}{2} \hat{R}_{k,j}^{\mathcal{S},\mathsf{l}n-1} \int_{\mathcal{S}} \psi_{\mathsf{l}}^{n-1} \Big(\psi_{\mathsf{l}}^n \psi_{\mathsf{l}}^{n-1} n_k^{\mathsf{l}} \bar{\psi}_{\mathsf{l},j} \bar{\psi}_{\mathsf{l},i} +$$

$$\psi_{\mathsf{r}}^n \psi_{\mathsf{r}}^{n-1} n_k^{\mathsf{r}} \bar{\psi}_{\mathsf{l},j} \bar{\psi}_{\mathsf{r},i} \Big) \, \mathrm{d}\mathcal{S}$$

$$+ \frac{1}{2} \hat{R}_{k,j}^{\mathcal{S},\mathsf{r}n-1} \int_{\mathcal{S}} \psi_{\mathsf{r}}^{n-1} \Big(\psi_{\mathsf{l}}^n \psi_{\mathsf{l}}^{n-1} n_k^{\mathsf{l}} \bar{\psi}_{\mathsf{r},j} \bar{\psi}_{\mathsf{l},i} +$$

$$\psi_{\mathsf{r}}^n \psi_{\mathsf{r}}^{n-1} n_k^{\mathsf{r}} \bar{\psi}_{\mathsf{r},j} \bar{\psi}_{\mathsf{r},i} \Big) \, \mathrm{d}\mathcal{S} \Bigg)$$

$$
\begin{aligned}
&- \sum_{\mathcal{S}\in\Gamma_L} \sum_{j=1}^{n_p} \int_{\mathcal{S}} g_N \psi_{\mathsf{l}}^n \psi_{\mathsf{l}}^{n-1} \bar{\psi}_{\mathsf{l},i} \, \mathrm{d}\mathcal{S} \\
&- \sum_{\mathcal{S}\in\Gamma_S} \sum_{j=1}^{n_p} \hat{\eta}_{\mathsf{l},j}^n \int_{\mathcal{S}} \psi_{\mathsf{l}}^n \psi_{\mathsf{l}}^{n-1} (\partial_t \psi_{\mathsf{l},j}^n) \bar{\psi}_{\mathsf{l},i} \bar{\varphi}_{\mathsf{l},j} \, \mathrm{d}\mathcal{S} \\
&- \sum_{\mathcal{S}\in\Gamma_S} \sum_{j=1}^{n_p} \hat{\eta}_{\mathsf{l},j}^{n-1} \int_{\mathcal{S}} \psi_{\mathsf{l}}^n \psi_{\mathsf{l}}^{n-1} (\partial_t \psi_{\mathsf{l}}^{n-1}) \bar{\psi}_{\mathsf{l},i} \bar{\varphi}_{\mathsf{l},j} \, \mathrm{d}\mathcal{S} = 0.
\end{aligned} \tag{4.96}
$$

Next, the discretization of (4.74) is

$$
\begin{aligned}
&\sum_{\mathcal{S}\in\Gamma_S} \sum_{j=1}^{n_p} \hat{\phi}_{\mathsf{l},j}^n \int_{\mathcal{S}} \psi_{\mathsf{l}}^n \big(\partial_t (\psi_{\mathsf{l}}^n \psi_{\mathsf{l}}^{n-1})\big) \bar{\varphi}_{\mathsf{l},i} \bar{\psi}_{\mathsf{l},j} \, \mathrm{d}\mathcal{S} + \\
&\sum_{\mathcal{S}\in\Gamma_S} \sum_{j=1}^{n_p} \hat{\phi}_{\mathsf{l},j}^{n-1} \int_{\mathcal{S}} \psi_{\mathsf{l}}^{n-1} \big(\partial_t (\psi_{\mathsf{l}}^n \psi_{\mathsf{l}}^{n-1})\big) \bar{\varphi}_{\mathsf{l},i} \bar{\psi}_{\mathsf{l},j} \, \mathrm{d}\mathcal{S} - \\
&\sum_{\mathcal{S}\in\Gamma_S} \sum_{j=1}^{n_p} g \hat{\eta}_{\mathsf{l},j}^n \int_{\mathcal{S}} (\psi_{\mathsf{l}}^n)^2 \psi_{\mathsf{l}}^{n-1} \bar{\varphi}_{\mathsf{l},i} \bar{\psi}_{\mathsf{l},j} \, \mathrm{d}\mathcal{S} \\
&\sum_{\mathcal{S}\in\Gamma_S} \sum_{j=1}^{n_p} g \hat{\eta}_{\mathsf{l},j}^{n-1} \int_{\mathcal{S}} \psi_{\mathsf{l}}^n (\psi_{\mathsf{l}}^{n-1})^2 \bar{\varphi}_{\mathsf{l},i} \bar{\psi}_{\mathsf{l},j} \, \mathrm{d}\mathcal{S} = 0.
\end{aligned} \tag{4.97}
$$

To obtain and describe the linear system of algebraic equations from (4.96) and (4.97), we introduce and use the following matrix and vector notations:

$$
\begin{aligned}
A_{ij}^{\mathcal{K},\mathsf{k}} &:= \int_{\mathcal{K}_{\mathsf{k}}^n} \bar{\psi}_{\mathsf{k},i} \bar{\psi}_{\mathsf{k},j} \, \mathrm{d}\mathcal{K}, \\
B_{ij}^{\mathcal{K},\mathsf{kk}} &:= \int_{\mathcal{K}_{\mathsf{k}}^n} (\psi_{\mathsf{k}}^n)^2 \psi_{\mathsf{k}}^{n-1} \bar{\nabla} \bar{\psi}_{\mathsf{k},i} \cdot \bar{\nabla} \bar{\psi}_{\mathsf{k},j} \, \mathrm{d}\mathcal{K}, \\
\bar{B}_{ij}^{\mathcal{K},\mathsf{kk}} &:= \int_{\mathcal{K}_{\mathsf{k}}^n} (\psi_{\mathsf{k}}^{n-1})^2 \psi_{\mathsf{k}}^n \bar{\nabla} \bar{\psi}_{\mathsf{k},i} \cdot \bar{\nabla} \bar{\psi}_{\mathsf{k},j} \, \mathrm{d}\mathcal{K}, \\
C_{ij}^{\mathcal{S},\mathsf{lr}} &:= \int_{\mathcal{S}} \psi_{\mathsf{l}}^n \psi_{\mathsf{l}}^{n-1} \psi_{\mathsf{r}}^n (\bar{\mathbf{n}}^{\mathsf{l}} \cdot \bar{\nabla} \psi_{\mathsf{l},i}) \, \psi_{\mathsf{r},j} \mathrm{d}\mathcal{S}, \\
\bar{C}_{ij}^{\mathcal{S},\mathsf{lr}} &:= \int_{\mathcal{S}} \psi_{\mathsf{l}}^n \psi_{\mathsf{l}}^{n-1} \psi_{\mathsf{r}}^{n-1} (\bar{\mathbf{n}}^{\mathsf{l}} \cdot \bar{\nabla} \psi_{\mathsf{l},i}) \, \psi_{\mathsf{r},j} \mathrm{d}\mathcal{S},
\end{aligned}
$$

$$\hat{D}^{\mathcal{S},\mathsf{lr}}_{k,ij} := \int_{\mathcal{S}} n^{\mathsf{l}}_k \bar{\psi}_{\mathsf{l},i} \bar{\psi}_{\mathsf{r},j} \mathrm{d}\mathcal{S},$$

$$D^{\mathcal{S},\mathsf{lr}}_{k,ij} := \int_{\mathcal{S}} n^{\mathsf{l}}_k \psi^n_{\mathsf{l}} \psi^{n-1}_{\mathsf{l}} \psi^n_{\mathsf{r}} \bar{\psi}_{\mathsf{l},i} \bar{\psi}_{\mathsf{r},j} \mathrm{d}\mathcal{S},$$

$$\bar{D}^{\mathcal{S},\mathsf{lr}}_{k,ij} := \int_{\mathcal{S}} n^{\mathsf{l}}_k \psi^n_{\mathsf{l}} \psi^{n-1}_{\mathsf{l}} \psi^{n-1}_{\mathsf{r}} \bar{\psi}_{\mathsf{r},j} \bar{\psi}_{\mathsf{l},i} \mathrm{d}\mathcal{S},$$

$$G^{\mathcal{S}}_{ij} := \int_{\mathcal{S}} \psi^n_{\mathsf{l}} \psi^{n-1}_{\mathsf{l}} (\partial_t \psi^n_{\mathsf{l}}) \bar{\psi}_{\mathsf{l},i} \bar{\varphi}_{\mathsf{l},j} \, \mathrm{d}\mathcal{S},$$

$$\bar{G}^{\mathcal{S}}_{ij} := \int_{\mathcal{S}} \psi^n_{\mathsf{l}} \psi^{n-1}_{\mathsf{l}} (\partial_t \psi^{n-1}_{\mathsf{l}}) \bar{\psi}_{\mathsf{l},i} \bar{\varphi}_{\mathsf{l},j} \, \mathrm{d}\mathcal{S},$$

$$L^{\mathcal{S}}_{ij} := \int_{\mathcal{S}} \psi^n_{\mathsf{l}} \big(\partial_t (\psi^n_{\mathsf{l}} \psi^{n-1}_{\mathsf{l}})\big) \bar{\varphi}_{\mathsf{l},i} \bar{\psi}_{\mathsf{l},j} \, \mathrm{d}\mathcal{S},$$

$$\bar{L}^{\mathcal{S}}_{ij} := \int_{\mathcal{S}} \psi^{n-1}_{\mathsf{l}} \big(\partial_t (\psi^n_{\mathsf{l}} \psi^{n-1}_{\mathsf{l}})\big) \bar{\varphi}_{\mathsf{l},i} \bar{\psi}_{\mathsf{l},j} \, \mathrm{d}\mathcal{S},$$

$$H^{\mathcal{S}}_{ij} := \int_{\mathcal{S}} (\psi^n_{\mathsf{l}})^2 \psi^{n-1}_{\mathsf{l}} \bar{\varphi}_{\mathsf{l},i} \bar{\varphi}_{\mathsf{l},j} \, \mathrm{d}\mathcal{S},$$

$$\bar{H}^{\mathcal{S}}_{ij} := \int_{\mathcal{S}} (\psi^{n-1}_{\mathsf{l}})^2 \psi^n_{\mathsf{l}} \bar{\varphi}_{\mathsf{l},i} \bar{\varphi}_{\mathsf{l},j} \, \mathrm{d}\mathcal{S},$$

$$E^{\mathcal{S},\mathsf{l}}_i := \int_{\mathcal{S}_{\mathsf{m}}} g_N \psi^n_{\mathsf{l}} \psi^{n-1}_{\mathsf{l}} \psi_{\mathsf{l},i} \mathrm{d}\mathcal{S},$$

$$M^{\mathsf{ll}} := \sum_{k=1}^{3} \Big(D^{\mathcal{S},\mathsf{ll}}_k (A^{\mathcal{K},\mathsf{l}})^{-1} (\hat{D}^{\mathcal{S},\mathsf{ll}}_k)^T + D^{\mathcal{S},\mathsf{lr}}_k (A^{\mathcal{K},\mathsf{r}})^{-1} (\hat{D}^{\mathcal{S},\mathsf{lr}}_k)^T \Big),$$

$$M^{\mathsf{lr}} := \sum_{k=1}^{3} \Big(D^{\mathcal{S},\mathsf{ll}}_k (A^{\mathcal{K},\mathsf{l}})^{-1} (\hat{D}^{\mathcal{S},\mathsf{rl}}_k)^T + D^{\mathcal{S},\mathsf{lr}}_k (A^{\mathcal{K},\mathsf{r}})^{-1} (\hat{D}^{\mathcal{S},\mathsf{rr}}_k)^T \Big),$$

$$M^{\mathsf{rl}} := \sum_{k=1}^{3} \Big(D^{\mathcal{S},\mathsf{rl}}_k (A^{\mathcal{K},\mathsf{l}})^{-1} (\hat{D}^{\mathcal{S},\mathsf{ll}}_k)^T + D^{\mathcal{S},\mathsf{rr}}_k (A^{\mathcal{K},\mathsf{r}})^{-1} (\hat{D}^{\mathcal{S},\mathsf{lr}}_k)^T \Big),$$

$$M^{\mathsf{rr}} := \sum_{k=1}^{3} \Big(D^{\mathcal{S},\mathsf{rl}}_k (A^{\mathcal{K},\mathsf{l}})^{-1} (\hat{D}^{\mathcal{S},\mathsf{rl}}_k)^T + D^{\mathcal{S},\mathsf{rr}}_k (A^{\mathcal{K},\mathsf{r}})^{-1} (\hat{D}^{\mathcal{S},\mathsf{rr}}_k)^T \Big),$$

$$\bar{M}^{\mathsf{ll}} := \sum_{k=1}^{3} \Big(\bar{D}^{\mathcal{S},\mathsf{ll}}_k (A^{\mathcal{K},\mathsf{l}})^{-1} (\hat{D}^{\mathcal{S},\mathsf{ll}}_k)^T + \bar{D}^{\mathcal{S},\mathsf{lr}}_k (A^{\mathcal{K},\mathsf{r}})^{-1} (\hat{D}^{\mathcal{S},\mathsf{lr}}_k)^T \Big),$$

$$\bar{M}^{\mathsf{lr}} := \sum_{k=1}^{3} \Big(\bar{D}_k^{\mathcal{S},\mathsf{ll}} (A^{\mathcal{K},\mathsf{l}})^{-1} (\hat{D}_k^{\mathcal{S},\mathsf{rl}})^T + \bar{D}_k^{\mathcal{S},\mathsf{lr}} (A^{\mathcal{K},\mathsf{r}})^{-1} (\hat{D}_k^{\mathcal{S},\mathsf{rr}})^T \Big),$$

$$\bar{M}^{\mathsf{rl}} := \sum_{k=1}^{3} \Big(\bar{D}_k^{\mathcal{S},\mathsf{rl}} (A^{\mathcal{K},\mathsf{l}})^{-1} (\hat{D}_k^{\mathcal{S},\mathsf{ll}})^T + \bar{D}_k^{\mathcal{S},\mathsf{rr}} (A^{\mathcal{K},\mathsf{r}})^{-1} (\hat{D}_k^{\mathcal{S},\mathsf{lr}})^T \Big),$$

$$\bar{M}^{\mathsf{rr}} := \sum_{k=1}^{3} \Big(\bar{D}_k^{\mathcal{S},\mathsf{rl}} (A^{\mathcal{K},\mathsf{l}})^{-1} (\hat{D}_k^{\mathcal{S},\mathsf{rl}})^T + \bar{D}_k^{\mathcal{S},\mathsf{rr}} (A^{\mathcal{K},\mathsf{r}})^{-1} (\hat{D}_k^{\mathcal{S},\mathsf{rr}})^T \Big). \tag{4.98}$$

Given ϕ_{h}^{n-1} and η_{h}^{n-1}, we can construct the linear system $\mathcal{L}\Phi^n = \mathcal{X}$ and solve it for ϕ_{h}^n. Subsequently, we obtain η_{h}^n using (4.81).

Chapter 5

Conclusions and Recommendations

The main objective of the present research was to develop a stable, efficient and accurate numerical scheme for shallow and deep water waves that is suitable for deforming grids and thus time dependent boundaries. To achieve this goal, we have used a space-time discontinuous Galerkin finite element method. The motivation for using this method is that it does not distinguish between space and time, and therefore provides flexibility to accommodate time dependent boundaries. Thus, our research has focused on developing and testing a space-time discontinuous Galerkin scheme for nonlinear shallow water waves in Chapters 2 and 3, and for linear free surface gravity water waves in Chapter 4. We now present our conclusions and recommendations for future research. This will be presented in two parts in accordance with our research objectives: (i) modeling shallow water waves and (ii) modeling linear free surface water waves. In addition, we discuss to what extent we have achieved the milestones set in Chapter 1.

5.1 Modeling shallow water waves

In Chapter 2, we presented a novel space-time discontinuous Galerkin finite element discretization for the nonlinear (rotational) shallow water equations over a irregular bottom topography. The novel aspects of this discretization

are:

(i) Local application of the numerical dissipation operator around bores and hydraulic jumps with the help of a discontinuity detector. As a consequence, we can preserve the accuracy of the numerical scheme in smooth regions of the wave field and suppress the spurious oscillations around discontinuities and sharp gradients.

(ii) The bottom topography is approximated in such a way that it is smooth and piecewise continuous. This helps to preserve exactly the steady rest state of a lake at the discrete level. In practice, such property ensures that the numerical scheme does not produce any undesirable artificial flow near to the steady rest state.

(iii) The numerical HLLC flux is unified in space and time, which makes it applicable to all the faces of a space-time finite element.

The space-time DG discretization of the shallow water equations results in a set of nonlinear algebraic equations. These are solved by integrating in pseudo-time until a steady state is reached in pseudo-time. The key feature of the pseudo-time integration method is that its CFL pseudo-time step is local, i.e. the pseudo-time step can vary per space-time finite element. This feature improves convergence to a steady state solution in pseudo-time even on non-uniform grids with varying cell sizes. Furthermore, we propose to combine the pseudo-time integration method with the multi-grid solution techniques developed by Klaij et al. [31] in the near future to increase the convergence to steady state in pseudo-time. Thus, we have developed an efficient space-time discontinuous Galerkin finite element scheme for shallow water waves and achieved the first mile stone set for modeling shallow water waves.

Having obtained a space-time DG finite element scheme for the shallow water equations, we considered the verification and validation of the scheme through a number of test cases. The test cases range from simple exact solutions to experiments supported by shallow water theory. The scheme was first verified against exact solutions for its accuracy. Next, it was verified for wave dispersion and dissipation errors. This was done by conducting a discrete Fourier analysis of the space-time DG discretization.

To demonstrate the applicability of the numerical scheme for problems arising in geophysical fluid dynamics and problems with deforming grids, we

considered Kelvin and Poincaré waves in a rectangular and circular basin, and harmonic waves generated by a linear wave maker in a wave basin, respectively. These tests failed for traditional zero normal flow boundary condition at solid walls. This has lead to investigate and devise new boundary conditions for solid walls, and they have proved crucial to accurately capture these waves.

An important theoretical aspect of shallow water waves is that they conserve energy and potential vorticity in the smooth parts of the wave field, and that they dissipate energy and may generate potential vorticity in the presence of bores. In order to validate this, we considered test cases consisting of bores that dissipate energy non uniformly across the bore and consequently generate vorticity. The present numerical scheme has captured this bore-vortex phenomena in good agreement with its anomaly. Finally, the numerical scheme is validated, qualitatively and quantitatively, against a laboratory experiment in which oblique hydraulic jumps are formed in super critical steady state flows. Having successfully tested these cases with our numerical scheme, we can say that the second milestone has been achieved.

The third and last milestone set for modeling shallow water waves is to capture the complicated phenomenon of flooding and drying. To capture this phenomenon in the space-time discontinuous Galerkin scheme, we first considered to model flooding and drying on simple (rectangular) domains in which the shoreline is assumed to be single valued with respect to a fixed reference line roughly parallel to the shoreline. The fixed reference line is typically choosen as the opposite boundary of the shoreline. At the shoreline, the zero water depth condition is satisfied by constraining the slope of the water depth. Further to accurately predict the movement of the shore line, we have chosen to approximate the wave field in primitive variables (h, u, v) instead of the conservative variables (h, hu, hv). This helped to accurately resolve the velocity of the water particles at the shoreline and subsequently, the movement of the shoreline. Although the initial tests were encouraging but we are facing the following numerical difficulties:

(i) Artificial numerical dissipation applied around the bores does not guarantee the non-negativity of the water depth. This poses a problem when bores are near to the shore line boundary. However, initial tests for smooth cases were encouraging, cf. Ambati [2].

(ii) Slope limiters are commonly used to preserve positivity of the water depth (see Bokhove [12]) but in our space-time DG finite element scheme the slope limiters stall the convergence of the pseudo-time integration to steady state.

(iii) It is difficult to handle the mesh deformation caused by the moving shore line boundary and by the possibility of merging and emerging dry patches on an irregular topography.

In order to deal with these difficulties, further research is necessary.

Based on the present research for shallow water waves, we recommend the following:

1. To exactly preserve a steady rest state at the discrete level, we have choosen a smooth approximation of the topography over the computational domain. However, a discontinuous approximation of the topography which can preserve a steady rest state at the discrete level in a space-time discontinuous Galerkin discretization is recently presented by Rhebergen et al. [50]. Such a discretization helps to deal with a discontinuous topography in practical applications. Further, it will be useful in modeling the sediment morphological evolution of sea and river beds, cf. Tassi et al. [58].

2. Implementing multi-grid algorithms will further improve the efficiency of the implicit space-time DG finite element scheme and will make the scheme more economical to use for practical applications.

3. We strongly recommend to use the polynomial approximation of the primitive variables (h, u, v) in the shallow water equations instead of the conservative variables (h, hu, hv). This is particularly advantageous for the flooding and drying phenomenon as the velocity field will be available at the shore line where the water depth tends to zero. We have also observed that the use of primitive variables accelerates the rate of convergence of the pseudo-time integration method.

4. We also recommend investigating either a positivity preserving numerical dissipation or a positivity preserving slope limiter that does not stall the convergence of the pseudo-time integration.

We hope the recommendations can pave the way for capturing the flooding and drying phenomenon by the use of a space-time DG finite element discretization.

5.2 Modeling linear free surface water waves

In Chapter 4, we first presented the space-time discontinuous Galerkin finite element discretization for the linear free surface gravity wave equations and verified the resulting numerical scheme against exact solutions. The salient features of this discretization are

(i) Eliminating the velocity field by using a primal formulation and global lifting operators. This has significantly reduced the number of degrees of freedom needed for the velocity field.

(ii) Approximating the global lifting operator on a face with its local counterpart lifting operator of the respective face. As a consequence, the discretization results in a linear algebraic system of equations with a compact stencil.

(iii) Coupling the kinematic and dynamic free surface boundary conditions to the weak formulation of the potential flow equation. This is done through the numerical flux at the free surface and it ensures the stability of the resulting numerical scheme.

This accomplished the first mile stone that was set for modeling the deep water waves.

Next, we presented a novel space-time variational (dis)continuous Galerkin method for linear free surface waves. The novelty of this method is the discrete variational formulation based on Luke's variational principle instead of a weak formulation. Such a variational formulation has resulted in a numerical scheme which shows no decay in the amplitude of the linear harmonic waves in a periodic domain and harmonic waves generated in a wave basin. Further, the numerical scheme has all the salient features that were mentioned for the space-time discontinuous Galerkin method. However, the space-time variational (dis)continuous Galerkin scheme shows a larger dispersion error. This concludes the achievement of the second mile stone for the modeling of linear free surface waves.

The linear system of algebraic equations resulting from the discretization of both the space-time discontinuous Galerkin method and the space-time variational (dis)continuous Galerkin method has a sparse global matrix. The sparsity of the global matrix is limited by the maximum number of neighboring elements to any given element in the computational domain. More precisely, the global matrix can be divided into block rows with each block row corresponding to an element in the computational domain. The number of non-zero blocks in a block row is equal to the number of neighboring elements of that element. Such a block sparse matrix structure has drawn our attention to the PETSc package [53, 52, 54] designed to construct and solve linear systems of equations. The PETSc package has a large suite of efficient sparse matrix storage routines and sparse linear solvers with an added advantage of parallelization. Among them, the block matrix storage routine of the PETSc package is the best choice for building the present linear system of equations. Biconjugate gradient and conjugate gradient solvers with ILU preconditioners are chosen to solve the linear system of equations resulting from space-time DG and space-time variational methods. These choices improved the performance of our numerical code and saved a significant amount of time in building our global system.

The space-time DG finite element scheme for linear free surface waves was verified by comparing the numerical results with two exact solutions, one for linear harmonic waves propagating in a periodic domain and another for waves generated by a wave maker in a wave basin. Finally, we conclude that the space-time finite element scheme for linear free surface waves combined with the PETSc package has resulted in a fast, accurate and stable numerical scheme. Thus, we have achieved the milestone set for modeling deep water waves in Chapter 1.

Based on the present research work for linear free surface waves, we recommend the following:

1. Space-time variational discontinuous Galerkin scheme is advantageous for the long time simulations of linear free surface waves with no decay in the amplitude of the waves which indicates better energy conservation then the scheme proposed by van der Vegt and Xu [65]. Hence, the extension of this scheme to nonlinear free surface waves will be useful for practical applications. The scheme, however, needs improvement in minimizing the dispersion error in the numerical sim-

ulations which can be achieved by investigating better time discretizations.

2. The performance of the developed numerical schemes depends largely on the sparse matrix storage routines. To gain further improvements in performance, it is recommended that the memory for the matrix storage be preallocated rather than the use of the dynamic memory allocation.

3. If p adaptivity is required, then we recommend using the sparse matrix storage routine of PETSc since the block sparse matrix storage routine requires the same block size for each block row of the global matrix.

4. For practical applications, it is useful to parallelize the present numerical scheme since a parallelized version of PETSc is available.

5. We recommend the extension of the present numerical scheme to nonlinear free surface waves by developing an efficient nonlinear solver using the pseudo-time integration method in combination with multigrid technique instead of the Newton method used by van der Vegt and Xu [65].

Bibliography

[1] B. Akers, Shallow water flow through a contraction, GFD Fellowship program 2005, Woods Hole Oceanographic Institution, 2005. `http://gfd.whoi.edu/proceedings/2005/PDFvol2005.html`

[2] V.R. Ambati, Flooding and drying in discontinuous Galerkin discretizations of shallow water equations. ECCOMAS Egmond aan Zee 2006, European Conference on CFD, 2006. `http://proceedings.fyper.com/eccomascfd2006`

[3] V.R. Ambati and O. Bokhove, Space-time discontinuous Galerkin finite element method for shallow water flows, *J. Comput. Appl. Math.* **204**(2), 452–462, 2007.

[4] V.R. Ambati and O. Bokhove, Space-time discontinuous Galerkin discretization of rotating shallow water equations, *J. Comput. Phys.* **225**(2), 1233–1261, 2007.

[5] D.N. Arnold, F. Brezzi, B. Cockburn and L.D. Marini, Unified analysis of discontinuous Galerkin methods for elliptic problems, *SIAM J. Numer. Anal.* **39**(5), 1749–1779, 2002.

[6] E. Audusse, F. Bouchut, M.-O. Bristeau, R. Klein and B. Perthame, A fast and stable well-balanced scheme with hydrostatic reconstruction for shallow water flows, *SIAM J. Sci. Comp.* **25**, 2050–2065, 2004.

[7] E. Audusse and M.-O. Bristeau, A well-balanced positivity preserving "second-order" scheme for shallow water flows on unstructured grids. *J. Comp. Phys.* **206**, 311–333, 2006.

[8] K.J. Bai and J.W. Kim, A finite element method for free surface flow problems, *Theor. Appl. Mech.,* **1**(1), 1–27, 1995.

[9] P. Batten, N. Clarke, C. Lambert and D.M. Causon, On the choice of wavespeeds for the HLLC Riemann solver, *SIAM J. Sci. Comput.* **18**(6), 1553–1570, 2997.

[10] J.T. Beale, A Convergent Boundary Integral Method for Three-Dimensional Water Waves, *Math. Comp.*, **70**, 977–1029, 2001.

[11] O. Bokhove, Flooding and drying in finite-element Galerkin discretizations of shallow water equations. Part I: one dimension, *J. Sci. Comput.* **22**, 47–82, 2005.

[12] O. Bokhove, Flooding and drying in finite-element discretizations of shallow-water equations. Part II: Two dimensions, *Memorandum no. 1684*, Department of applied mathematics, University of Twente, The Netherlands, 2003.

[13] F. Bouchut, *Nonlinear stability of finite volume methods for hyperbolic conservation laws: and well-balanced scheme for sources*, Frontiers in Mathematics, Birkhauser, 2004.

[14] F. Bouchut, J. Le Sommer and V. Zeitlin, Frontal geostrophic adjustment and nonlinear-wave phenomena in one dimensional rotating shallow water. Part 2: high-resolution numerical simulations, *J. Fluid Mech.* **514**, 35–63, 2004.

[15] F. Brezzi, G. Manzini, D. Marini, P. Pietra and A. Russo, Discontinuous Galerkin approximations for elliptic problems, *Numer. Methods Partial Differential Eq.*, **16**(4), 365–378, 2000.

[16] J. Broeze, E.F.G. van Daalen and P. J. Zandbergen, A three-dimensional panel method for nonlinear free surface waves on vector computers, *Comput. Mech.*, **13**, 12–28, 1993.

[17] O. Bühler, On the vorticity transport due to dissipating or breaking waves in shallow-water flow, *J. Fluid Mech.* **407**, 235–263, 2000.

[18] X. Cai, H.P. Langtangen, B.F. Nielsen and A. Tvieto, A finite element method for fully nonlinear water waves, *J. Comput. Phys.*, **143** 544–568, 1998.

[19] B. Cockburn, *Discontinuous Galerkin methods for convection-dominated problems*, Lecture Notes in Computational Science and Engineering, Vol. 9, Springer-Verlag, Berlin, 1999.

[20] B. Cockburn, G.E. Karniadakis and C.-W. Shu, Eds., *Discontinuous Galerkin Methods. Theory, Computation and Applications*, Lecture notes in Computational Science and Engineering, Vol. 11, Springer-Verlag, Berlin, 2000.

[21] B. Cockburn and C.-W. Shu, The Runge-Kutta discontinuous Galerkin method for conservation laws V: multidimensional systems, *J. Comput. Phys.*, **141** 199–224, 1998.

[22] B. Cockburn and C.-W. Shu, Runge-Kutta Discontinuous Galerkin methods for convection-dominated problems, *J. Sci. Comput.*, **16** 173–261, 2001.

[23] W. Craig and C. Sulem, Numerical simulation of gravity waves, *J. Comput. Phys.*, **108** 73–83, 1993.

[24] C. Dawson and J. Proft, Discontinuous and coupled continuous/discontinuous Galerkin methods for the shallow water equations, *Comp. Meth. Appl. Mech. Eng.*, **191**, 421–4746, 2002.

[25] G. Hu, Note on numerical simulation of shallow water, Bristol University, School of Mathematics, Rep. No. AM-02-01, 2002.

[26] J. Jaffre, C. Johnson and A. Szepessy, Convergence of the discontinuous Galerkin method for hyperbolic conservation laws, *Math. Models and Methods in Appl. Sci.* **5**, 367–386, 1995.

[27] R.S. Johnson, A Modern Introduction to the Mathematical Theory of Water Waves, Cambridge University Press, Cambridge, 1997.

[28] J.W. Kim and K.J. Bai, A finite element method for two dimensional water wave problems, *Int. J. Numer. Methods Fluids,* **30**(1), 105–121, 1999.

[29] J.W. Kim, K.J. Bai, R.C. Ertekin, and W.C. Webster, A strongly-nonlinear model for water waves in water of variable depth – The irrotational Green-Naghdi model, *J. Offshore Mech. Arct. Eng.,* 125(1), 25–32.

[30] C.M. Klaij, J.J.W. van der Vegt and H. van der Ven, Spacetime discontinuous Galerkin method for the compressible NavierStokes equations, *Journal of Comput. Phys.,* **217**(2), 589–611, 2006

[31] C.M. Klaij, M.H. van Raalte, H. van der Ven, and J.J.W. van der Vegt, h-Multigrid for space-time discontinuous Galerkin discretizations of the compressible Navier-Stokes equations, *Journal of Comput. Phys.,* **227**(2), 1024–1045, 2007.

[32] G.Klopman. M. Dingemans and E. van Groesen, A variational model for fully non-linear water waves of Boussinesq type, *Proceedings of 20th International Workshop on Water Waves and Floating Bodies*, Spitsbergen, Norway, 2005.

[33] L. Krivodonova, J. Xin, J.-F. Remacle, N. Chevaugeon and J.E. Flaherty, Shock detection and limiting with discontinuous Galerkin methods for hyperbolic conservation laws, *Appl. Numer. Math.* **48**, 323–338, 2004.

[34] A. Kurganov and D. Levy, Central-upwind schemes for the Saint-Venant equations. *Math. Modelling and Num. Anal.* **36**, 397–425, 2002.

[35] H. Lamb, *Hydrodynamics*, Dover Publications, New York, 1932.

[36] R.J. LeVeque, *Numerical methods for conservation laws*, Birkhäuser Verlag, Berlin, 1992.

[37] R.J. LeVeque, Wave propagation algorithms for multi-dimensional hyperbolic systems. *J. Comput. Phys.* **131**, 327–353, 1997.

[38] M.S. Longuet-Higgins and E.D. Cokelet, The deformation of steep surface waves on water, I. A numerical method of computation, *Proc. Roy. Soc. London A*, **35**, 1–26, 1976.

[39] J.C. Luke, A variational principle for a fluid with a free surface. *J. Fluid Mech.*, **27**(2), 395–397, 1967.

[40] H. Matsutomi and A. Michizula, Behaviour of a bore over a conical shoal. *Tohoku Journal of Natural Disaster Science*, in Japanese, 2001.

[41] Q.W. Ma, G.X. Wu and R. Eatock Taylor, Finite element simulation of fully nonlinear interaction between vertical cylinders and steep waves. Part 2: Methodology and numerical procedure, *Int. J. Numer. Meth. Fluids*, **36**, 265–285.

[42] Q.W. Ma, G.X. Wu and R. Eatock Taylor, Finite element simulation of fully nonlinear interaction between vertical cylinders and steep waves. Part 1: Numerical results and validation, *Int. J. Numer. Meth. Fluids*, **36**, 287–308.

[43] Q.W. Ma and S. Yan, Quasi ALE finite element method for nonlinear water waves, *J. Comput. Phys.*, **212**, 52–72, 2006.

[44] S. McCormick, B. Briggs and V. Henson, *A multigrid tutorial*. SIAM, Philadelphia, 2000.

[45] J.W. Miles, On Hamiltons principle for surface waves, *J. Fluid Mech.,* **83**(1), 153–158, 1977.

[46] D.M. Milder, A note on: On Hamilton's principle for surface waves, *J. Fluid Mech.,* **83**(1), 159–161, 1977.

[47] J. Pedlosky, *Geophysical fluid dynamics*, Springer, New York, 1998.

[48] D.H. Peregrine, Surf zone currents, *Theoret. Comput. Fluid Dynamics* **10**, 295–309, 1998.

[49] L.J. Pratt, On inertial flow over topography, Part 1: Semigeostrophic adjustment to an obstacle, *Journal of fluid mechanics* **131**, 195–218, 1983.

[50] S. Rhebergen, O. Bokhove and J.J.W. van der Vegt, Discontinuous Galerkin finite element methods for hyperbolic nonconservative partial differential equations. *J. Comp. Phys.* Article in press, 2007. `http://eprints.eemcs.utwente.nl`.

[51] J.E. Romate and P.J. Zandbergen, Boundary integral equation formulations for free-surface flow problems in two and three dimensions, *Comput. Mech.,* 4(4), 1989.

[52] B. Satish, B. Kris, E. Victor, D.G. William, K. Dinesh, G.K. Matthew, McInnes C. Lois, B.F. Smith and Z. Hong, *PETSc users manual*, Argonne National Laboratory, NL-95/11 - Revision 2.1.5, 2004. `http://www-unix.mcs.anl.gov/petsc`

[53] B. Satish, B. Kris, D.G. William, K. Dinesh, G.K. Matthew, McInnes C. Lois, B.F. Smith and Z. Hong, *PETSc Web page*, 2001. http://www.mcs.anl.gov/petsc

[54] B. Satish, D.G. William, McInnes C. Lois and B.F. Smith, *Efficient Management of Parallelism in Object Oriented Numerical Software Libraries*, In Modern Software Tools in Scientific Computing by E. Arge, A.M. Bruaset and H.P. Langtangen, Birkhä user Press, 163–202. 1997.

[55] A.H. Shapiro, *The dynamics and thermodynamics of compressible fluid flow*, Ronald, New York, 1953.

[56] J.J. Stoker, *Water waves: The mathematical theory with applications*, Interscience publishers, New York, 1957.

[57] P.A. Tassi, O. Bokhove and C.A. Vionnet, Space discontinuous Galerkin method for shallow water flows —kinetic and HLLC flux, and potential vorticity generation, *Advances in water resource*, **30**(4), 998–1015, 2007.

[58] P.A. Tassi, S. Rhebergen, C.A. Vionnet and O. Bokhove, A discontinuous Galerkin finite element model for morphological evolution under shallow flows. Submitted to *Computer Methods in Applied Mech. and Eng.*, 2007. `http://eprints.eemcs.utwente.nl`

[59] S.K. Tomar and J.J.W. van der Vegt, Runge-Kutta discontinuous Galerkin method for linear free-surface gravity waves using high order velocity recovery, *Computer Methods in Applied Mechanics and Engineering,* **196**(13-16), 1984–1996, 2007.

[60] E.F. Toro, *Shock-capturing methods for free-surface flows*, Wiley, Toronto, 2001.

[61] E.F. Toro, M. Spruce and W. Speares, Restoration of the contact surface in the HLL-Riemann solver, *Shock Waves* **4**, 25–34, 1994.

[62] W. Tsai and D. Yue, Compuations of nonlinear free-surface flows, *Ann. Rev. Fluid Mech.*, **28**, 249–278, 1996.

[63] J.J.W. van der Vegt and S.K. Tomar, Discontinuous Galerkin Method for linear free surface gravity wave, *J. Sci. Comput.* **22**(1), 531–567, 2005.

[64] J.J.W. van der Vegt and H. van der Ven, Space-time discontinuous Galerkin finite element method with dynamic grid motion for inviscid compressible flows, *J. Comput. Phys.* **182**, 546–585, 2002.

[65] J.J.W. van der Vegt and Y. Xu, Space-time Discontinuous Galerkin Method for nonlinear water waves, *J. Comput. Phys.* **224**(1) 17–39, 2007.

[66] A.W. Vreman, M. Al-Tarazi, J.A.M. Kuipers, M. van Sint Annaland and O. Bokhove, Supercritical shallow granular flow through a contraction: experiment, theory and simulation, *J. Fluid Mech.*, **578**, 233–269, 2007.

[67] T. Vinje and P. Brevig, Numerical simulation of breaking waves, *Adv. Water Resources*, **4**, 77–82, 1981.

[68] J.H. Westhuis, The numerical simulation of nonlinear water waves in a hydrodynamic model test basin, Ph.D. thesis, University of Twente, Enschede, The Netherlands, 2001.

[69] G.B. Whitham, Linear and Nonlinear Waves, Wiley-Interscience, New York, 1974.

[70] G.X. Wu and R.E. Taylor, Finite element analysis fo two dimensional non-linear transient water waves, *Appl. Ocean Res.*, **16** 263–372, 1994.

[71] G.X. Wu and Z.Z. Hu, Simulation of nonlinear interactions between waves and floating bodies through a finite-element based numerical tnk, *Proc. R. Soc. Lond. Se. A* 460, 2797–2817, 2004.

Summary

Forecasting water waves and currents in near shore and off shore regions of the seas and oceans is essential to maintain and protect our environment and man made structures. In wave hydrodynamics, waves can be classified as shallow and deep water waves based on its water depth. The mathematical models of these waves are shallow water and free surface gravity water wave equations which describe the hydrodynamics of waves and currents near shore and off shore regions of seas and oceans. The complexity in these models exist as moving boundaries whose position depends on the solution of the governing equations. For shallow water waves, it is the shore line boundary where the water depth falls dry and for deep water waves, it is the free surface which separates the sea or ocean from atmospheric air. It is often difficult to solve these wave equations analytically while solving them numerically in an efficient and accurate way is a challenging task because of the moving boundaries. The numerical challenges are two fold: one is to develop a numerical method which is accurate and efficient for deforming grids and the other is to design a numerical algorithm for the grid adaptation following the moving boundaries. In this thesis, we aimed at first developing space-time discontinuous Galerkin finite element schemes for shallow water and free surface gravity water wave equations which are accurate and efficient for deforming grids.

The shallow water equations are a leading order hydrodynamic model for coastal waves and currents. This is because they can exhibit the complicated flooding and drying phenomena due to the moving shore line boundary, and the wave breaking phenomena in the form of bores. A new

space-time discontinuous Galerkin (DG) discretization is first presented for the (rotating) shallow water equations over varying topography and fixed boundaries. We formulated the discretization in an efficient and conservative way with the numerical HLLC flux on the finite element boundaries. We also designed a novel way to apply numerical dissipation around discontinuities, that are present in the form of bores, with the help of Krivodonova's discontinuity indicator such that the spurious oscillations are suppressed. The non-linear algebraic system resulting from the space-time discretization is solved using a pseudo-time integration method. A thorough verification of the space-time DG finite element method is undertaken by comparing the numerical and exact solutions. We carried out a discrete Fourier analysis of the one dimensional linear rotating shallow water equations to show that the method is unconditionally stable with minimal dispersion and dissipation error. The numerical scheme is verified and validated for a number of problems arising in geophysical flows. To demonstrate that the space-time DG method is particularly suitable for problems with dynamic grid motion, we simulated nonlinear waves generated by a wave maker and verified these for low amplitude waves where linear theory is approximately valid.

Free surface gravity water wave equations is widely used in marine and offshore engineering to model waves. The mathematical nature of these equations is complex because it consists of a potential flow equation which is of elliptic nature and nonlinear free surface boundary conditions which are hyperbolic in nature. Hence, a space-time discontinuous Galerkin finite element method is presented for simplified linear free surface gravity water waves. The free surface gravity water wave equations also arise from Luke's variational formulation which is associated with the conservation of energy and phase space, under suitable boundary conditions. This variational formulation also provided a basis to obtain a novel space-time variational (dis)continuous Galerkin finite element method. Both the space-time discontinuous Galerkin and the space-time variational finite element discretizations result in an algebraic linear system of equations with a very compact stencil, i.e., the algebraic equations from each element is coupled to its immediate neighboring elements only. Thus, the linear system of equations are built using an efficient block sparse matrix storage routine and solved by using iterative linear solvers using a well-tested PETSc package.

Numerical schemes are verified for harmonic waves in a periodic domain and generated in a wave basin.

Extension of the space-time discontinuous Galerkin method for flooding and drying in shallow water waves and nonlinear free surface evolution of deep water waves will be the topic of future research.

Samenvatting

Het voorspellen van water golven en stromingen in near-shore en off-shore gebieden van zeeën en oceanen is essentieel voor het onderhouden en beschermen van ons milieu en gebouwen in deze regios. In de hydrodynamica kunnen golven geclassifiseerd worden als ondiep of diepe water golven, afhankelijk van de water diepte. De wiskundige modellen die de hydrodynamica van deze golven beschrijven zijn de ondiep water vergelijkingen, in near-shore gebieden en de vrije-oppervlakte gravity water wave vergelijkingen voor de off-shore gebieden. De complexiteit in deze modellen zit in de bewegende randen van welk de positie afhangt van de oplossing van het model. Voor de ondiep water golven zitten deze bewegende randen in de kust lijn waar de water diepte nul wordt en voor de diep water golven is het de vrije oppervlakte die de zee of oceaan van de lucht scheidt. Vaak is het moeilijk om deze golf vergelijkingen analytisch op te lossen terwijl het efficient en nauwkeurig oplossen met numerieke methodes bemoeilijkt wordt vanwege de bewegende randen. Er zijn twee numerieke uitdagingen: het ontwikkelen van een numerieke methode die nauwkeurig en efficient is voor vervormende grids en het ontwerpen van een numerieke algoritme voor grid adaptatie zodat deze de bewegende randen volgt. In dit proefschrift hebben wij gestreefd naar het ontwikkelen van ruimte-tijd discontinue Galerkin eindige elementen methodes voor ondiep water vergelijkingen en vrije oppervlakte gravity wave vergelijkingen die nauwkeurig en efficient zijn voor vervormende grids.

De ondiep water vergelijkingen zijn een leidende orde hydrodynamische model voor kust golven en stromingen. Dit komt doordat het model het

verschijnsel van flooding en drying, als gevolg van een bewegende kustlijn, alsmede het breken van golven kan simuleren. Een nieuwe ruimte-tijd discontinue Galerkin (DG) discretisatie wordt gepresenteerd voor de (rotating) ondiep water vergelijkingen over varierende topografie en vaste randen. Wij hebben de discretisatie op een efficiente en conservatieve manier geformuleerd met de HLLC flux op de eindige elementen randen. Ook hebben we een nieuw manier ontwikkeld om numerieke dissipatie rond discontinuiteiten, die optreden in de vorm van brekende golven (bores), toe te passen met behulp van Krivodonova's discontinuiteiten detector zodanig dat numerieke schommelingen onderdrukt worden. De niet-lineaire algebraisch systeem als gevolg van de ruimte-tijd discretisatie wordt opgelost door gebruik te maken van een pseudo-tijdstaps methode. Een uitgebreide verificatie van de ruimte-tijd DG eindige elementen methode wordt ondergaan door numerieke oplossingen te vergelijken met exacte oplossingen. Ook hebben we een discrete Fourier analyse uitgevoerd van de één dimensionale lineaire rotating ondiep water vergelijkingen om te laten zien dat de methode onvoorwaardelijk stabiel is met minimale dispersie en dissipatie fouten. De numerieke schema is geverifieerd en gevalideerd voor een aantal problemen die voorkomen in geofysische stromingen. Om aan te tonen dat de ruimte-tijd DG methode in het bijzonder geschikt is voor problemen met dynamische grid bewegingen, hebben we niet-lineaire golven gesimuleerd die opgewekt worden door een golf maker. Dit hebben we geverifieerd voor lage amplitude golven waar lineaire theorie bij benadering geldig is.

De vrije oppervlakte gravity water wave vergelijkingen worden uitgebreid gebruikt in maritiem en off-shore onderzoek. Het wiskundig karakter van deze vergelijkingen is complex omdat deze bestaan uit een potentiaal vergelijking die elliptisch is en niet-lineaire vrije oppervlakte rand condities die hyperbolisch van aard zijn. Derhalve wordt een ruimte-tijd discontinue Galerkin eindige elementen methode gepresenteerd voor vereenvoudigde lineaire vrije oppervlak gravity water wave vergelijkingen. De vrije oppervlakte gravity water wave vergelijkingen kunnen ook afgeleid worden uit Luke's variationele formulatie welk geassocieerd wordt met het behoud van energie in de fase-ruimte, gegeven geschikte randcondities. Deze variationele formulatie vormt ook de basis voor een nieuw ruimte-tijd variationele (dis)continue Galerkin eindige elementen methode. Zowel de ruimte-tijd discontinue Galerkin en de ruimte-tijd variationele eindige elementen dis-

cretisaties resulteren in een algebraisch lineaire stelsel van vergelijkingen met een zeer compact stencil, d.w.z., de algebraische vergelijkingen van ieder element is gekoppeld alleen aan zijn directe buur elementen. Het lineaire stelsel van vergelijkingen wordt daarom gebouwd gebruik makend van efficiente block sparse matrix opslag routines en opgelost door gebruik te maken van iteratieve oplos methodes beschikbaar in het uitgebreid getestte PETSc pakket. De numerieke methode wordt geverifieerd voor harmonische golven in een periodiek domein en die door een golf maker gegenereerd worden.

Het uitbreiden van de ruimte-tijd discontinue Galerkin methode voor flooding en drying in de ondiep water vergelijkingen en voor de beweging van niet lineaire vrije oppervlaktes van diepe water golven wordt een toekomstig onderzoeks onderwerp.

Acknowledgements

The invaluable help, support and encouragement of my colleagues, friends and family has lead me to successfully finish this thesis. I would like to express my sincere gratitude to all of them in these most widely read pages of the thesis.

First and foremost, I am greatly indebted to my supervisor dr. ir. Onno Bokhove (Onno) for his constructive criticism, intuitive ideas and continuous encouragement towards my research work. Onno, you have been a great supervisor for me to excel as a researcher. I am also indebted to my promoter prof. J.J.W. van der Vegt (Jaap) for giving me an opportunity to work in the "Numerical Analysis and Computational Mechanics" (NACM) Group. Jaap, your timely involvement in my research project has helped me to focus more on my research goals. I am very thankful to both of you for the time and expertise that you have invested in reading the thesis.

For the past four and a half years, I had the pleasure to do scientific research in the NACM group. Credits to all my present and past colleagues at NACM and in particular to my office mates: Chris, Sena, Michael, Oleana, Domokos, Pablo, Davit, Sander, Bob and Lee for creating a friendly atmosphere in the office. I would like to also acknowledge the following people who contributed towards my research:

- It is a pleasure to thank Chris and Janavita for many useful discussions on space-time discontinuous Galerkin finite element method.
- My special thanks also go to Lars and Alex for sharing their knowledge on C++ programming, hpGEM project and PETSc package.

- I am also indebted to Domokos and Sander for carefully reading my thesis. Thanks to the later for translating the summary of this thesis in Dutch.

- It was a pleasure to closely work with Pablo and exchange ideas.

- I also thank Ferenc for making me acquainted with the underlying mathematical theory of finite elements.

In the initial days of my Ph.D. life, it was not easy to adapt to the living conditions and working environment in the Netherlands. Thanks to my Indian friends who made me accustom to the Dutch culture and weather. I would like to particularly thank Kiran, Tomar, Sashi bhabhi, Ravi, Madhavi, Pramod, Vishwas, Makarandh, Srinivas, Komal, Sheela and Vasughi for giving me a nice company during my stay in the university campus. Here, I must also thank Davit and Ferenc for inviting me to dinner parties and weekend outings which I enjoyed a lot and made me feel better.

After I got accustomed to Enschede, I have moved out of the university campus together with Ram (Ramakrishna Pasumarthy) to start the adventure of being an Enschede citizen. Ram, I have been really lucky to have you as my house mate. I can never forget all our dinner parties combined with either a movie show or playing cards, pool or bowling. We have not just partied but also collaborated in research which has resulted as a chapter in your Ph.D. thesis. Also, my special thanks for continuing your collaboration with me as a post doctoral student in Australia. I wish to see you in Australia soon. After Ram, I have been lucky to have another Ram (Ramakrishna Siddapa) as my next house mate. Ram, I have really enjoyed your company and specially spontaneous sense of humour. Also my special thanks to Ram's wife, Veda, who used to visit us in the weekends from Waganingen. Veda, thank you for always being a helping hand to me.

During my stay in Enschede, I have made some great friends: Visakha and Pramod, Srihari and Lakshmi, Meenakshi and Chandu, Kiran and Kavitha, Satya, Sandeep, Jeetu, Srivatsa, Srikanth, Ganesh, Anand, Raghav and many others. In particular, I am greatly indebted to Srihari and Lakshmi, Pramod and Visakha, and Meenakashi and Chandu for their help and support during the stressful days of my PhD. It is a pleasure to also thank Vibhor, the newly born child of Visakha and Pramod, for choosing me as his "official or legal" friend in Netherlands. My sweet kisses to the little

angel Pooji, daughter of Lakshmi and Srihari, who always likes to ride on my bike.

In Enschede, my favourite sport is to play badminton in DIOK ("Drank Is Onze Kracht"). I would like to thank all the members of DIOK club for conducting great tournaments, group events and cool parties. Also, many thanks to all the Diokkers who played badminton with me. It is my pleasure to also thank AADHAAR and ISA@UT for giving me an opportunity to participate in their activities.

Last but not least, I would like to thank my family and friends in India for their constant support and encouragement. I am greatly indebted to my parents, brother and sister for their love and support.

Vijaya Raghav Ambati

January 2008, Enschede.